

## **Copyright Warning & Restrictions**

The copyright law of the United States (Title 17, United States Code) governs the making of photocopies or other reproductions of copyrighted material.

Under certain conditions specified in the law, libraries and archives are authorized to furnish a photocopy or other reproduction. One of these specified conditions is that the photocopy or reproduction is not to be “used for any purpose other than private study, scholarship, or research.” If a user makes a request for, or later uses, a photocopy or reproduction for purposes in excess of “fair use” that user may be liable for copyright infringement,

This institution reserves the right to refuse to accept a copying order if, in its judgment, fulfillment of the order would involve violation of copyright law.

**Please Note: The author retains the copyright while the New Jersey Institute of Technology reserves the right to distribute this thesis or dissertation**

Printing note: If you do not wish to print this page, then select “Pages from: first page # to: last page #” on the print dialog screen

The Van Houten library has removed some of the personal information and all signatures from the approval page and biographical sketches of theses and dissertations in order to protect the identity of NJIT graduates and faculty.

## **ABSTRACT**

### **MULTI-WAVELENGTH PYROMETRIC SYSTEMS FOR EMISSIVITY- INDEPENDENT NON-CONTACT TEMPERATURE SENSING**

**by**

**Michael B. Kaplinsky**

A Multi-Wavelength Imaging Pyrometer (M-WIP) for real-time remote sensing of temperature profiles of targets with unknown emissivity was developed and demonstrated. To measure the spectral radiance of a target at several distinct wavelengths an M-WIP system was implemented based on an 320x122-element PtSi IR-CCD imager with an assembly of 7 narrow-band IR filters in the range from 1790nm to 4536nm. A real-time algorithm for simultaneous estimation of the temperature and model parameters of the target emissivity from the least-squares fit of the theoretical model of IR camera output signal to the experimental spectral measurements was developed and implemented. This real-time least-squares minimization was accomplished by combination of Levenberg-Marquardt and simulated annealing algorithms. The least-squares-based calibration algorithm was developed for evaluation of effective values of peak transmissions and center wavelengths of M-WIP channels based on the detection of radiation from pre-calibrated blackbody source. To achieve high radiometric accuracy, compensation for the dark current charge as function of the detected signal level was implemented. The effect of the response non-linearity of IR imager was minimized by developing an algorithm for imager operation at fixed pre-selected signal level for each M-WIP spectral channel based on adaptive control of the duration of the optical integration time of the imager. Initial testing demonstrated an accuracy of  $\pm 1.0^{\circ}\text{C}$  for real-time temperature measurements of the center of the blackbody aperture in the range from  $500^{\circ}\text{C}$  to  $1000^{\circ}\text{C}$ . Temperature resolution of  $\pm 3^{\circ}\text{C}$  was demonstrated for the blackbody source viewed through a double side polished silicon wafer with unknown spectral transmissivity in the temperature range from  $500^{\circ}\text{C}$  to  $900^{\circ}\text{C}$ .

**MULTI-WAVELENGTH PYROMETRIC SYSTEMS FOR EMISSIVITY-  
INDEPENDENT NON-CONTACT TEMPERATURE SENSING**

**by**

**Michael B. Kaplinsky**

**A Dissertation  
Submitted to the Faculty of  
New Jersey Institute of Technology  
in Partial Fulfillment of the Requirements for the Degree of  
Doctor of Philosophy**

**Department of Electrical and Computer Engineering**

**May 1997**

Copyright © 1997 by Michael B. Kaplinsky

ALL RIGHTS RESERVED

**APPROVAL PAGE**

**MULTI-WAVELENGTH PYROMETRIC SYSTEMS FOR EMISSIVITY-  
INDEPENDENT NON-CONTACT TEMPERATURE SENSING**

**by**

**Michael B. Kaplinsky**

**April 28, 1997**

---

Dr. Edwin Hou, Committee Chair

Associate Professor of Electrical and Computer Engineering, NJIT

---

Dr. Constantine N. Manikopoulos, Committee Member

Associate Professor of Electrical and Computer Engineering, NJIT

---

Dr. N. M. Ravindra, Committee Member

Associate Professor of Physics, NJIT

---

Dr. Yun-Qing Shi, Committee Member

Associate Professor of Electrical and Computer Engineering, NJIT

---

Dr. Vipul Patel, Committee Member

Member of Technical Staff, David Sarnoff Research Center

## BIOGRAPHICAL SKETCH

**Author:** Michael B. Kaplinsky

**Degree:** Doctor of Philosophy in Electrical Engineering

**Place of Birth:** Moscow, Union of Soviet Socialist Republics

### Graduate Education:

- Doctor of Philosophy in Electrical Engineering,  
New Jersey Institute of Technology, Newark, New Jersey, 1997
- Master of Science in Electrical Engineering,  
New Jersey Institute of Technology, Newark, New Jersey, 1993
- Master of Science in Mechanical Engineering,  
Moscow Institute of Steel and Alloys, Moscow, USSR, 1989

**Major:** Electrical Engineering

### Presentations and Publications:

- M. B. Kaplinsky, J. Li, N. J. McCaffrey, E. S. Hou, and W. F. Kosonocky, "Progress on the Development of Multi-Wavelength Imaging Pyrometer", *SPiE Proceedings*, Vol. 2746-18, Orlando, FL (1996).
- M. B. Kaplinsky, J. Li, N. J. McCaffrey, W. F. Kosonocky, E. S. H. Hou, and N. M. Ravindra, "Multi-Wavelength Imaging Pyrometer for Non-Contact Temperature Monitoring," *Proceedings of 1996 TMS Annual Meeting*, Anaheim, CA (1996).
- M. B. Kaplinsky, J. Li, N. J. McCaffrey, V. Patel, E. S. H. Hou, N. M. Ravindra, C. N. Manikopoulos, and W. F. Kosonocky, "Recent Advances in the Development of Multi-Wavelength Imaging Pyrometer," submitted for publication in *Optical Engineering* (1997).
- M. B. Kaplinsky, J. Li, N. M. Ravindra and W. F. Kosonocky, "Multi-Wavelength Imaging Pyrometer: Calibration and Experimental Results," accepted for presentation at *7th Infrared Radiometric Sensor Calibration Symposium*, Logan, Utah (May 1997).

- M. B. Kaplinsky, W. F. Kosonocky, N. J. McCaffrey, J. Li, E. S. Hou, C. N. Manikopoulos, and N. M. Ravindra, "Multi-Wavelength Imaging Pyrometer for Non-Contact Temperature Sensing," *Proceedings of IEEE International Symposium on Industrial Electronics*, Athens, Greece (July 1995).
- M. B. Kaplinsky, W. F. Kosonocky, and N. J. McCaffrey, "Calibration of Multi-Wavelength Imaging Pyrometer," *Proceedings of 5th Infrared Radiometric Sensor Calibration Symposium*, Logan, Utah (May 1995).
- J. Li, E. Hou, M. B. Kaplinsky, J. Li, N. J. McCaffrey, and W. F. Kosonocky, "M-WIP Workstation for RTP Monitoring and Control," *Proceedings of 1996 TMS Annual Meeting*, Anaheim, CA (February 1996).
- W. F. Kosonocky, M. B. Kaplinsky, N. J. McCaffrey, E. Hou, C. N. Manikopoulos, N. M. Ravindra, S. Belikov, J. Li, and V. Patel, "Multi-Wavelength Imaging Pyrometer", *SPIE Proceedings*, Vol. 2225-04, Orlando, FL (1994).
- N. J. McCaffrey, M. B. Kaplinsky, and W. F. Kosonocky, "Radiometric Performance of 640x480 and 320x122 PtSi IR Cameras", *SPIE Proceedings*, Vol. 2225-05, Orlando, FL (1994).
- S. Belikov, H. Martynov, M. B. Kaplinsky, and C. N. Manikopoulos, "Using Wavelength-Dependent Emissivity of Semiconductor Wafer to Model Heat Transfer in Rapid Thermal Processing Station," *IEEE Transactions on Semiconductor Manufacturing*, Vol. 8, No. 3 (1995).
- S. Belikov, M. B. Kaplinsky, and B. Friedland, "Parameter Estimation for Evaluating the Ability of a Rapid Thermal Processing System to Maintain Uniform Temperature," *Proceedings of 4th IEEE Conference on Control Applications*, Albany, NY (1995).
- S. Belikov, M. Kaplinsky, N. Ravindra, F. Tong, W. Kosonocky, J. Markham, and K. Kinsella, "Wafer Temperature Measurements Correction for Multi-Wavelength Imaging Pyrometer using Kalman Filtering," *Proceedings of The 3rd International Rapid Thermal Processing Conference*, Amsterdam, Netherlands (1995).
- S. Belikov, M. Kaplinsky, and B. Friedland, "Parameter Estimation in a Dynamic Model for Rapid Thermal Processing: Theory and Experimental Results," *Proceedings of 1995 American Control Conference*, Seattle, WA (1995).
- S. Belikov, H. Martynov, and M. Kaplinsky, "Design of Rapid Thermal Processing System Based on MSC/NASTRAN Thermal Analysis," *Proceedings of 1995 MSC World User's Conference*, Universal City, CA (1995).



- S. Belikov, H. Martynov, M. Kaplinsky, C. Manikopoulos, N. Ravindra, and W. Kosonocky, "A Design Methodology for Configuration of Lamps in an RTP System", *Proceedings of 2nd International Rapid Thermal Processing Conference RTP'94*, Monterey, CA (1994).
- V. Patel, M. B. Kaplinsky, W. F. Kosonocky, S. Ayyagari, and B. Singh, "Heat Transfer Analysis of Silicon Wafers During Reactive Ion Etching," *Proceedings of 39th National AVS Symposium*, SRC ID# N92039 (1992).
- P. Zotov, O. Blinov, V. Berdyshev, and M. Kaplinskii, "Research Into Heat Transfer in Furnaces with Screen Systems," *Steel in the USSR*, 16(9), London (1986).

This work is dedicated to the memory of my mentor  
Dr. Walter F. Kosonocky  
whose support, ideas and friendship made this work possible

## ACKNOWLEDGMENT

The author wishes to dedicate this work to the memory of his dissertation advisor and friend, Professor Walter F. Kosonocky. The author is infinitely grateful for his support and encouragement throughout the term of this work.

Very special thanks go to my wife and NJIT doctoral student, Helen Martynov, who provided constructive criticism throughout the term of this work, and who believes that her name should be placed next to my dissertation advisor due to significance of her contributions to this dissertation.

The author would like to acknowledge Dr. Edwin Hou, Dr. N. M. Ravindra, Dr. Constantine N. Manikopoulos and Dr. Vipul Patel for moral support during the trying times following the death of Dr. Kosonocky and for providing technical suggestions and moral support during the term of this work.

Special thanks are due to Professor Dr. Yun-Qing Shi for serving as member of the committee.

The author also wishes to express his appreciation to Jun Li and Nathaniel McCaffrey, NJIT doctoral students, for their friendship and help with experimental part of this work.

The author also would like to thank Guang Yang, Zeynep Pektas and Taras Golota for their friendship and help during my years at NJIT Electronic Imaging Center.

Finally, the author would like to acknowledge funding for this work provided by DARPA, NASA and NJIT Foundation Chair for Optoelectronics and Solid-State Circuits.

## TABLE OF CONTENTS

Chapter	Page
1 INTRODUCTION.....	1
2 BASIC CONCEPTS OF RADIATION THERMOMETRY .....	8
2.1 Spectral Radiance and Exitance .....	8
2.2 Black Body Radiators .....	9
2.3 Emissivity of Real Surfaces .....	12
2.4 Radiometric Model of the IR Sensor .....	14
2.5 Accuracy and Limitations of Conventional Radiometric Methods .....	16
2.5.1 Wide-Band Temperature Measurements. ....	17
2.5.2 Single Wavelength Radiometry .....	19
2.5.3 Two Wavelengths Ratio Radiometry .....	20
2.5.4 Multi-Wavelength Radiometry .....	25
3 MULTI-WAVELENGTH IMAGING PYROMETRY (M-WIP).....	27
3.1 Basic Concepts of Least-Squares-Based M-WIP.....	27
3.2 Real-Time M-WIP Algorithm .....	29
3.2.1 Levenberg-Marquardt Method.....	30
3.2.2 Method of Simulated Annealing.....	32
3.3 General Configuration of M-WIP Systems.....	33
3.4 M-WIP Filter Optics.....	34

## TABLE OF CONTENTS (Continued)

Chapter	Page
3.5 Radiometric Model of M-WIP Sensor.....	40
4 PERFORMANCE PREDICTION FOR MULTI-WAVELENGTH PYROMETERS....	48
4.1 General Methodology of M-WIP Performance Prediction.....	48
4.2 Performance of M-WIP Systems Based on PtSi Imagers with Schottky-Barrier IR Detectors (SBDs).....	55
4.2.1 320x244 IR CCD and 640x480 IR MOS Image Sensors.....	55
4.2.2 PtSi Schottky-Barrier Detector .....	57
4.2.3 Accuracy of M-WIP Temperature Measurements based on IR FPA with PtSi Schottky-Barrier Detectors .....	59
4.3 Performance of M-WIP Systems Based on InGaAs Photodetector Array .....	60
4.3.1 Experimental M-WIP System .....	61
4.3.2 Theoretical Performance Prediction.....	63
4.3.3 Experimental Evaluation of InGaAs M-WIP Performance.....	69
4.4 Performance of M-WIP System based on Uncooled Microbolometer Focal Plane Array .....	74
4.4.1 Design and Operational Principle of Microbolometer UFPA .....	74
4.4.2 Responsivity of Microbolometer Detectors .....	76
4.4.3 Noise Sources Affecting Bolometer Operation.....	78
4.4.4 Predicted Performance of Microbolometer-Based M-WIP.....	81

## TABLE OF CONTENTS (Continued)

Chapter	Page
5 EXPERIMENTAL 7-FILTER LINE-SENSING M-WIP SYSTEM.....	83
5.1 General Description of the System.....	83
5.2 M-WIP Filters and Optics.....	84
5.3 320x244 PtSi IR-CCD Camera and It's Operation .....	87
5.4 Signal Processing System .....	90
6 CALIBRATION OF M-WIP SYSTEM AND EXPERIMENTAL RESULTS.....	91
6.1 Compensation for Inherent System Non-Linearities.....	91
6.1.1 Dark Current Compensation.....	91
6.1.2 Correction for Saturation Non-Linearity of the Imager Response .....	97
6.2 Fixed Signal Level M-WIP Operation for Non-Linearity Independent Real-Time Temperature Sensing .....	100
6.3 Calibration of NJIT M-WIP System.....	105
6.3.1 Initial Calibration of M-WIP Spectral Characteristics .....	108
6.3.2 Compensation for Secondary Transmission Bands of M-WIP Filters .....	112
6.4 Demonstrated Temperature Resolution of M-WIP based on PtSi IR FPA.....	117
7 CONCLUSIONS.....	122
REFERENCES .....	125

## LIST OF FIGURES

Figure	Page
2.1 Spectral radiance of a blackbody radiator. ....	10
2.2 Comparison of blackbody and real body emission: (a) spectral distribution and (b) directional distribution of radiance.....	12
2.3 Imaging radiation thermometer with lens.....	14
2.4 Calculated NE $\Delta$ T of 640x480 IR MOS Sarnoff imager with f/1.4 optics.....	19
2.5 Calculated and measured signal of 320x122 Sarnoff IR-CCD imager operating with optical integration time of 33 ms, f/2 optics and 20-nm Gaussian filter with 60% peak of transmission. ....	21
2.6 Illustration of the basic principle of ratio radiometry: temperature is inferred from the ratio of signals measured at two wavelengths. ....	22
2.7 Calculated accuracy of ratio pyrometry for 320x244 IR CCD camera operating with optical integration time of 33 ms, f/2 optics, and 20 nm Gaussian filters.....	24
3.1 Illustration of the least-squares fit performed by M-WIP for simulated signal. ....	27
3.2 Schematic diagram of Multi-Wavelength Imaging Pyrometer with optical filters positioned in close proximity of the array of photodetectors. ....	34
3.3 Schematic diagram of Multi-Wavelength Imaging Pyrometer with relay optics used to refocus optical filters onto the array of photodetectors.....	34
3.4 Line-sensing M-WIP configuration with one cylindrical lens. ....	35
3.5 Line-sensing M-WIP configuration with two cylindrical lenses.....	35
3.6 Area-sensing M-WIP configuration utilizing rotating filter wheel.....	36
3.7 Area-sensing M-WIP configuration based on mosaic and striped filter assemblies. ....	37

Missing Page



## LIST OF FIGURES (Continued)

Figure	Page
4.8 Photograph of Sensors Unlimited SU256L-1.7RT-250A linear array. ....	62
4.9 Schematics of Sensors Unlimited SU256L-1.7RT-250A InGaAs array .....	62
4.10 InGaAs responsivity approximation. ....	63
4.11 Simulated detected signal for InGaAs line sensor viewing blackbody target. ....	64
4.12 M-WIP performance estimated for InGaAs sensor viewing blackbody target. ....	65
4.13 M-WIP performance estimated for InGaAs sensor viewing linear radiator. ....	66
4.14 Effect of detector response non-linearity on M-WIP performance. ....	67
4.15 InGaAs M-WIP performance vs. uncertainty in filter wavelengths. ....	69
4.16 Experimental measurements of blackbody radiance and dark current obtained with Sensors Unlimited InGaAs detector array. ....	70
4.17 Measured and estimated dark current for Sensors Unlimited InGaAs array. ....	71
4.18 Corrections for inherent non-linearity of InGaAs detector response. ....	72
4.19 Calibrated response of Sensors Unlimited InGaAs line sensor array. ....	73
4.20 Demonstrated accuracy of M-WIP temperature measurements with Sensors Unlimited InGaAs linear photodetector array. ....	74
4.21 Microscope photograph of Honeywell microbolometer array .....	75
4.22 Schematics and operational principle of microbolometer. ....	75
4.23 Absorptance of Honeywell microbolometer detector .....	76
4.24 Simulated UFPA signal for IR filters with 10% fractional bandwidth. ....	82

## LIST OF FIGURES (Continued)

Figure	Page
UFPA M-WIP performance for filters with 10% fractional bandwidth .....	82
Schematics of experimental NJIT Multi-Wavelength Imaging Pyrometer.....	83
Mosaic filter assembly initially utilized in experimental M-WIP system.....	85
Filter optics employed in experimental line-sensing NJIT M-WIP system.....	85
Video image of line-sensing filter assembly. ....	86
Schematics of the Sarnoff 320X244 IR-CCD FPA.....	88
Dark current signal for the 320x122 IR-CCD camera versus integration time.....	92
Dark current non-uniformity for the 320x122 PtSi IR-CCD camera.....	93
Measured and estimated dark current. ....	94
Signal corrections employed by initial M-WIP algorithm. ....	96
Initial measurements of blackbody temperature based on prerecorded data.....	97
Saturation non-linearity correction. ....	99
Optical integration times corresponding to fixed pre-selected signal level.....	101
Estimated effect of response nonuniformity on M-WIP temperature resolution: 1 - gray body & filter calibration, 2 - color body & filter calibration, 3 - gray body & pre-measured filters, 4 - color body & pre-measured filters. ....	108
Certificate of calibration of Mikrom M360 reference blackbody source.....	109
10 The background signal of the 320X122 IR-CCD camera vs. optical integration time. ....	111
11 Temperature-dependent calibration of M-WIP filters. ....	113

## LIST OF FIGURES (Continued)

Figure	Page
6.12 Temperature-dependent calibration of M-WIP filters vs. manufacturers data.....	114
6.13 Real-time M-WIP measurements of blackbody temperature after implementation of on-line correction for “saturation” nonlinearity. ....	116
6.14 Real-time M-WIP measurements of blackbody temperature after implementation of non-linearity independent M-WIP algorithm. ....	117
6.15 M-WIP measurements of target temperature with effective emissivity equal to the transmissivity of double-polished silicon wafer. ....	118
6.16 Real-time M-WIP temperature measurements of blackbody target viewed through double-polished silicon wafer. Based on non-linearity independent algorithm.....	119
6.17 Measured and M-WIP modeled signal levels for blackbody target in the temperature range from 450°C to 750°C.....	120
6.18 First two steps of $\chi^2$ - minimization by M-WIP algorithm for target at 973.3°C with effective emissivity equal to the transmissivity of the double side polished silicon wafer. ....	121
6.19 $\chi^2$ - minimization by M-WIP algorithm in the proximity of the solution for the same target as in Figure 6.18.....	121

## LIST OF TABLES

Table	Page
5.1 Spectral characteristics of M-WIP filters (Optical Filter Corporation).....	87
6.1 Fixed operating signal levels and corresponding optical integration times .....	105
6.2 Calibration of M-WIP filters.....	110

## CHAPTER 1

### INTRODUCTION

The research presented in this dissertation was performed at Electronic Imaging Center of New Jersey Institute of Technology under the general direction of the late Dr. Walter F. Kosonocky, Distinguished Professor of Electrical and Computer Engineering and NJIT Foundation Chair for Optoelectronics and Solid-State Circuits. Dr. Walter F. Kosonocky was my dissertation advisor from January 1994 until his sudden death on November 02, 1997. Subsequently, Dr. Edwin Hou of NJIT ECE Department assumed the responsibility of chairing my dissertation committee.

The author would like to acknowledge the support for this work provided by DARPA and NASA under the following contracts:

- DARPA Contract F33615-92-C-5817 *Multi-Wavelength Imaging Pyrometry for Semiconductor Process Monitoring and Control*;
- DARPA TRP Agreement MDA972-95-3-0022 *for Uncooled Low-cost Technology Reinvestment Alliance (ULTRA)*;
- DARPA Contract DAAH01-93-C-R272 *Compact NIR Spectral Radiometer for CVD Non-Contact Temperature Measurements*;
- NASA Contract NAS1-18226 *Radiometric Infrared Focal Plane Array Imaging System for Thermographic Applications*.

The major objective of this work was to study the advantages and limitation of multi-wavelength imaging pyrometry for non-contact temperature sensing and to develop the methodology for performance prediction of Multi-Wavelength Imaging Pyrometers (MWIPs) based on a variety of IR sensors. The second major objective of this work was to develop and demonstrate an experimental 7-filter line-sensing Multi-Wavelength Imaging

Pyrometer based on 320x244 Sarnoff IR-CCD imager with PtSi Schottky-barrier detectors.

The non-contact radiometric temperature measurements are based on the detection and analysis of thermal radiation emitted by an object. The underlying idea of all radiometric techniques is based on the concept of the blackbody radiator which is defined as an ideal surface that emits more thermal radiation than any other surface at the same temperature. The emission of real objects can be described by the surface emissivity,  $\epsilon$ , which is defined as the ratio of radiation emitted by the real surface to that emitted by the blackbody at the same temperature.

In general, to infer the temperature of the target from the measurement of emitted radiation, the value of the surface emissivity should be known. Therefore, in the situations where the emissivity of the target is changing rapidly, or the conditions of the process preclude the independent measurements of target emissivity, conventional radiometric methods will not yield the true temperature.

The extensive study of the radiometric literature and patents shows that there exists a wide variety of methods designed to circumvent the problem of unknown emissivity. Some of these methods (e.g. ratio radiometry) provide satisfactory results if certain, usually rather restrictive, assumptions about the spectral emissivity of the target are met. Other methods (referred to as multi-wavelength radiometry) require more extensive measurements but provide acceptable results without placing substantial restrictions on the shape of the spectral emissivity curve.

The well developed technique of two wavelength ratio radiometry yields accurate temperature measurements of surfaces with unknown emissivity, provided that the emissivity values within two spectral bands used in the measurements are equal. When this condition is satisfied, the ratio of spectral radiances measured at two distinct wavelengths depends only on target temperature and does not contain emissivity term.

A patent search revealed that there is a number of patents related to ratio pyrometers

for non-contact temperature sensing [1,2,3,4,5]. Some of the available ratio pyrometers employ individual photodetectors and provide for single point temperature measurements, others employ two-dimensional imaging arrays and provide for measurement of the temperature distribution on the target surface.

Among single point ratio pyrometers, an “Active Optical Pyrometer” described by Glenn may be mentioned [6]. This system represents a sophisticated ratio pyrometer employing two laser sources illuminating the target at two distinct wavelengths. The temperature and emissivity of the target are estimated based on the detection of the emitted and reflected radiation. This technique, though circumventing many shortcomings of the conventional ratio pyrometry, is invasive and is not capable of temperature measurements of distant targets.

Among imager-based ratio pyrometers, a system described by Tatsuwaki should be noted [7]. This system represents an imaging pyrometer capable of accurate sensing of temperature distribution on gray surfaces (constant emissivity). However, in the absence of the detailed knowledge of the spectral emissivity of the target, the system described by Tatsuwaki does not appear capable of accurate temperature measurements for targets with spectrally dependent surface emissivity.

As was already mentioned, ratio pyrometers rely on unrealistic assumptions about the spectral emissivity of the targets and, in general, do not yield accurate temperature measurements for non-gray (color) targets. In contrast, least-squares based multi-wavelength pyrometers determine target temperature and emissivity simultaneously from the multiple ( $> 3$ ) spectral measurements [8,9]. One of such systems, “Emissivity Independent Multiwavelength Pyrometer” described by Khan et al. provided the foundation for the research presented in this dissertation. The least-squares based multiwavelength pyrometer system presented by Khan provides for single-point temperature measurements on targets with unknown wavelength-dependent emissivity [8]. In his patent Khan

developed the basic theory behind the least-squares based multiwavelength pyrometry. However, the system described by Khan lacks the imaging capability needed to determine the spatial temperature distribution on the target surface. Furthermore, the above patent does not provide algorithms for calibration and non-linearity compensation required for accurate real-time temperature sensing. The research presented in this dissertation extends the theory presented by Khan by developing the experimental Multi-Wavelength Imaging Pyrometer (M-WIP) and associated algorithms for real-time M-WIP minimization, calibration and non-linearity independent operation.

This work presents the development of Multi-Wavelength Imaging Pyrometer (M-WIP) for remote sensing of temperature profiles of hot surfaces with unknown wavelength-dependent emissivity. In the case of remote temperature sensing by M-WIP, the spectral radiance of the target is measured at several distinct wavelengths by an IR camera (or several individual IR detectors) with an assembly of narrow-band filters positioned in front of its focal plane array (FPA). Based on these measurements the temperature and model parameters of the target emissivity are determined simultaneously from the least-squares fit of the theoretical model of IR camera output signal to the experimental data. This least-squares minimization is accomplished in real-time by combination of Levenberg-Marquardt and simulated annealing algorithms.

An experimental part of this work is based on a 7-filter line-sensing M-WIP using a 320x122-element non-interlaced PtSi IR-CCD radiometric camera capable of operation with optical integration times ranging from 0.12ms to 12 s, thus providing wide dynamic range.

The experimental M-WIP system also includes a least-squares-based calibration algorithm for evaluation of effective values of peak filter transmissions and center wavelengths based on the detection of radiation emitted by the pre-calibrated blackbody source over a wide range of temperatures. In the case of the PtSi IR-CCD imager, both the dark current and the spectral responsivity of the Schottky-barrier detectors (SBDs) depend



on the SBD bias voltage and decrease with increasing level of integrated charge signal. To achieve high radiometric accuracy, we have found it necessary to operate the IR-CCD camera with black level and background subtraction, and compensation for dark current charge as function of the detected signal level.

Our initial approach to compensation for saturation non-linearity of the imager response was relying on its off-line characterization. However, the saturation non-linearity compensation based on the pre-stored correction coefficients did not completely linearize the signal due to on-line gain and offset fluctuations. To minimize the effect of the response non-linearity on the accuracy of real-time M-WIP temperature estimation, we have developed new M-WIP algorithm which provides for imager operation at fixed pre-selected signal level for each spectral channel. This algorithm exploits the ability of the imager to change on-line the duration of the optical integration time. Using this capability, we are able to find the values of the integration time yielding the same pre-selected signal level for all target temperatures. The resulting values of integration time, rather than detected signals, are then used for M-WIP temperature estimation, providing for virtually non-linearity independent operation.

After implementing the above non-linearity independent M-WIP algorithm and signal corrections, we have demonstrated an accuracy of  $\pm 1.0^{\circ}\text{C}$  for real-time temperature measurements of the center zone of the blackbody aperture in the range from  $650^{\circ}\text{C}$  to  $900^{\circ}\text{C}$ .

The study of the accuracy of M-WIP temperature measurements for targets with spectrally varying emissivity was conducted using a double side polished silicon wafer placed in the optical path of the M-WIP system. Temperature resolution of  $\pm 3^{\circ}\text{C}$  was demonstrated with the experimental M-WIP system for blackbody source viewed through the double polished silicon wafer with unknown spectral transmissivity in the temperature range from  $500^{\circ}\text{C}$  to  $950^{\circ}\text{C}$ .

Chapter 2 of this work provides brief overview of the basic concepts of the radiation thermometry. Black body radiation, surface emissivity and principles of the detection of thermal radiation are introduced. The chapter concludes with the analysis of conventional thermometric techniques and their limitations.

Chapter 3 explains the principle of the least-squares-based multi-wavelength pyrometry. The alternative designs of the filter optics for M-WIPs are then considered, including filter optics for area-sensing, line-sensing and point-sensing systems. The radiometric model of M-WIP based on Reference Wavelength Method is also presented in this chapter.

Chapter 4 develops the theoretical approach to performance prediction of multi-wavelength pyrometers. Using this method the performance of a number of M-WIPs was investigated, including M-WIP systems based on IR FPAs with PtSi Schottky-barrier detectors (SBDs), InGaAs line sensor arrays, and microbolometer Uncooled Focal Plane Arrays (UFPAs).

Chapter 5 presents an experimental 7-filter line-sensing M-WIP based on a 320x122-element non-interlaced PtSi IR-CCD radiometric camera capable of operation with optical integration times ranging from 0.12ms to 12 s. Following general overview, the description of the individual system components is given. The description of M-WIP optics and the line-sensing filter assembly consisting of 7 narrow-band striped interference filters in the range from 1790nm to 4536nm is followed by the discussion of the IR-CCD imager and the signal processing system.

Chapter 6 presents the procedure developed for the calibration of the experimental NJIT M-WIP system. This chapter starts from the discussion of the algorithms developed for compensation for the inherent non-linearities of the response of the IR-CCD imager with PtSi SBDs. The dark current compensation presented in Section 6.1 is followed by the description of the linearization of the imager response at high signal levels. The novel

approach for non-linearity independent M-WIP temperature sensing based on the operation of the imager at fixed pre-selected signal levels is presented in Section 6.3. Section 6.4 presents M-WIP calibration procedure including the algorithm for compensation for the secondary transmission bands (leakages) of M-WIP filters. The chapter concludes with the presentation and discussion of experimental results.

Finally, the conclusions outlining the main technical achievements of this work are presented in Chapter 7.

## CHAPTER 2

### BASIC CONCEPTS OF RADIATION THERMOMETRY

#### 2.1 Spectral Radiance and Exitance

All matter emits radiant energy as a consequence of its temperature. To obtain a quantitative description of the emitted radiation the concept of spectral radiance has been introduced. The spectral radiance,  $L_{\lambda,em}$ , is defined as the radiant flux,  $\Phi_{em}$ , emitted at the wavelength  $\lambda$  in a given direction, per unit of the emitting surface normal to this direction, per unit solid angle about this direction, and per unit wavelength interval  $d\lambda$  about  $\lambda$ . The spectral radiance, which has the units of  $[W/(m^2 \text{ sr } \mu m)]$ , may then be expressed as [10]

$$L_{\lambda,em}(\lambda, \theta) = \frac{d^3 \Phi_{em}}{dA_n d\omega d\lambda} \quad (2.1)$$

If the spectral and directional distributions of the spectral radiance are known, the radiant power per unit area of the emitting surface may be determined by integration of Equation (2.1) over finite solid angle and wavelength interval. In particular, the radiant power per unit area, emitted into the hemispheric space above the surface is defined as the total self-exitance,  $M_{em} [W/m^2]$ .

It is important to note that, in general, the directional distribution of surface emission varies according to the conditions of the surface. However, many real surfaces can be reasonably approximated by so-called lambertian surface. For a lambertian surface (also known as isotropically diffuse emitter) the radiance of the emitted radiation is independent of the direction. In this case the following relationship between radiance and exitance holds

$$M_{em} = \pi L_{em} \quad (2.2)$$

where  $L_{em}$  - is the total radiance of the emitted radiation  $[W/m^2 \cdot \text{sr}^{-1}]$ .

It should be noted that in this work all considerations will be restricted to emitters which can be closely approximated by lambertian surfaces within reasonably small solid angles.

## 2.2 Black Body Radiators

The noncontact radiometric temperature measurements are based on the detection and analysis of thermal radiation emitted by an object. The underlying idea of all radiometric techniques is based on the notion of the blackbody radiator. The blackbody is defined as an ideal surface that (1) absorbs all incident radiation, (2) emits more thermal radiation than any other surface at the same temperature, and (3) emits radiation in isotropically diffuse manner, i.e. independent of direction. The spectral distribution of the radiation emitted by the blackbody is given by Planck's distribution law

$$L_{\lambda,b}(\lambda, T) = \frac{C_1}{\lambda^5 \left( \exp\left(\frac{C_2}{\lambda T}\right) - 1 \right)} \quad (2.3)$$

where  $L_{\lambda,b}(\lambda, T)$  is the blackbody spectral radiance [ $\text{W}/\text{m}^2 \cdot \mu\text{m}$ ],  $T$  is the temperature of the blackbody radiator [K],  $\lambda$  is the wavelength [ $\mu\text{m}$ ],  $C_1 = 1.1911 \times 10^8$  is the first radiation constant [ $\text{W}\mu\text{m}^4/\text{m} \cdot \text{sr}$ ],  $C_2 = 1.4388 \times 10^4$  is the second radiation constant [ $\mu\text{m} \cdot \text{K}$ ].

The spectral radiance of a blackbody is shown in Figure 2.1 for selected temperatures. The following important characteristics of this distribution can be noted:

- (1) The emitted radiation varies continuously with wavelength.
- (2) At any wavelength the magnitude of the emitted radiation increases with increasing temperature.
- (3) The spectral region in which the radiation is concentrated depends on temperature, with comparatively more radiation appearing at shorter wavelengths as the temperature increases.

Since the form of Equation (2.3) is inconvenient for analytical manipulations a number of approximations to Planck's law have been developed. One of the most useful approximations to Equation (2.3) is known as Wien's approximation and has the form

$$L_{\lambda,b}(\lambda, T) = \frac{C_1}{\lambda^5 \exp\left(\frac{C_2}{\lambda T}\right)} \quad (2.4)$$

For  $\lambda T < 2900 \mu\text{m} \cdot \text{K}$  Planck's law and Wien's approximation produce almost indistinguishable results.

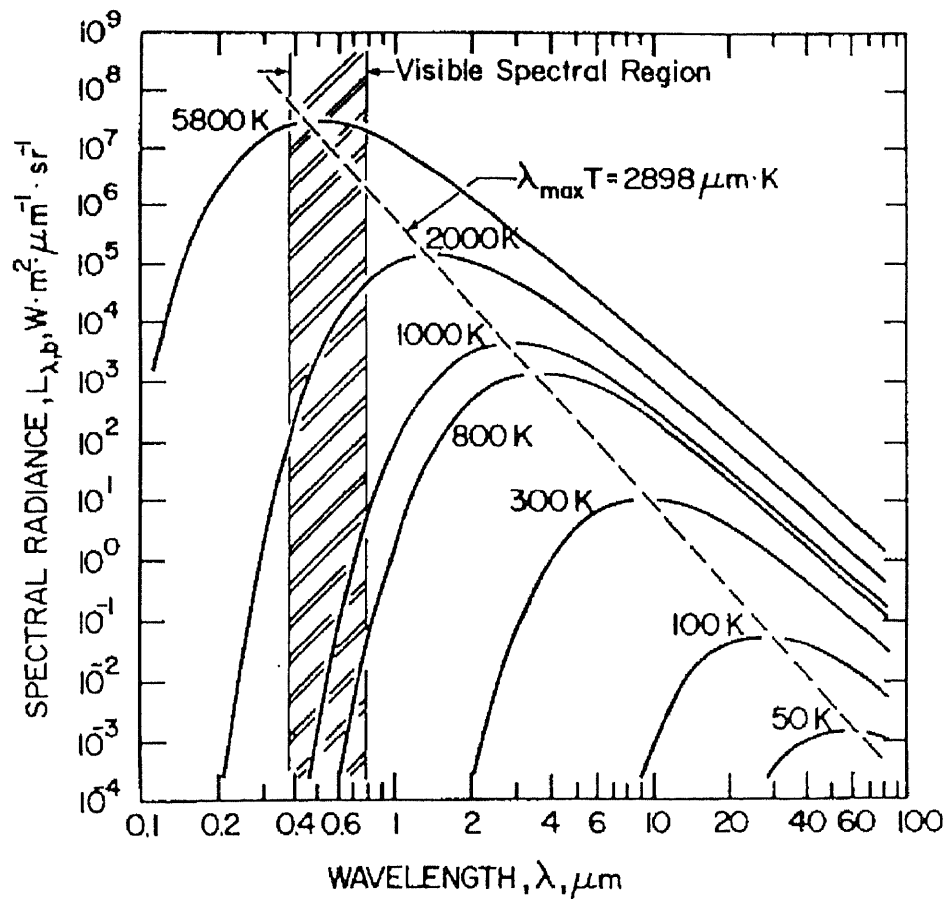


**Figure 2.1** Spectral radiance of a blackbody radiator [10]

It can be seen from Figure 2.1 that the blackbody spectral radiance is characterized by a maximum and that the wavelength associated with this maximum,  $\lambda_{\max}$ , depends on blackbody temperature. Differentiating the Planck distribution given by Equation (2.3) with respect to wavelength and setting the result equal to zero, we obtain:

$$\lambda_{\max} \cdot T = 2897.7 \text{ } [\mu\text{m} \cdot \text{K}] \quad (2.5)$$

Equation (2.5) is known as Wien's displacement law. According to this law, the maximum of spectral radiance is displaced to shorter wavelengths with increasing temperature of the radiant surface. Thus, for a blackbody at 1000 K peak emission occurs at 2.9  $\mu\text{m}$ , and for 300 K peak corresponds to 9.7  $\mu\text{m}$ .

It can be shown that the value of the blackbody spectral radiance at its maximum is proportional to the fifth power of the blackbody temperature. Performing the substitution of Equation (2.5) into Equation (2.3) and multiplying the constants we obtain

$$L_{\lambda,b}(\lambda_{\max}, T) = 1.288 \times 10^{-11} \cdot T^5 \left[ \frac{\text{W}}{\text{m}^2 \cdot \mu\text{m}} \right] \quad (2.6)$$

It might also be noted that the value of the total radiant power emitted from the unit surface area of a blackbody over the wavelength range from zero to infinity can be obtained by integration of Equation (2.7) for any given temperature  $T$ . The result of this integration can be expressed as

$$L_{0 \rightarrow \infty, b} = \sigma \cdot T^4 \left[ \frac{\text{W}}{\text{m}^2} \right] \quad (2.7)$$

where  $\sigma = 1.8049 \times 10^{-8} \text{ } [\text{W} / \text{m}^2 \cdot \text{K}^4]$  is the Boltzmann constant.

Equation (2.7), known as the Stefan-Boltzmann law, shows that the total radiant power emitted by a blackbody is proportional to the fourth power of temperature.

### 2.3 Emissivity of Real Surfaces

Using Equations (2.3) and (2.4), one can infer the blackbody temperature either from single wavelength (narrow band) or wideband measurements of the emitted thermal radiation. The major obstacle in utilizing single wavelength or broadband radiation detection for remote temperature measurement of real surfaces is the fact that emission of real objects is always less than that of a blackbody radiator and is characterized, in general, by wavelength-dependent spectral emissivity as:

$$L_{\lambda, \text{real}}(\lambda, T) = \epsilon(\lambda, T) \cdot L_{\lambda, b}(\lambda, T) \quad (2.8)$$

It should be noted that emissivity may assume different values according to whether one is interested in emission at a given wavelength, in a given direction or in weighted averages over all possible wavelengths and directions as shown in Figure 2.2.

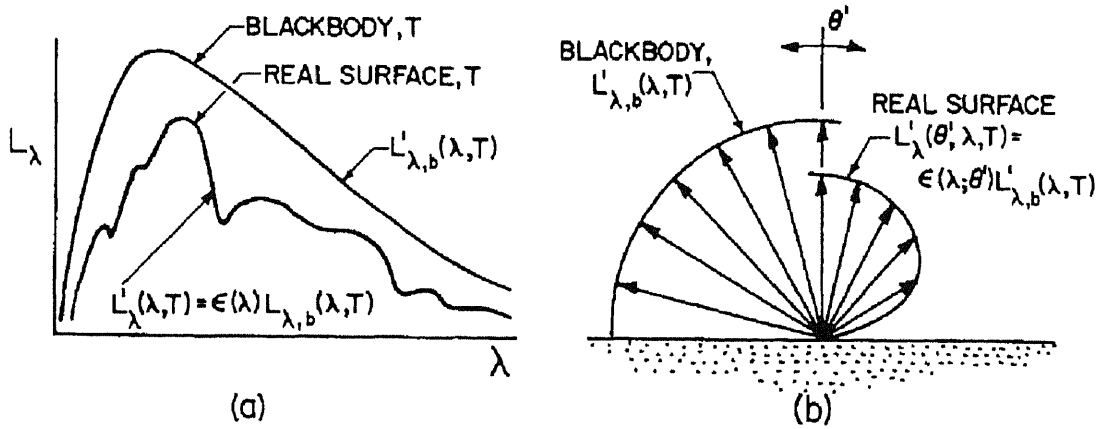


**Figure 2.2** Comparison of blackbody and real body emission: (a) spectral distribution and (b) directional distribution of radiance [10]

The spectral-directional emissivity  $\epsilon(\lambda, \theta, T)$  of a surface at temperature  $T$  is defined (assuming azimuthal isotropy for clarity) as the ratio of radiance of the radiation emitted at wavelength  $\lambda$  and in the direction  $\theta$  to the radiance of the radiation emitted by a blackbody



at the same temperature and wavelength

$$\varepsilon(\lambda, \theta, T) = \frac{L_{\lambda, \text{em}}(\lambda, \theta, T)}{L_{\lambda, \text{b}}(\lambda, T)} \quad (2.9)$$

It should be recognized that the spectral-directional emissivity is the most basic of the radiative properties from which other expressions for surface emissivity can be derived. The spectral-hemispherical emissivity (later referred to as spectral emissivity) represents a weighted average over all directions within the hemispherical space above a surface and is defined as:

$$\begin{aligned} \varepsilon(\lambda, T) &= \frac{\int_0^{\pi/2} L_{\lambda, \text{em}}(\lambda, \theta, T) \cos \theta \sin \theta \, d\theta}{\int_0^{\pi/2} L_{\lambda, \text{b}}(\lambda, T) \cos \theta \sin \theta \, d\theta} = \\ &= \frac{\int_0^{\pi/2} L_{\lambda, \text{em}}(\lambda, \theta, T) \cos \theta \sin \theta \, d\theta}{\pi \cdot L_{\lambda, \text{b}}(\lambda, T)} \end{aligned} \quad (2.10)$$

From Equation (2.10) it follows that for lambertian surfaces the spectral-directional emissivity is equal to the spectral-hemispherical emissivity

$$\varepsilon(\lambda, \theta) = \varepsilon(\lambda, 2\pi) \quad (2.11)$$

Finally, the total-hemispherical emissivity represents an average over the entire spectral range and for all possible directions and is defined as:

$$\varepsilon(t, 2\pi) = \frac{M_{\text{em}}(T)}{M_{\text{b}}(T)} \quad (2.12)$$

where  $M_{\text{b}}(T)$  is the total exitance of the blackbody radiator  $[\text{W}/\text{m}^2]$  and  $M_{\text{em}}(T)$  is the total self-exitance of the radiant surface given by Equation (2.2).

## 2.4 Radiometric Model of the IR Sensor

The actual radiometric temperature measurements require the availability of an adequate radiometric model of the IR sensor. For the purpose of the development of radiometric models of the IR sensors utilized in this work, the radiant flux originating from the remote radiant surface and entering the IR detectors can be approximated by integrating Equation (2.1) over the area of the emitting surface within the field of view of the detector, solid angle subtended by the detector aperture, and the total bandwidth of the radiometer, as:

$$\Phi(T) = \int_{\omega_t} \int_{A_{t,n}} \int_0^{\infty} L_{\lambda}(\lambda, T) dA_{t,n} d\omega_t d\lambda \quad (2.13)$$

where

$A_{t,n}$  - is the area of the projection of the emitting surface in the field of view to the plane perpendicular to the optical axes;

$\omega_t$  - is the solid angle subtended by the radiation beam leaving the surface of the radiant target and reaching the radiation detector;

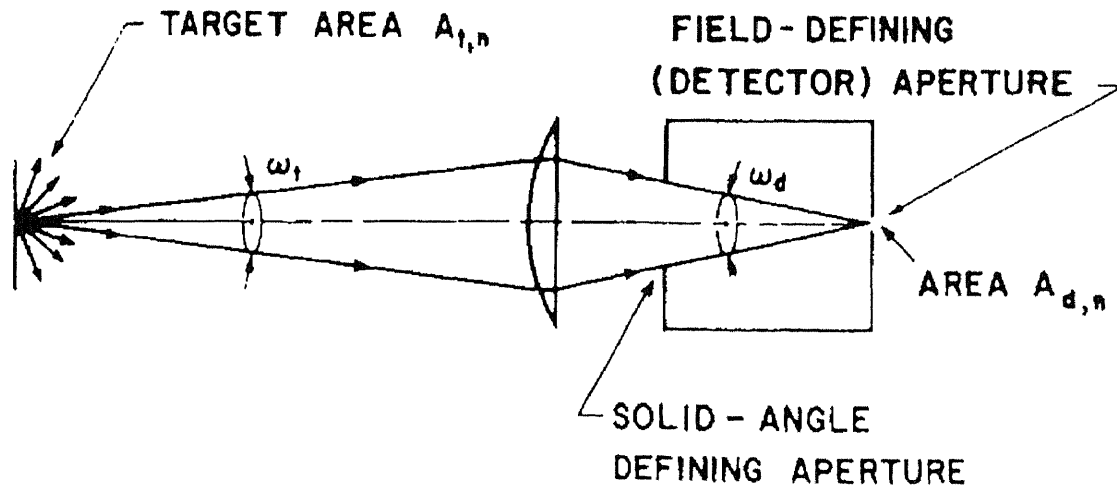


Figure 2.3 Imaging radiation thermometer with lens

For a lambertian emitting surface, radiance is essentially constant over the  $A_{t,n}$  and, for sufficiently remote target,  $d\omega_t$  has nearly the same value from all points on  $A_{t,n}$ . In addition to the above assumptions we use the concept of optical invariant [11] in the following form

$$A_{d,n} \omega_d = A_{t,n} \omega_t \quad (2.14)$$

where:

$A_{d,n}$  - is the area of projection of the detector aperture onto a plane perpendicular to the optical axes;

$\omega_d$  - is the solid angular field of view determined by the aperture.

Therefore, Equation (2.13) can be re-written as:

$$\Phi(T) = A_{d,n} \cdot \omega_d \cdot \int_0^{\infty} L_{\lambda}(\lambda, T) d\lambda \quad (2.15)$$

In order to obtain the output signal of the radiometer, we must also know its spectral responsivity function which is defined as:

$$R(\lambda) = \frac{dS}{d\Phi(\lambda)} \quad (2.16)$$

Substituting Equation (2.16) into Equation (2.15) and taking into consideration the transmission curve  $\tau(\lambda)$  of the filter positioned between the radiant target and detector (if applicable), we obtain the following expression for the signal detected by the imager viewing the radiant target

$$S(T) = A_{d,n} \cdot \omega_d \cdot \int_0^{\infty} \tau(\lambda) \cdot R(\lambda) \cdot L_{\lambda}(\lambda, T) d\lambda \quad (2.17)$$

The signal given by Equation (2.17) represents the output current of the radiation detector. For the purpose of this work, however, it is more convenient to represent the detected signal in terms of the electrical charge accumulated in the detector (pixel) during the optical integration time. The representation of the output signal of an imager in terms of electrons per pixel makes it easier to define radiation (shot) noise and to compare the signal under consideration with the maximum charge handling capacity of the detector. Therefore, in this work we will use the following expression for the signal detected by the imager:

$$S(T) = A_{d,n} \cdot \omega_d \cdot \frac{t_i}{Q_{el}} \cdot \int_0^{\infty} \tau(\lambda) \cdot R(\lambda) \cdot L_{\lambda}(\lambda, T) d\lambda \quad (2.18)$$

where  $t_i$  is the optical integration time [s],  $Q_{el} = 1.6 \times 10^{-19}$  is the charge of the electron [q].

Finally, we note that the spectral radiance  $L_{\lambda}$  of the radiation incident on the detector can be expressed by the product of the spectral emissivity of the emitting surface times the spectral radiance of the blackbody, in accordance with the Equation (2.8). Substitution of Equation (2.8) into Equation (2.18) leads us to the most general expression for the output signal of the radiation detector viewing the radiant target [12,13]:

$$S(T) = A_{d,n} \cdot \omega_d \cdot \frac{t_i}{Q_{el}} \cdot \int_0^{\infty} \varepsilon(\lambda, T) \cdot \tau(\lambda) \cdot R(\lambda) \cdot L_{\lambda,b}(\lambda, T) d\lambda \quad (2.19)$$

## 2.5 Accuracy and Limitations of Conventional Radiometric Methods

The radiometric model of IR sensor given by Equation (2.19) allows, in principle, to determine the temperature of radiative target based on the detection of its thermal radiation. However, in order to infer the temperature of the target from the wide band measurement of emitted radiation, the value of the total emissivity  $\varepsilon(T)$  should be known. Similarly, the

technique based on the measurement of the radiation through a narrow filter (single wavelength radiometry) requires the knowledge of target spectral emissivity,  $\epsilon(\lambda, T)$ , within the passband of the filter. Therefore, in the situations where the emissivity of the target is changing rapidly, or the conditions of the process preclude the independent measurements of target emissivity, the above radiometric methods will not yield the true temperature of the radiant target.

### 2.5.1 Wide-Band Temperature Measurements

It can be shown from statistical considerations [14,15] that the process of photon emission from a radiant surface, i.e. the number of photons emitted per unit time per unit area of emitter surface, can be described by the Poisson distribution. The same is equally true for the process of photon detection by a photodetector.

One of the fundamental properties of Poisson distribution is the fact that its standard deviation is equal to the square root of its mean. Applying this property to the process of photon detection by the radiation detector we conclude that rms radiation (shot) noise in the detected signal is equal to the square root of the signal itself.

Another source of noise in the output signal of the imager is the rms readout noise,  $N_{\text{readout}}$ , related to the mechanism of sensing the accumulated charge in the detector by the capacitor. Since the readout noise is independent of the radiation shot noise, the total noise in the imager output can be expressed as

$$\Delta S_{\text{noise}} = \sqrt{N_{\text{readout}}^2 + S(\lambda, T)} \quad (2.20)$$

If the emissivity of the target is known, Equation (2.19) can be solved numerically for target temperature,  $T$ , as a function of measured imager output signal  $S(T)$ . The accuracy of the temperature measurement in this case will be limited by the noise in the

output signal,  $\Delta S_{\text{noise}}$ , and is referred to as noise equivalent temperature difference, NE $\Delta$ T.

Using Equation (2.20) we can express NE $\Delta$ T as

$$S(T + \text{NE}\Delta T) - S(T) = \sqrt{N_{\text{readout}}^2 + S(\lambda, T)} \quad (2.21)$$

Considering the first order terms in a Taylor's series expansion of  $S(T)$  and using Equation (2.21) we can express NE $\Delta$ T as

$$\text{NE}\Delta T(T) = \frac{\sqrt{N_{\text{readout}}^2 + S(\lambda, T)}}{\frac{dS(\lambda, T)}{dT}} \quad (2.22)$$

In order to obtain the partial derivative of the signal with respect to temperature, we note that the only temperature dependent term in Equation (2.19) is the blackbody spectral radiance,  $L_{\lambda, b}$ , therefore

$$\frac{dS(T)}{dT} = A_{d,n} \cdot \frac{\pi}{4 \cdot (f/\#)^2} \cdot \frac{t_i}{Q_{el}} \cdot \int_0^\infty R(\lambda) \cdot \left( \frac{dL_{\lambda, b}(\lambda, T)}{dT} \right) d\lambda \quad (2.23)$$

where  $f/\#$  is the f-number of the optics.

The derivative of Planck's equation with respect to temperature is

$$\frac{dL_{\lambda, b}(\lambda, T)}{dT} = \frac{C_1 \cdot C_2 \cdot e^{\left(\frac{C_2}{\lambda T}\right)}}{\lambda^6 \cdot T^2 \cdot \left( e^{\left(\frac{C_2}{\lambda T}\right)} - 1 \right)^2} \quad (2.24)$$

From Equations (2.22)-(2.24) the NE $\Delta$ T can be numerically evaluated for any given value of the optical integration time  $t_i$ , and radiant target temperature  $T$ .

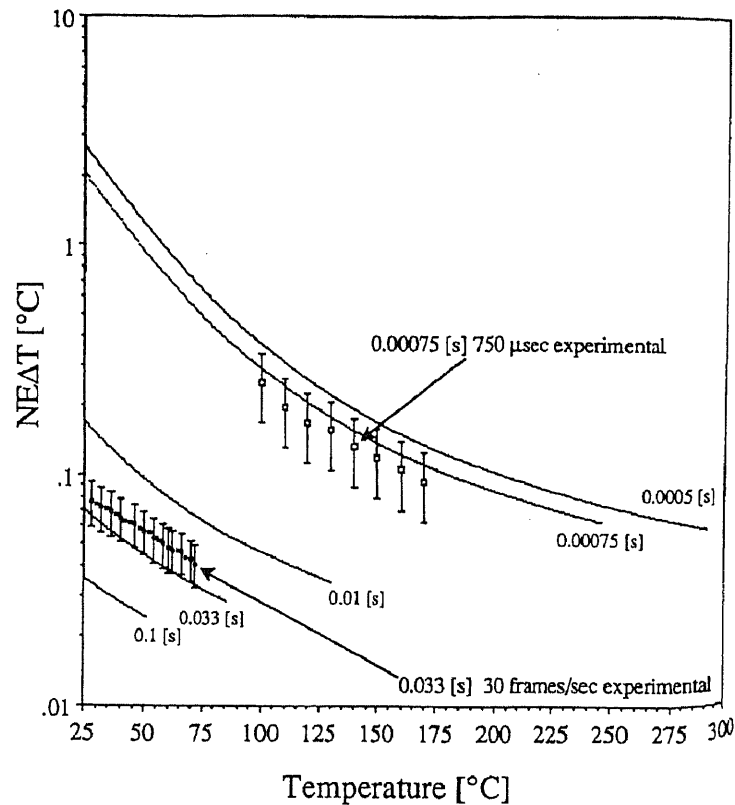


**Figure 2.4** Calculated NEAT of 640x480 IR MOS Sarnoff imager with  $f/1.4$  optics

The values computed from Equation (2.22) along with the experimentally obtained measurements of NEAT for 640x480 IR MOS imager manufactured at David Sarnoff Research Center [16] for different optical integration times and target temperatures are shown in Figure 2.4. Each curve in this figure is shown only up to the point where the signal level reaches the maximum charge handling capacity of the imager ( $Q_{\max} = 1.5 \times 10^6$  electrons per pixel).

### 2.5.2 Single Wavelength Radiometry

The wideband radiometric temperature measurements described in the previous section have the advantage of achieving high signal-to-noise ratio even for relatively low

temperatures of radiant target. However, at the elevated target temperatures the signal level has to be limited by decreasing the optical integration time in order to keep the signal below the maximum charge handling capacity of the detector. Inspection of Figure 2.4 shows that even for the moderate target temperature of 300 °C the integration time of the IR imager should be less than 0.5 ms.

In addition to the control of the optical integration time, the signal level can also be limited by the use of the narrow passband filter positioned between the target and the detector. This approach (referred to as monochromatic or single wavelength radiometry) is especially attractive because it does not require the knowledge of total emissivity. Instead, the spectral emissivity within the passband of the filter or even just at its center wavelength is being used.

The values of NE $\Delta$ T for 320x122 Sarnoff IR CCD camera, described in Chapter 4, operating with optical integration time of 33 ms, f/2 optics, and 20-nm-wide Gaussian filter having 60% peak transmission are shown in Figure 2.5 [12]. It should be noted, however, that these calculations were performed with the assumption of unlimited charge handling capacity. Therefore, the values of NE $\Delta$ T shown in Figure 2.5 are not realizable in practice for elevated temperatures of the radiant target.

### **2.5.3 Two Wavelengths Ratio Radiometry**

The analysis given in the preceding Section shows that some knowledge about the emissivity of the radiant target is essential to the temperature measurement techniques based on either wide band or single wavelength radiometry. Nevertheless, there exist a number of techniques designed to circumvent the problem of unknown emissivity of the radiant target. We will now briefly consider one of such methods, known as the method of ratio radiometry.



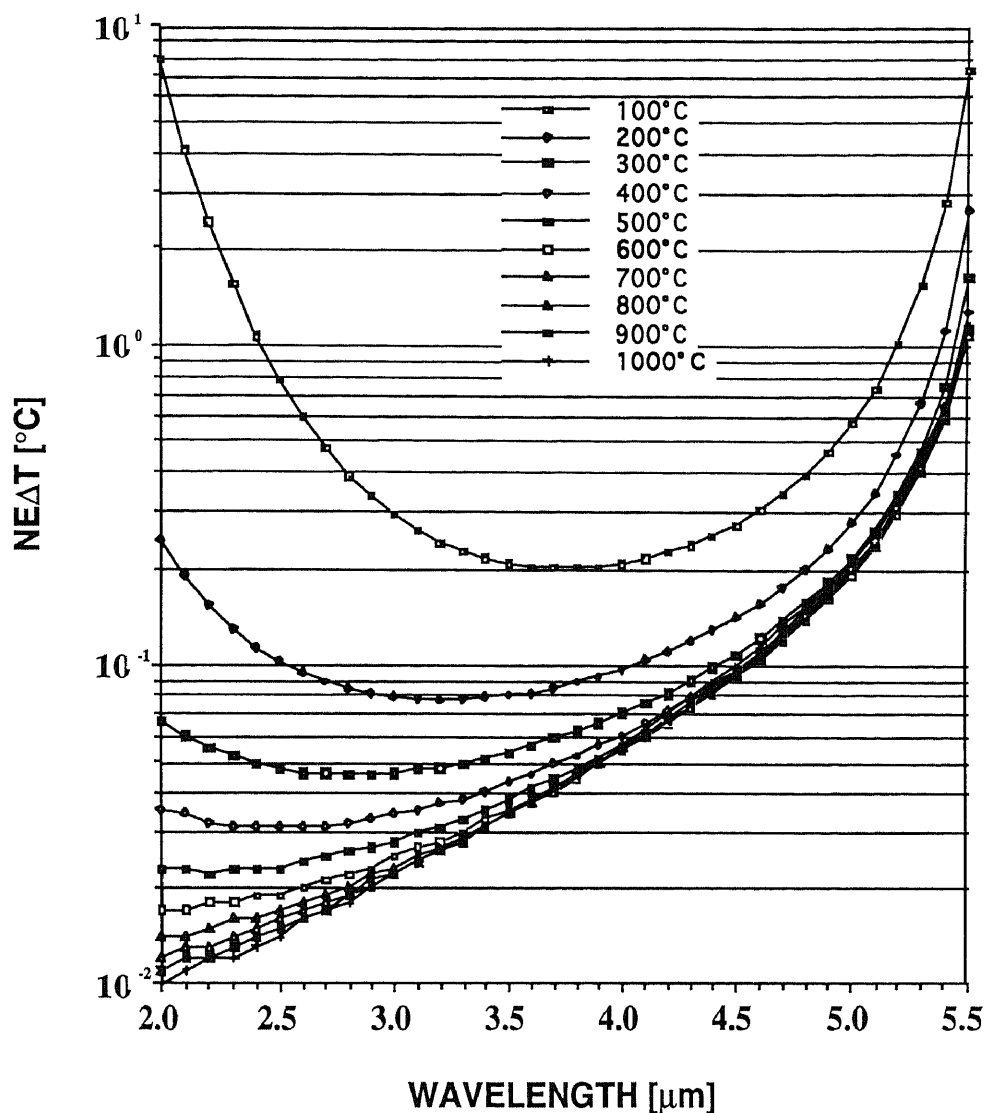


**Figure 2.5** Calculated and measured signal of 320x122 Sarnoff IR-CCD imager operating with optical integration time of 33 ms,  $f/2$  optics and 20-nm Gaussian filter with 60% peak of transmission

The two wavelength ratio radiometry (later referred to as ratio radiometry) involves measuring the spectral radiance of the target at two different wavelengths (see Figure 2.6) and inferring the temperature from the ratio of these two measurements. Although measuring two signals, rather than one, introduces the additional uncertainty due to the noise present in both measurements, the method of ratio radiometry can successfully

circumvent the problem of unknown emissivity for radiators with constant spectral emissivity (graybodies).

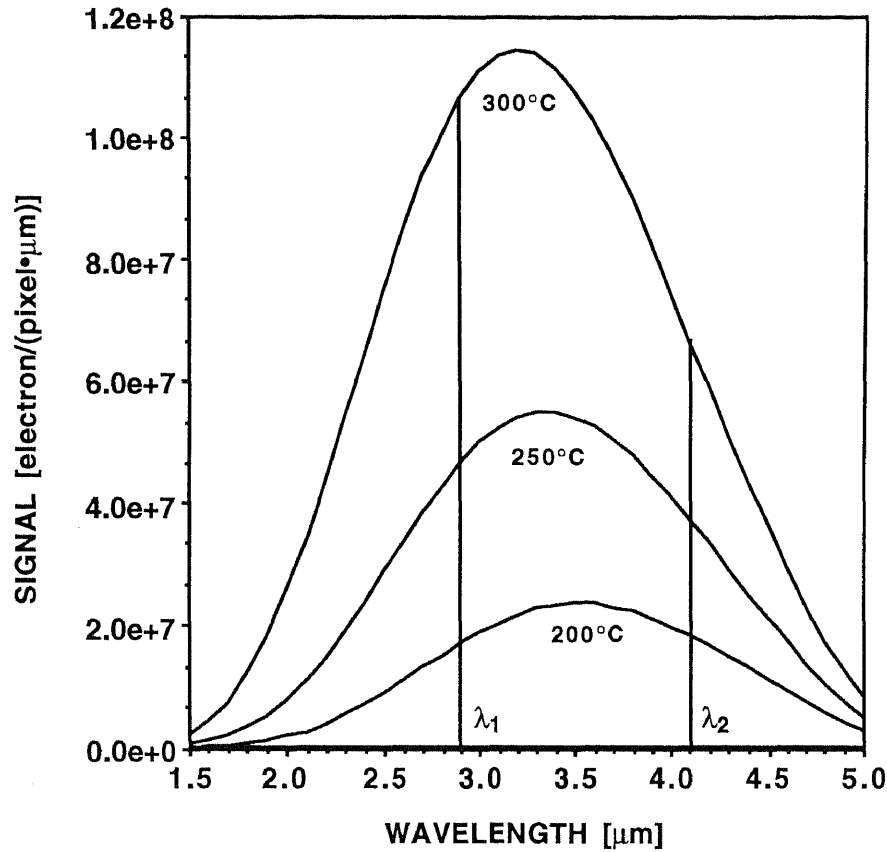


**Figure 2.6** Illustration of the basic principle of ratio radiometry: temperature is inferred from the ratio of signals measured at two wavelengths

Using Planck's law we can express the ratio of the signals detected at two distinct wavelengths  $\lambda_1$  and  $\lambda_2$  as

$$\frac{S_1(T)}{S_2(T)} = \frac{\varepsilon(\lambda_1) \cdot K(\lambda_1, T) \cdot R(\lambda_1) \cdot \lambda_1^{-5} \cdot e^{(-C_2/\lambda_1 T)}}{\varepsilon(\lambda_2) \cdot K(\lambda_2, T) \cdot R(\lambda_2) \cdot \lambda_2^{-5} \cdot e^{(-C_2/\lambda_2 T)}} \quad (2.25)$$

where  $S_1(T)$  and  $S_2(T)$  are the signals measured at  $\lambda_1$  and  $\lambda_2$ , respectively, and  $K(\lambda_1, T)$  and  $K(\lambda_2, T)$  are the correction coefficients depending primarily on the shape of the utilized narrow-band filters as explained in Chapter 3.

By solving Equation (2.25) for temperature, we obtain

$$\frac{1}{T} = \frac{\lambda_1 \lambda_2}{C_2(\lambda_1 - \lambda_2)} \left[ \ln\left(\frac{S_2}{S_1}\right) + \ln\left(\frac{K_1}{K_2}\right) + \ln\left(\frac{R_1}{R_2}\right) + 5 \ln\left(\frac{\lambda_2}{\lambda_1}\right) + \ln\left(\frac{\varepsilon(\lambda_1)}{\varepsilon(\lambda_2)}\right) \right] \quad (2.26)$$

Although Equation (2.26) has the temperature-dependent term  $K(\lambda_1, T)/K(\lambda_2, T)$  in its right-hand side, it can be solved iteratively, because the dependence of this term on temperature is very weak. It should also be noted that in the case of a graybody radiator with  $\varepsilon(\lambda_1) = \varepsilon(\lambda_2)$  Equation (2.26) does not include the value of the target emissivity. Therefore, the method of ratio radiometry can be used to determine the temperature of a graybody radiator with unknown emissivity. Furthermore, the target need not to be totally gray; it is sufficient for the target to have just two spectral regions where the spectral emissivities are equal. Moreover, even if the target is occluded by spectrally non-selective transparent media the results given by the method of ratio radiometry will still be correct.

It has already been mentioned that ratio radiometry yields the correct temperature for the case of graybody radiators. However, if the spectral emissivities of the target  $\varepsilon(\lambda_1)$  and  $\varepsilon(\lambda_2)$  are not exactly equal, then the measured temperature will differ from the true temperature of the target. The magnitude of this error can be estimated from Equation (2.26) and is given by [12,13]

$$\Delta T_{\varepsilon_1 \neq \varepsilon_2} = \frac{\lambda_1 \cdot \lambda_2 \cdot T^2 \cdot \ln\left(\frac{\varepsilon(\lambda_1)}{\varepsilon(\lambda_2)}\right)}{\lambda_1 \cdot \lambda_2 \cdot T \cdot \ln\left(\frac{\varepsilon(\lambda_1)}{\varepsilon(\lambda_2)}\right) + C_2(\lambda_1 - \lambda_2)} \quad (2.27)$$

However, assuming true graybody radiator, the accuracy of ratio radiometry is determined by the noise level of the detected signals.

To estimate the effect of radiation shot noise on the accuracy of the ratio radiometry

we note that the noise levels of both signals  $S(\lambda_1)$  and  $S(\lambda_2)$  have to be taken into account.

Since the signal measurements at two wavelengths are independent of each other we can express the accuracy of the temperature measurement as

$$\Delta T_{\lambda_1, \lambda_2} = \left[ \left( \frac{dT}{dS_1} \cdot \Delta S_1 \right)^2 + \left( \frac{dT}{dS_2} \cdot \Delta S_2 \right)^2 \right]^{\frac{1}{2}} \quad (2.28)$$

where from Equation (2.26)

$$\left| \frac{dT}{dS_i} \right| = \frac{\lambda_1 \cdot \lambda_2}{C_2 \cdot (\lambda_1 - \lambda_2)} \cdot \frac{T^2}{S_i} \quad (2.29)$$

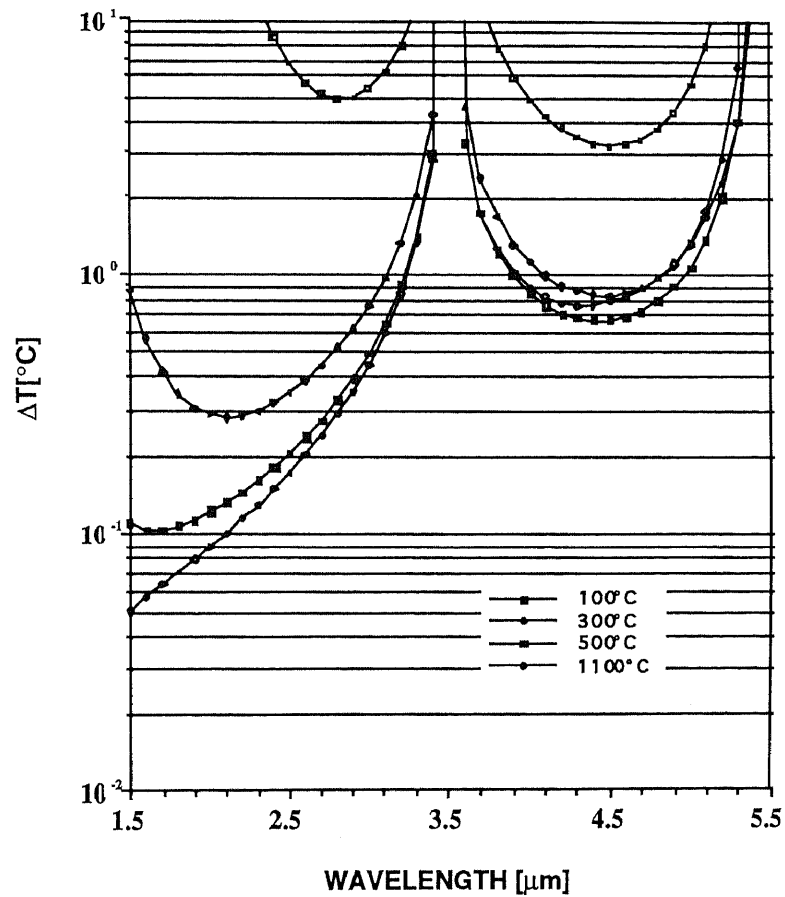


**Figure 2.7** Calculated accuracy of ratio pyrometry for 320x244 IR CCD camera operating with optical integration time of 33 ms, f/2 optics, and 20 nm Gaussian filters

The values of  $\Delta T_{\lambda_1, \lambda_2}$  corresponding to the positioning of one of the filters at  $3.5\mu\text{m}$  and the second filter at various wavelength are shown in Figure 2.7. These computations were performed for 320x122 IR CCD camera operating with optical integration time of 33 ms, f/2 optics, and 20-nm-wide Gaussian filters.

The analysis of Equations (2.27) and (2.28) shows that the effects of shot noise and emissivity variations on the accuracy of temperature measurement are minimized by proper selections of the filters. In particular, the increase in the separation of the filter wavelengths leads to improvement of  $\Delta T$ . On the other hand, it can be seen from Equations (2.27) and (2.28) that for a given wavelength separation, smaller values of the product  $\lambda_1 \cdot \lambda_2$  correspond to better accuracy.

#### 2.5.4 Multi-Wavelength Radiometry

The extensive study of the radiometric literature shows that there exists a wide variety of methods designed to circumvent the problem of unknown emissivity. Some of these methods (e.g. ratio radiometry) provide satisfactory results if certain, usually rather restrictive, assumptions about the spectral emissivity of the target are met. Other methods (referred to as multi-wavelength radiometry) require more extensive measurements but provide acceptable results without placing substantial restrictions on the shape of the spectral emissivity curve.

It would appear that most of the multi-wavelength radiometric techniques can be divided into two general classes [17]. The methods in the first class can be described as "interpolation based techniques", where the spectral radiance of the target is being measured at  $n+1$  distinct wavelengths and these measurements are being used in order to determine the unknown temperature of the radiant target and  $n$  parameters of the particular emissivity model. The methods in the second class are referred to as "least-square-based techniques", where the radiant measurements are made at  $m$  wavelengths, such that  $m > n$ , where  $n$  is the number of unknowns in the model. The redundancy in the data obtained here

is used to smooth out the effects of noise in the data and allow more accurate estimation of the spectral emissivity.

The "interpolation based techniques" can be further separated into two distinct approaches. Some of these methods lead to evaluation of both temperature and emissivity [18, 19], while others provide the target temperature by elimination of the emissivity parameters [20]. The latter methods are referred to as ratio radiometry. It should be noted that the theoretical errors associated with the interpolation methods which provide both temperature and emissivity have been analyzed by Coates [18]. The analysis given in [18] shows that when the number of unknowns  $n > 3$  the accuracy of these methods is unacceptable.

## CHAPTER 3

### MULTI-WAVELENGTH IMAGING PYROMETRY (M-WIP)

#### 3.1 Basic Concepts of Least-Squares-Based M-WIP

The technique of ratio radiometry described in the previous Chapter belongs to the class of radiometric methods which are designed to circumvent the problem of the unknown emissivity by eliminating the emissivity term from the ratios of the measured signals [12,13,20]. These techniques have not, in general, provided adequately accurate temperature estimates for broad industrial usage [19]. The often large inaccuracies of ratio techniques have been attributed to the fact that they require the unrealistic assumption of constant spectral emissivity of the target. The multi-wavelength least-squares-based technique presented here is more robust since it is based on a realistic assumption of a wavelength-dependent emissivity function.

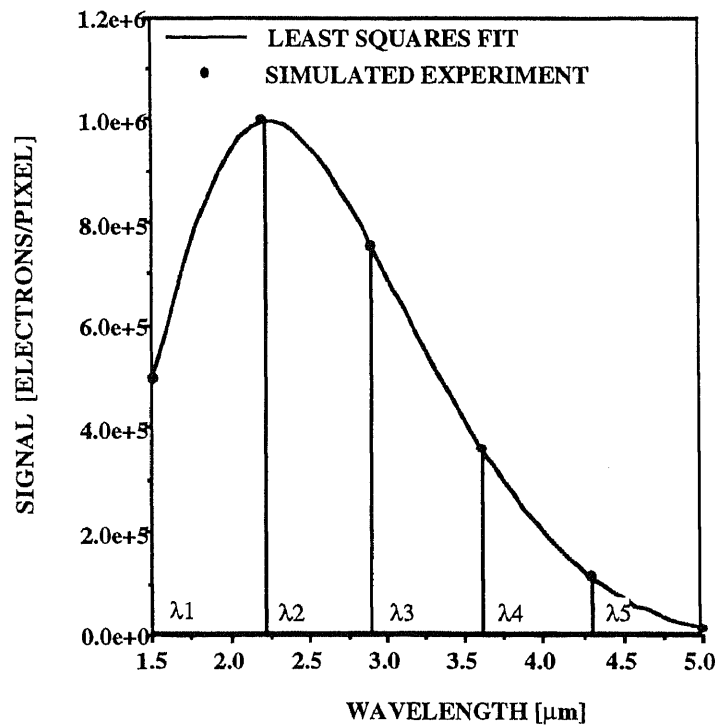


**Figure 3.1** Illustration of the least-squares fit performed by M-WIP for simulated signal

In the case of temperature measurements by Multi-Wavelength Imaging Pyrometer (M-WIP) the spectral radiance of the target is measured at  $N$  distinct wavelengths, as illustrated in Figure 3.1. Based on these measurements the temperature and emissivity of the target are determined simultaneously from the least-squares fit of the signal given by the radiometric model of the IR camera to the experimental data. It should be noted that in order to obtain meaningful results, the number of wavelengths,  $N$ , should exceed the number of unknown parameters of the theoretical model [21]. In its most general form, the least-squares minimization problem of M-WIP can be expressed as:

$$\min_{T, \mathbf{\epsilon}} \chi^2 = \min_{T, \mathbf{\epsilon}} \sum_{i=1}^N \left\{ \frac{1}{\sigma_i^2} \left[ S_i - \tilde{S}(T, \mathbf{\epsilon}, \lambda_i) \right]^2 \right\} \rightarrow T, \mathbf{\epsilon}(\lambda) \quad (3.1)$$

where:

$S_i$  – detected signal at  $\lambda_i$  (electrons/pixel),

$\tilde{S}(T, \mathbf{\epsilon}, \lambda)$  – theoretical signal at  $\lambda$  (electrons/pixel),

$T$  – unknown temperature of the target (K),

$\mathbf{\epsilon} = \mathbf{\epsilon}(\lambda)$  – emissivity model,

$\sigma_i = \Delta S_i = \sqrt{\overline{S_i}} - \text{rms signal noise (rms electrons/pixel)}$

It can be shown that the accuracy of the least squares based M-WIP temperature measurement strongly depends on the selected emissivity model [12]. In order to correctly determine the temperature of the target with unknown emissivity, it is necessary to provide a sufficiently complex and flexible emissivity model that is capable of accurately approximating the target spectral emissivity. On the other hand, a too complex, overdetermined model, will lead to a decrease in the resulting temperature accuracy of the measurement due to the redundant degrees of freedom which it introduces in the fitting algorithm. Analysis of the published data on the spectral emissivity of various materials



[22,23] shows that in most cases the spectral emissivity can be adequately represented by a polynomial function of wavelength:

$$\varepsilon(\lambda) = a_0 + a_1 \cdot \lambda + a_2 \cdot \lambda^2 + \dots \quad (3.2)$$

where  $a_0, a_1, a_2, \dots$  are the parameters of the emissivity model.

However, our theoretical and experimental studies [24] of the spectral emissivity of silicon using Fourier Transform Infrared (FTIR) Spectroscopy indicate that the emissivity is most accurately approximated by polynomial functions of wavenumber as:

$$\varepsilon(\lambda) = a_0 + \frac{a'_1}{\lambda} + \frac{a'_2}{\lambda^2} + \dots \quad (3.3)$$

### 3.2 Real-Time M-WIP Algorithm

It might be noted that in the case of M-WIP, Equation (3.1) calls for minimization of the weighted sum of squares of differences between the theoretical and experimental values of the detected signal, where the points with higher values of the rms shot noise are given less weight. This minimization is performed in real time using the combination of Levenberg-Marquardt and a simulated annealing algorithm as follows:

- Starting from the initial “guess” of the target temperature and emissivity, the minimization algorithm descends into the proximity of the minima using Levenberg-Marquardt method [21]. This method, being somewhat similar to the method of steepest descent, utilizes the derivatives of the minimized function and often yields quick descent during its first few steps. However, Levenberg-Marquardt method finds, in general, local rather than global minima.
- After the first few steps the minimization is handled by the method of simulated annealing. The basic idea of this method originates from the fact, that slowly cooled

liquids are able to arrange its molecules, through random Brownian motion, as to produce near-perfect crystals corresponding to low-energy state of the system. Drawing on this analogy, simulated annealing algorithm generates random perturbations of the system state, accepting new states with probability given by the Boltzmann probability distribution. As the algorithm parameter, known as annealing temperature, is progressively lowered, the probability of accepting new states with higher energy is decreased. It can be shown that, given sufficient number of steps, the method of simulated annealing converges to global, rather than local minima [25].

### 3.2.1 Levenberg-Marquardt Method

As mentioned above, the Levenberg-Marquardt method employed at the beginning of M-WIP minimization procedure represents the combination of so-called steepest descent and inverse-Hessian methods. This iterative method attempts to find the minimum of the surface given by Equation (3.1) by repeatedly solving the following set of linear equations:

$$\sum_{l=1}^M \alpha'_{kl} \cdot \delta a_l = \beta_k \quad (3.4)$$

where:

$a_l$  – is the  $l$  – th parameter of the minimization,

$M$  – is the number of minimization parameters,

$$\beta_k = -\frac{1}{2} \frac{\partial \chi^2}{\partial a_k},$$

$$\alpha'_{jj} = \alpha_{jj}(1 + \lambda),$$

$$\alpha'_{jk} = \alpha_{jk}, \text{ for } j \neq k,$$

$$\alpha_{kl} = \frac{1}{2} \frac{\partial^2 \chi^2}{\partial a_k \partial a_l},$$

$\lambda$  – is the non – dimensional step factor.

The main premise of Levenberg-Marquardt algorithm is that for large values of the step parameter  $\lambda$  the matrix  $\alpha$  becomes predominantly diagonal, effectively making the method to be identical to the method of steepest descent with the iterative step given by:

$$\delta a_1 = \text{constant} \times \beta_1 \quad (3.5)$$

On the other hand, for small values of the step parameter  $\lambda$ , the matrix  $\alpha$  becomes equal to one-half of the Hessian matrix, forcing the Levenberg-Marquardt algorithm to jump to the minimum of the parabolic approximation of  $\chi^2$ , defined by:

$$\chi^2(\mathbf{a}) \approx \gamma - \mathbf{d} \cdot \mathbf{a} + \mathbf{a} \cdot \alpha \cdot \mathbf{a} \quad (3.6)$$

with minimum,  $\mathbf{a}_{\min}$ , at:

$$\mathbf{a}_{\min} = \mathbf{a}_{\text{current}} + 2 \cdot \alpha \cdot \left[ -\nabla \chi^2(\mathbf{a}_{\text{current}}) \right] \quad (3.7)$$

where  $\mathbf{d}$  is an M-vector and  $\gamma$  is a constant.

The following iterative procedure represents one possible implementation of the above algorithm [21]:

1. Compute  $\chi^2(\mathbf{a})$  and pick modest value of  $\lambda$ , say  $\lambda=0.001$ .
2. Solve Equation (3.4) for  $\delta \mathbf{a}$  and evaluate  $\chi^2(\mathbf{a}+\delta \mathbf{a})$ .
3. If  $\chi^2(\mathbf{a}+\delta \mathbf{a}) \geq \chi^2(\mathbf{a})$ , increase  $\lambda$  by a factor of 10 and return to step 2.
4. If  $\chi^2(\mathbf{a}+\delta \mathbf{a}) < \chi^2(\mathbf{a})$ , decrease  $\lambda$  by a factor of 10, update trial solution  $\mathbf{a} \leftarrow \mathbf{a}+\delta \mathbf{a}$  and return to step 2.
5. Stop whenever  $\chi^2$  decreases by a negligible amount.

### 3.2.2 Method of Simulated Annealing

As was mentioned above the method of simulated annealing, employed at the later stages of M-WIP algorithm, represents the technique for global minimization of non-linear functions of multiple variables. Typical annealing algorithm consists of the formula for the calculation of the system energy, random number generator for imitation of the Brownian motion of the system parameters, annealing schedule prescribing the algorithm for gradual reduction of the annealing temperature, and the stopping condition [21,25].

For the purpose of M-WIP temperature estimation the simulated annealing algorithm is implemented as follows:

1. The energy state of the system at the k-th step,  $E(\mathbf{a}_k)$ , is computed as the weighted sum of squares of differences between modeled and measured signals from:

$$E(\mathbf{a}_k) = \chi^2 = \sum_{i=1}^M \left\{ \frac{1}{\sigma_i^2} \left[ S_i - \tilde{S}(\mathbf{a}_k) \right]^2 \right\} \quad (3.8)$$

where vector  $\mathbf{a}_k$  represents M M-WIP parameters (temperature and parameters of emissivity model) at the k-th step of the algorithm.

2. The algorithm parameter  $T_a$ , known as the annealing temperature, is set to a value proportional to  $E(\mathbf{a}_0)$ .
3. Next, the random fluctuation of parameters,  $\delta \mathbf{a}$  (with magnitude proportional to  $E(\mathbf{a}_k)$ ), is presented to the system and  $E(\mathbf{a}_{k+1}) = E(\mathbf{a}_k + \delta \mathbf{a})$  is evaluated.
4. If the energy of the new state  $E(\mathbf{a}_{k+1})$  is lower than  $E(\mathbf{a}_k)$ , then the new state  $\mathbf{a}_k + \delta \mathbf{a}$  is accepted. If, however,  $E(\mathbf{a}_{k+1}) > E(\mathbf{a}_k)$ , then the new state is accepted with probability

$$P(E(\mathbf{a}_{k+1})) = \exp \left[ \frac{E(\mathbf{a}_k) - E(\mathbf{a}_{k+1})}{K_B \cdot T_a} \right] \quad (3.9)$$

where  $K_B$  is the Boltzmann constant.

5. The steps 3 and 4 are repeated for a predetermined (large) number of iterations, allowing the system to reach “thermal equilibrium” at current annealing temperature,  $T_a$ , i.e. the state in which the probability of the system to have an energy  $E(T_a)$  is given by the Boltzmann distribution.
6. After a specified number of iterations the annealing temperature,  $T_a$ , is slowly lowered in accordance with selected annealing schedule, say  $T_{k+1} = \mu T_k$ , where  $\mu < 1$ .
7. The steps 3 through 6 are repeated until annealing temperature,  $T_a$ , becomes very small or the system energy is no longer changing.

### 3.3 General Configuration of M-WIP Systems

Block diagrams of two embodiments of the Multi-Wavelength Imaging Pyrometer (M-WIP) illustrating this invention are shown in Figure 3.2 and Figure 3.3 [26]. The Multi-Wavelength Imaging Pyrometer for non-contact real-time measurements of temperature and emissivity profiles of radiant targets with unknown spectral emissivity includes: an assembly of multiple narrow-band optical filters, an array of photodetectors sensitive to the transmission bands of the optical filters, optical means for imaging the radiant target through an assembly of multiple narrow-band optical filters on an array of photodetectors for producing multi-wavelength images of the radiant target; an array of photodetectors sensitive to the main transmission bands of the optical filters, and means for processing the detected multi-wavelength images of the radiant target using a model of the radiant target for determining the temperature and emissivity profiles on the radiant target. It should be noted that the difference between two embodiments illustrated in Figure 3.2 and Figure 3.3 is that in the case illustrated in Figure 3.2 the filters are in close proximity to the detectors, while in case illustrated in Figure 3.3 the target radiation is refocused on the photodetectors by means of the relay lens.

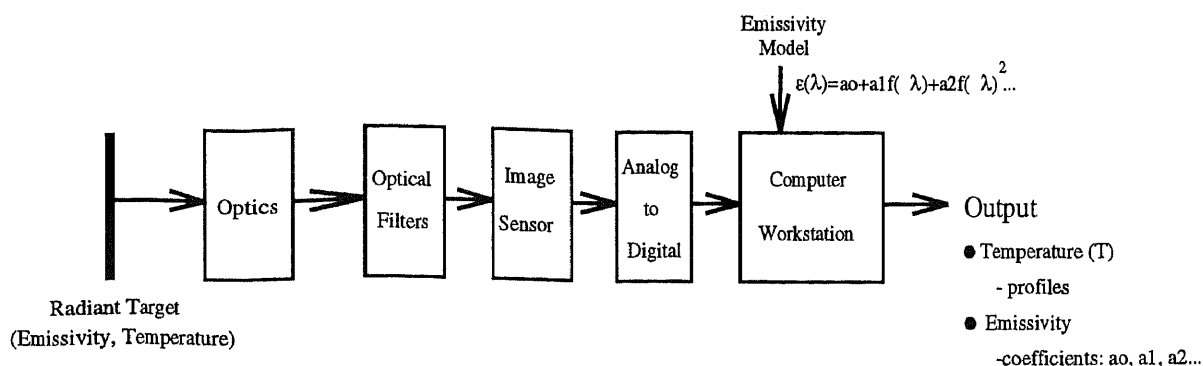


**Figure 3.2** Schematic diagram of Multi-Wavelength Imaging Pyrometer with optical filters positioned in close proximity of the array of photodetectors

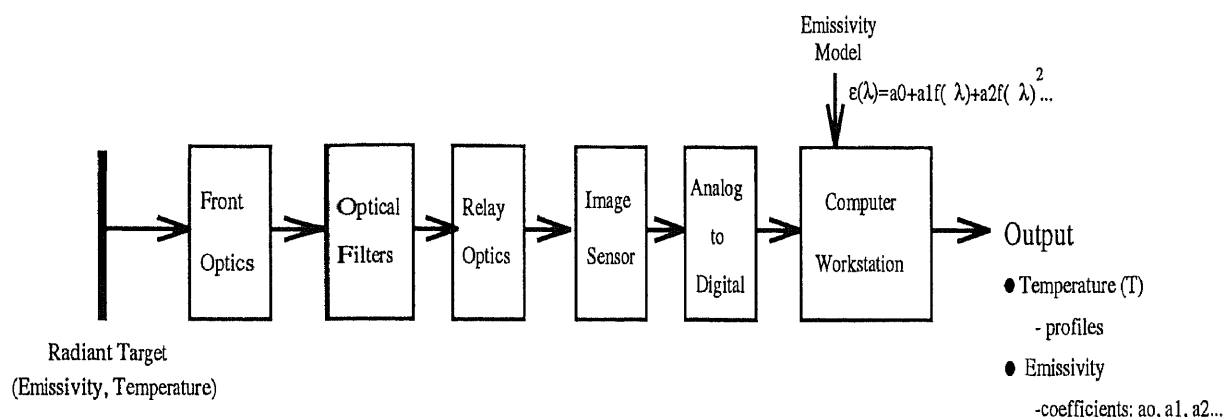
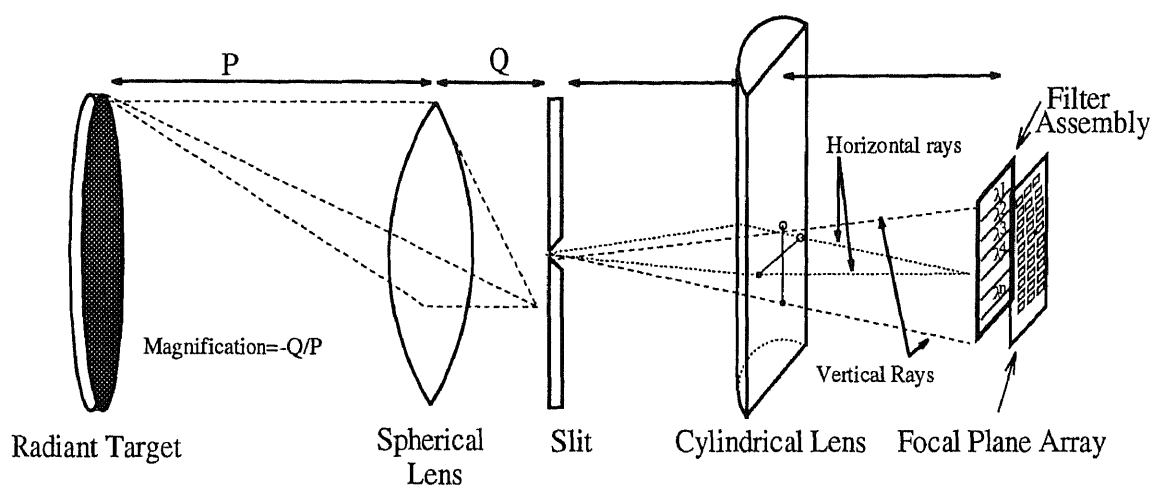


**Figure 3.3** Schematic diagram of Multi-Wavelength Imaging Pyrometer with relay optics used to refocus optical filters onto the array of photodetectors

### 3.4 M-WIP Filter Optics

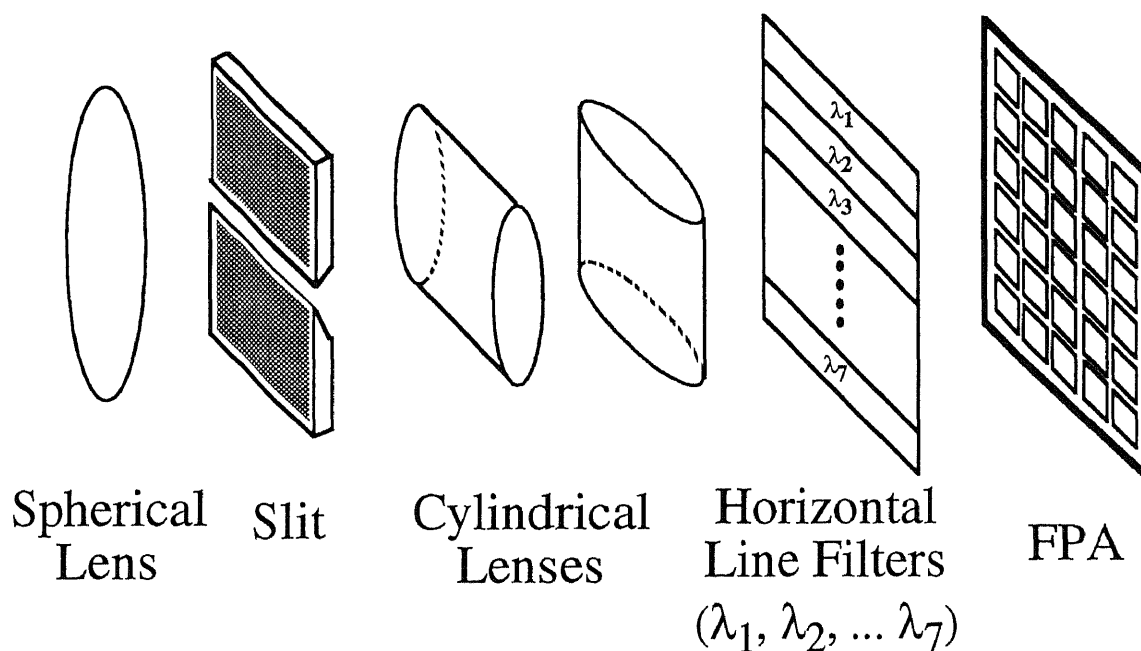
One of the most crucial elements of any Multi-Wavelength Imaging Pyrometer is the selection of IR filters and associated optics. The various filter-optics configurations suitable for area-sensing, line-sensing and point-sensing M-WIPs are illustrated below.

Figure 3.4 illustrates the Multi-Wavelength Imaging Pyrometer equipped with “line-sensing” assembly of striped narrow-band IR filters positioned in front of the focal plane array (FPA) of an image sensor. In this case the spherical lens is employed for focusing of the image of the radiant target on the narrow optical slit. The image of the target area defined by the slit is then refocused on the FPA using cylindrical lens.



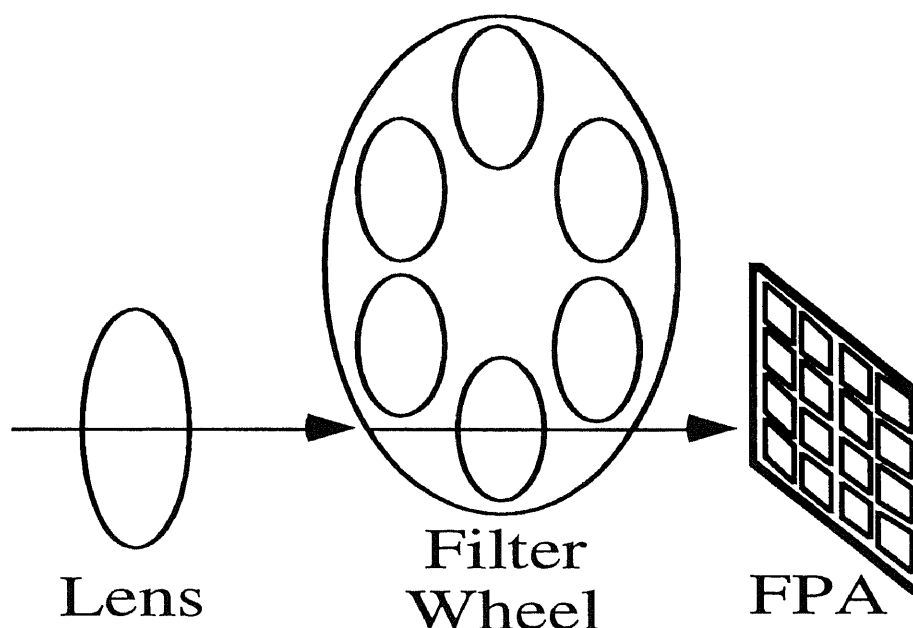
**Figure 3.4** Line-sensing M-WIP configuration with one cylindrical lens

Figure 3.5 illustrates the use of an additional cylindrical lens to magnify the image of the target area defined by the slit, in the direction perpendicular to the slit opening, and to project it on the array of striped filters.



**Figure 3.5** Line-sensing M-WIP configuration with two cylindrical lenses

Figure 3-6 illustrates area-sensing M-WIP with rotating filter wheel used to measure the spectra of the target radiation one wavelength at a time. This configuration utilizes spherical optics to image the target on the FPA and allows two-dimensional sensing of temperature and emissivity profiles on the target.



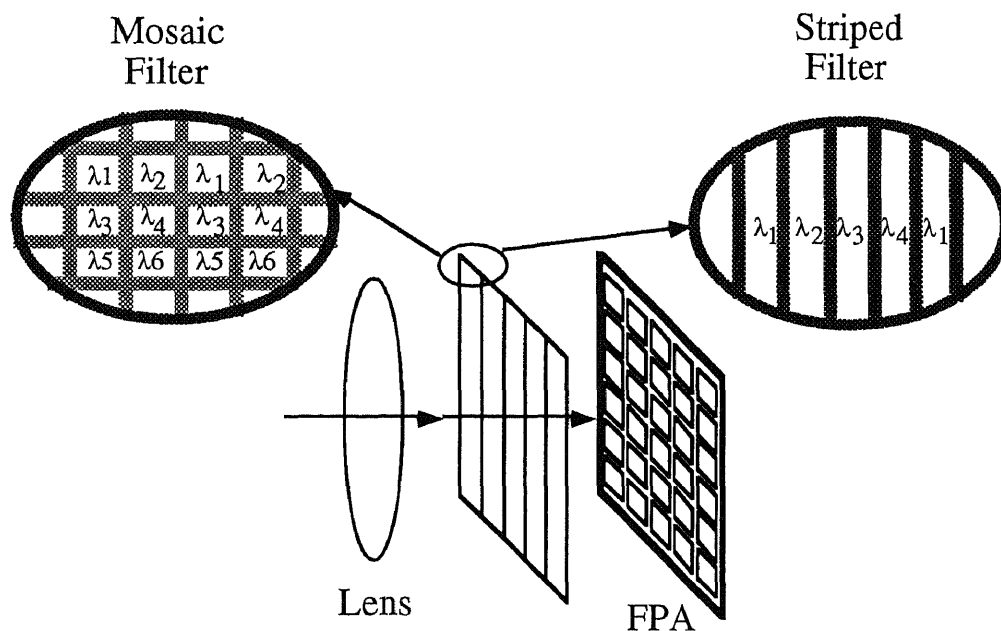
**Figure 3-6** Area-sensing M-WIP configuration utilizing rotating filter wheel

Figure 3.7 illustrates M-WIP configuration in which a set of  $n$  distinct filters is associated with each macropixel, where each macropixel is composed of  $n$  imager photodetectors. This configuration utilizes spherical optics to focus the image of the target on the FPA and facilitates two-dimensional sensing of temperature and emissivity profiles on the target surface.

Figure 3.8 illustrates M-WIP configuration suitable for measurement of temperature and emissivity profiles on the targets obscured from direct observation by opaque objects. In this configuration the fiber bundles with radiation collection optics are used to transmit the thermal radiation from the target to individual optical filters of filter assembly. In this



case  $m$  fiber-optic bundles containing  $n$  optical fibers each are used to image  $m$  target points on  $m \times n$  photodetectors through  $n$  optical filters, where each fiber bundle transmits radiation from one of  $m$  target points to  $n$  optical filters. It should be noted that larger number of detectors than  $m \times n$  can also be used, with several detectors grouped together to produce a single output signal.



**Figure 3.7** Area-sensing M-WIP configuration based on mosaic and striped filter assemblies

Figure 3.9 illustrates another fiber-optic-based M-WIP configuration where  $m$  individual optical fibers equipped with radiation collecting optics are used to collect thermal radiation from  $m$  target points. A cylindrical optics is then utilized to project the output of  $m$  individual optical fibers across an assembly of  $n$  narrow-band striped optical filters in one direction and to refocus the image of each optical fiber on the  $m$  sets (columns) of photodetectors in another direction.

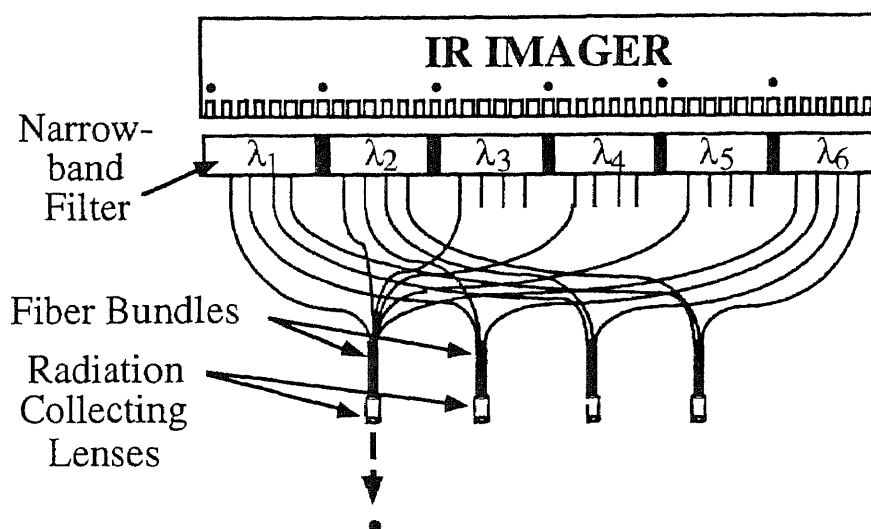


**Figure 3.8** Point-sensing M-WIP utilizing fiber bundles to transmit target radiation directly to individual optical filters of filter assembly

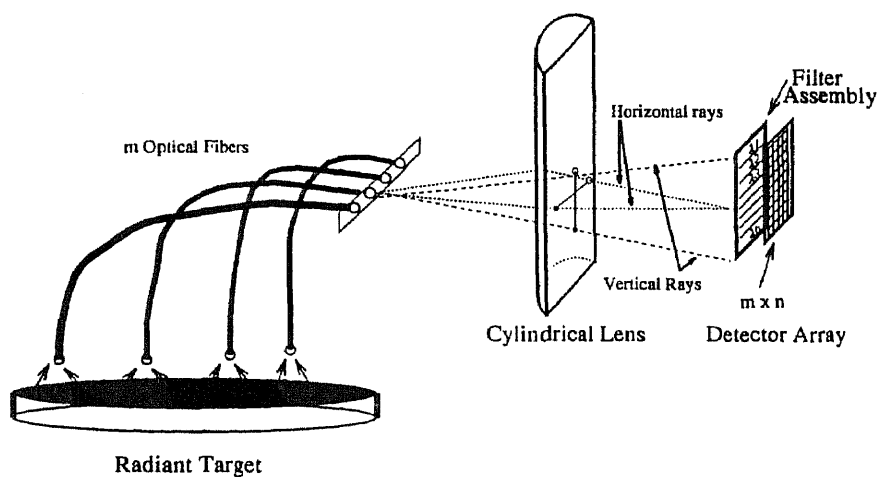


**Figure 3.9** Point-sensing M-WIP utilizing fiber bundles and cylindrical optics to transmit target radiation to the filter assembly

Finally, Figure 3.10 and Figure 3.11 illustrate point-sensing M-WIP configuration where the image of the radiant target may be focused on a point aperture; the image of the target point defined by the aperture is then projected by the collimating optics on a line array of  $n$  photodetectors through  $n$  filters as shown in Figure 3.10 or on a two-dimensional

array of  $n$  photodetectors through a two-dimensional array of  $n$  optical filters, where the filter array is of the same size as the detector array and is in the close proximity to the detector array, as shown in Figure 3.11. Alternatively, the slit may be positioned on a uni-directional translation stage for line-scanning or on bi-directional translation stage for area scanning of target temperature profiles.

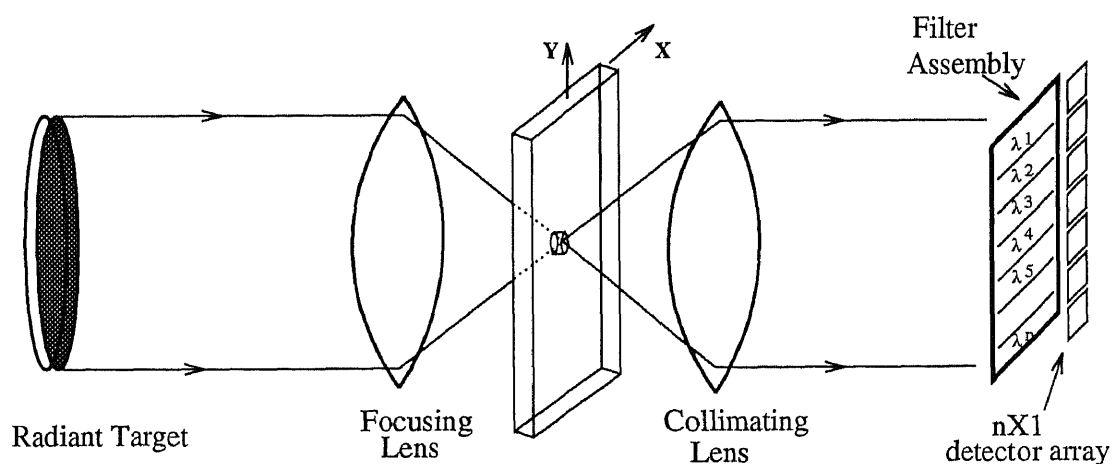


**Figure 3.10** Point-sensing M-WIP with point aperture and 1-D detector array

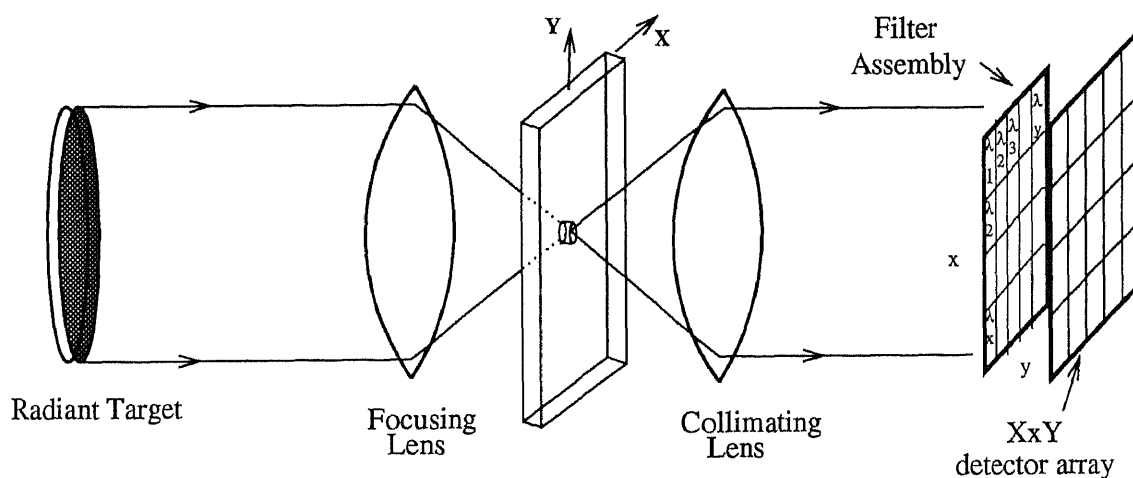


**Figure 3.11** Point-sensing M-WIP with point aperture and 2-D detector array

### 3.5 Radiometric Model of M-WIP Sensor

Equation (2.19) represents the most general form of the theoretical model of the signal detected by the IR imager and can, in principle, be utilized for the least-squares-based M-WIP computations. However, for an M-WIP system with an assembly of  $N$  IR filters the single temperature measurement would require the numerical integration specified by Equation (2.19) to be performed  $N$  times! The computational burden of numerical integration would virtually preclude multi-point (area) real-time M-WIP temperature monitoring. Therefore, there is a need to develop radiometric model of multi-wavelength imaging pyrometer that would yield sufficient accuracy without requiring on-line numerical integration.

Fortunately, a number of methods designed to provide an approximate analytical solution of Equation (2.19) have been described in the radiometric literature. Among these methods the technique developed by Coates [27] provides very high accuracy of the solution when the fractional bandwidth of the filter,  $\Delta\lambda/\lambda$ , is less than 0.1. It should be noted that this technique, known as *reference wavelength* method, in addition to high accuracy and ease of interpretation, provides the means to account for the variation of spectral emissivity across the passband of the filter. This *reference wavelength* method is based on the description of the spectral transmission of a narrow-bandpass filter in terms of the moments of its spectral transmittance,  $\tau(\lambda)$ , about the mean wavelength of the filter,  $\lambda_0$ .

Following the development by Coates we define the  $n^{\text{th}}$  moment of the transmittance,  $a_n$ , by

$$\int_0^{\infty} (\lambda - \lambda_0)^n \cdot \tau(\lambda) d\lambda = a_n \cdot \tau(\lambda_0) \cdot (\Delta\lambda)^{n+1} \quad (3.10)$$

where  $\Delta\lambda$  - is the bandwidth of the filter at half of its peak transmittance.

It can be noted that the moments reflect the shape of the filter and are independent of the peak transmission,  $\tau_0$ , and the filter width  $\Delta\lambda$ . Since the reference wavelength,  $\lambda_0$ , is taken as the mean wavelength of the filter, the first moment,  $a_1$ , is zero by definition.

The output signal of the IR imager viewing radiant target with temperature  $T$  and spectral emissivity  $\varepsilon(\lambda)$  can now be described to a good first approximation by:

$$S_0(T) = A_{d,n} \cdot \omega_d \cdot a_0 \cdot \tau(\lambda_0) \cdot \Delta\lambda \cdot R(\lambda_0) \cdot \varepsilon(\lambda_0) \cdot L_{\lambda,b}(\lambda_0, T) \quad (3.11)$$

where the factor  $a_0$  has been included to make the product  $a_0 \tau(\lambda_0) \Delta\lambda$  equal to the area under the  $\tau(\lambda)$  curve. We now define the correction factor  $C(T)$  as

$$C(T) = \frac{S(T)}{S_0(T)} = \int_0^\infty \frac{\tau(\lambda)}{a_0 \tau(\lambda_0) \Delta\lambda} \cdot \frac{R(\lambda)}{R(\lambda_0)} \cdot \frac{\varepsilon(\lambda)}{\varepsilon(\lambda_0)} \cdot \frac{L_{\lambda,b}(\lambda, T)}{L_{\lambda,b}(\lambda_0, T)} \cdot d\lambda \quad (3.12)$$

Once the correction factor  $C(T)$  has been determined, the signal  $S(T)$  can be obtained from the computed signal  $S_0(T)$ . Each of the factors in the integrand, except that involving the filter transmission, is now expanded in a Taylor series about reference wavelength  $\lambda_0$

$$\frac{R(\lambda)}{R(\lambda_0)} = 1 + r_1 \cdot (\lambda - \lambda_0) + r_2 \cdot (\lambda - \lambda_0)^2 + \dots \quad (3.13)$$

$$\frac{\varepsilon(\lambda)}{\varepsilon(\lambda_0)} = 1 + \varepsilon_1 \cdot (\lambda - \lambda_0) + \varepsilon_2 \cdot (\lambda - \lambda_0)^2 + \dots \quad (3.14)$$

and

$$\frac{L_{\lambda,b}(\lambda, T)}{L_{\lambda,b}(\lambda_0, T)} = 1 + L_1 \cdot (\lambda - \lambda_0) + L_2 \cdot (\lambda - \lambda_0)^2 + \dots \quad (3.15)$$

where

$$r_n = \frac{1}{n!R(\lambda_o)} \cdot \frac{d^n R(\lambda)}{d\lambda^n} \quad (3.16)$$

$$\varepsilon_n = \frac{1}{n!\varepsilon(\lambda_o)} \cdot \frac{d^n \varepsilon(\lambda)}{d\lambda^n} \quad (3.17)$$

and

$$L_n(T) = \frac{1}{n!L_{\lambda,b}(\lambda_o, T)} \cdot \frac{d^n L_{\lambda,b}(\lambda, T)}{d\lambda^n} \quad (3.18)$$

Expressions for  $L_1(T)$  and  $L_2(T)$  can be obtained by differentiating the Planck's distribution function to find

$$\lambda_o \cdot L_1(T) = \frac{x e^x}{(e^x - 1)} - 5 \quad (3.19)$$

$$\lambda_o^2 \cdot L_2(T) = \frac{x^2 e^x}{(e^x - 1)^2} + \frac{[(x^2 / 2) - 6x] \cdot e^x}{(e^x - 1)} + 15 \quad (3.20)$$

where

$$x = \frac{C_2}{\lambda_o T} \quad (3.21)$$

The computations performed for Gaussian filter with fractional bandwidth  $\Delta\lambda/\lambda_o=0.05$  and target temperatures between 100 °C and 1000 °C show that  $L_3(T)$  and  $L_4(T)$  enter only those terms of  $C(T)$  which constitute less than 0.49% of its absolute value [12]. Therefore,  $L_3(T)$  and  $L_4(T)$  can be sufficiently accurately evaluated by using Wien's law as

$$\lambda_o^3 \cdot L_3(T) = \frac{x^3}{6} - \frac{7x^2}{2} + 21x - 35 \quad (3.22)$$

$$\lambda_o^4 \cdot L_4(T) = \frac{x^4}{24} - \frac{4x^3}{3} + 14x^2 - 56x + 70 \quad (3.23)$$

Equations (3.16) through (3.23) are now substituted into Equations (3.13)-(3.15), and those expressions are in turn substituted into Equation (3.12). After the substitution is performed the coefficients of each order of the terms  $[(\lambda - \lambda_o) / \lambda_o]^n$  are collected. Designating the sum of the coefficients of the term of degree  $n$  as  $\Sigma_n(T)$  we can express the correction factor as

$$C(T) = 1 + \Sigma_1(T) \int_0^\infty \frac{(\lambda - \lambda_o) \tau(\lambda) d\lambda}{a_o \tau(\lambda_o) \lambda_o \Delta \lambda} + \Sigma_2(T) \int_0^\infty \frac{(\lambda - \lambda_o)^2 \tau(\lambda) d\lambda}{a_o \tau(\lambda_o) \lambda_o^2 \Delta \lambda} + \dots \quad (3.24)$$

Substituting Equation (3.10) into Equation (3.24) we obtain

$$C(T) = 1 + \Sigma_2(T) \cdot A_2 \cdot \left( \frac{\Delta \lambda}{\lambda_o} \right)^2 + \dots + \Sigma_n(T) \cdot A_n \cdot \left( \frac{\Delta \lambda}{\lambda_o} \right)^n + \dots \quad (3.25)$$

where  $A_n = a_n / a_o$  and  $A_1 = 0$  since  $a_1 = 0$  by definition.

In most practical cases  $\epsilon(\lambda)$  and  $R(\lambda)$  change relatively slow across the passband of the filter and can be accurately represented by the first three terms in Equations (3.13) and (3.14) [27]. Under these conditions the expressions for  $\Sigma_n(T)$  up to  $\Sigma_4(T)$  are found to be as follows

$$\Sigma_1(T) = \lambda_o [L_1(T) + (r_1 + \epsilon_1)] \quad (3.26a)$$

$$\Sigma_2(T) = \lambda_o^2 \cdot [L_2(T) + (r_1 + \epsilon_1) \cdot L_1(T) + (r_2 + r_1 \epsilon_1 + \epsilon_2)] \quad (3.26b)$$

$$\Sigma_3(T) = \lambda_0^3 \cdot [L_3(T) + (r_1 + \epsilon_1) \cdot L_2(T) + (r_2 + r_1\epsilon_1 + \epsilon_2) \cdot L_1(T) + (r_3 + r_2\epsilon_1 + r_1\epsilon_2 + \epsilon_3)] \quad (3.26c)$$

$$\Sigma_4(T) = \lambda_0^4 \cdot [L_4(T) + (r_1 + \epsilon_1) \cdot L_3(T) + (r_2 + r_1\epsilon_1 + \epsilon_2) \cdot L_2(T) + (r_3 + r_2\epsilon_1 + r_1\epsilon_2 + \epsilon_3) \cdot L_1(T) + (r_4 + r_3\epsilon_1 + r_2\epsilon_2 + r_1\epsilon_3 + \epsilon_4)] \quad (3.26d)$$

Moments up to  $A_4$  have been computed by numerical integration for several transmission curves of interest and are given in Figure 3.12. It may be noted that in the case of symmetrical filters,  $A_n$  is zero for odd values of  $n$ . Therefore, for symmetrical filters with moderate bandwidths, the third term in Equation (3.25) is zero. For filters with  $\Delta\lambda/\lambda_0 < 0.1$  the fourth term in Equation (3.25) is at least two orders of magnitude smaller than the second term. In this case the correction factor  $C(T)$  can be approximated by

$$C(T) = 1 + \Sigma_2(T) \cdot A_2 \cdot \left( \frac{\Delta\lambda}{\lambda_0} \right)^2 \quad (3.27)$$

Substituting  $C(T)$  from Equation (3.27) into Equation (3.12) we obtain the expression for the output signal of the imager viewing the radiant surface through the narrow-passband filter

$$S(T) = A_{d,n} \cdot \omega_d \cdot a_o \cdot \tau(\lambda_0) \cdot \Delta\lambda \cdot R(\lambda_0) \cdot \epsilon(\lambda_0) \times \\ \times \left[ 1 + \Sigma_2(T) \cdot A_2 \cdot \left( \frac{\Delta\lambda}{\lambda_0} \right)^2 \right] \cdot L_{\lambda,b}(\lambda_0, T) \quad (3.28)$$

In order to further simplify the expression (3.28) we define the filter shape factor  $K(\lambda_0, T)$  as



$$\begin{aligned}
 K(\lambda, T) &= A_{d,n} \cdot \omega_d \cdot a_o \cdot \tau(\lambda_o) \cdot \Delta\lambda \cdot \left[ 1 + \Sigma_2(T) \cdot A_2 \cdot \left( \frac{\Delta\lambda}{\lambda_o} \right)^2 \right] = \\
 &= G \cdot \left[ 1 + \Sigma_2(T) \cdot A_2 \cdot \left( \frac{\Delta\lambda}{\lambda_o} \right)^2 \right]
 \end{aligned} \tag{3.29}$$

where the geometric factor  $G$  is given by

$$G = A_{d,n} \cdot \omega_d \cdot a_o \cdot \tau(\lambda_o) \cdot \Delta\lambda \tag{3.30}$$

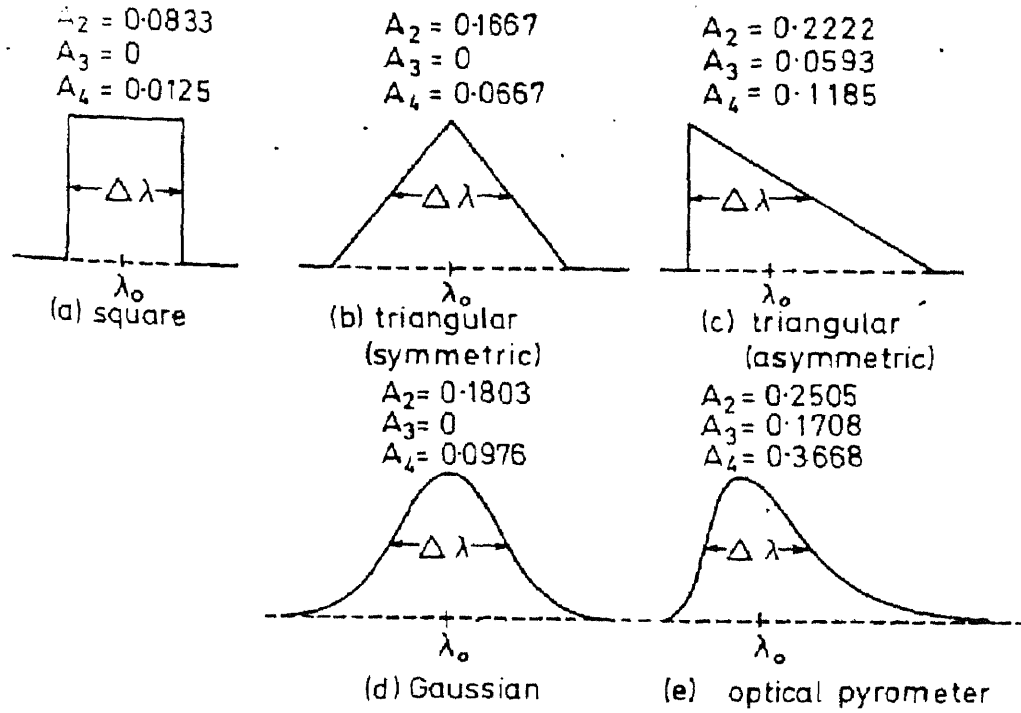


**Figure 3.12** Normalized moments of various filters [27]

Finally, substituting Equation (3.29) into Equation (3.28) we obtain the simplified expression for the output signal of the imager [12]

$$S(\lambda, T) = K(\lambda, T) \cdot \varepsilon(\lambda) \cdot R(\lambda) \cdot L_{\lambda,b}(\lambda, T) \tag{3.31}$$

The accuracy of Equation (3.31) was verified experimentally by measuring the output signal of a 320x122 IR CCD Camera viewing the blackbody radiator through the filter with various mean wavelengths. The blackbody had an aperture of 0.2 inches in diameter and was positioned 18 inches in front of the camera with lens of objective removed. The experimental values of the signal along with the theoretical results based on Equation (3.31) are shown in Figure 3.13. Inspection of the Figure 3.13 shows that there is good agreement between theoretical and experimental data. Nevertheless, slight discrepancies between model and experiment dictate the need for accurate filter and detector calibration which will be discussed in Chapter 6.

The values of the output signal calculated from Equation (3.31) for 320x244 IR CCD camera operating with optical integration time of 33 ms, f/2 optics, and 500-nm-wide Gaussian filter having 60% peak transmission are shown in Figure 3.14. The output signal of the same imager viewing the blackbody radiator through a 20-nm-wide Gaussian filter was calculated for a broad range of temperatures and is shown in Figure 3.15.

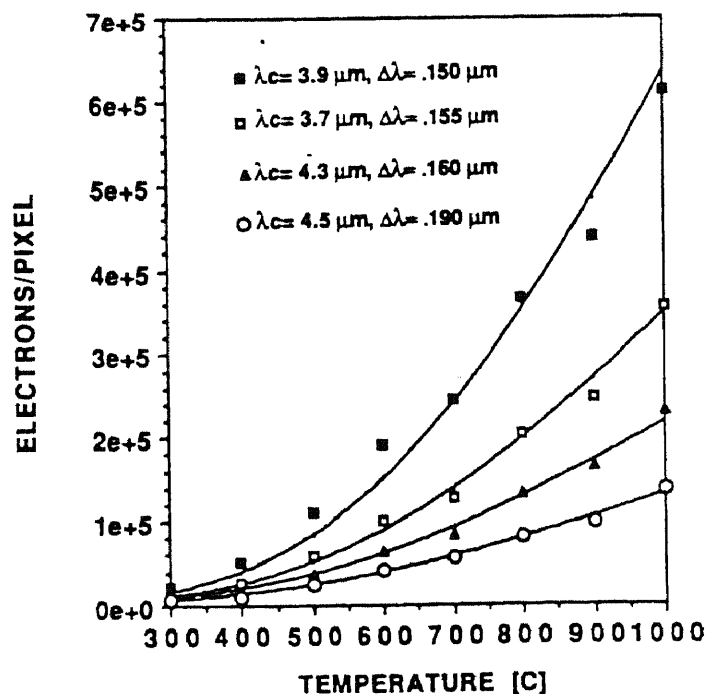


**Figure 3.13** Calculated and measured signal of 320x122 IR-CCD imager without lens

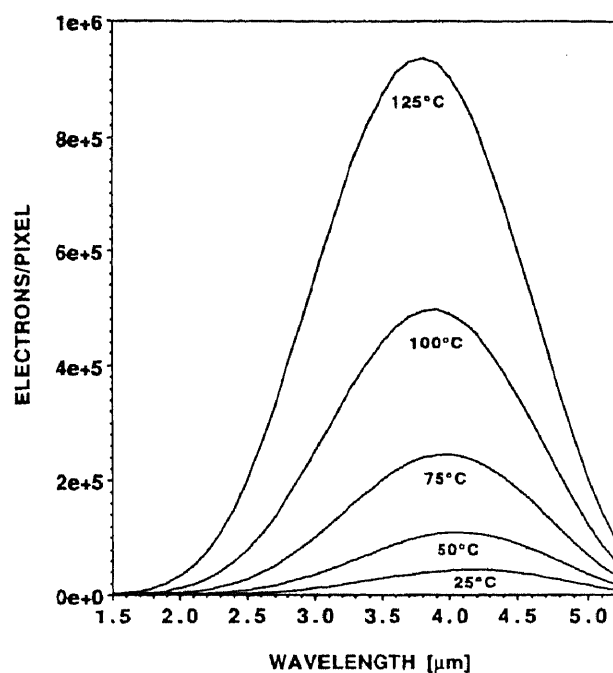


**Figure 3.14** Simulated signal of 320x122 IR-CCD imager operating with integration time of 33 ms,  $f/2$  optics and 500-nm Gaussian filter with 60% peak of transmission

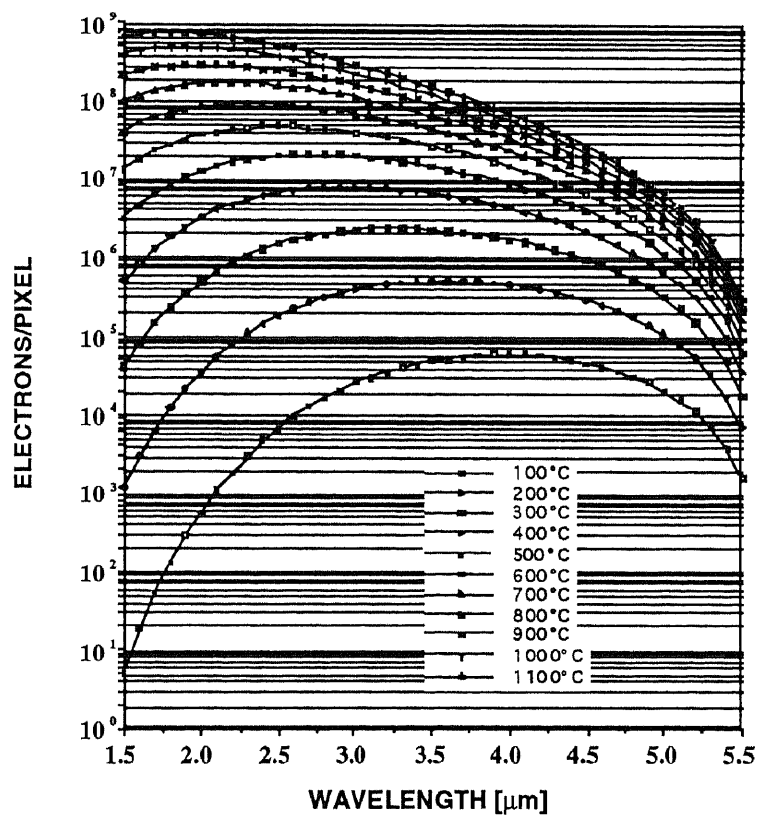


**Figure 3.15** Simulated signal of 320x122 IR-CCD imager operating with integration time of 33 ms,  $f/2$  optics and 20-nm Gaussian filter with 60% peak of transmission

## CHAPTER 4

### PERFORMANCE PREDICTION FOR MULTI-WAVELENGTH PYROMETERS

In this Chapter we will develop the methodology for theoretical prediction of the accuracy of temperature measurements achievable by a variety of M-WIPs. We will also demonstrate this methodology by analyzing the performance of three different M-WIP systems.

#### 4.1 General Methodology of M-WIP Performance Prediction

To estimate the accuracy of M-WIP temperature measurements we will develop the approximate analytical solution to the least-squares-based M-WIP problem defined by Equation (3.1) [12]. Substituting the emissivity model expressed by Equation (3.2) into the expression for the detected signal given by Equation (3.31) we obtain the parametric model of the output signal of the imager viewing the target with unknown emissivity

$$S(\lambda, a_1, \dots, a_n) = K(\lambda, a_1, \dots, a_n) \cdot \varepsilon(\lambda, a_1, \dots, a_n) \cdot R(\lambda) \cdot L_{\lambda, b}(\lambda, a_n) \quad (4.1)$$

where the temperature of the target  $T=a_n$  is also an unknown parameter of the model.

The function  $S(\lambda, a_1, \dots, a_n)$  can be approximated by the Taylor's series expansion at the close proximity of the solution of the minimization problem. Neglecting second and higher order terms, we have

$$S(\lambda) = S_o(\lambda) + \sum_{j=1}^n \left[ \frac{dS_o(\lambda)}{da_j} \cdot \delta a_j \right] + \frac{dS_o(\lambda)}{d\lambda} \cdot \delta \lambda \quad (4.2)$$

The approximate solution to the minimization problem given by Equation (3.1) can be obtained by setting the partial derivatives of  $\chi^2$  with respect to each of the parameter

increments equal to zero

$$-2 \sum_{i=1}^N \left( \frac{1}{\sigma_i^2} \left\{ S_i - S_o(\lambda_i) - \sum_{j=1}^n \left[ \frac{dS_o(\lambda)}{da_j} \delta a_j \right] - \frac{dS_o(\lambda)}{d\lambda} \delta \lambda \right\} \cdot \frac{dS_o(\lambda)}{da_k} \right) = 0 \quad (4.3)$$

where  $\sigma_i$  is the standard deviation of the signal detected at the wavelength  $\lambda_i$  and is equal to the total rms noise level in the signal.

Equation (4.3) can be written in matrix form as

$$\bar{\beta} = \delta \bar{a} \cdot \bar{\alpha} \quad (4.4)$$

where

$$\alpha_{jk} = \sum_{i=1}^N \left( \frac{1}{\sigma_i^2} \cdot \frac{dS_o(\lambda)}{da_j} \cdot \frac{dS_o(\lambda)}{da_k} \right) \quad (4.5)$$

and

$$\beta_k = \sum_{i=1}^N \left( \frac{1}{\sigma_i^2} \left\{ S_i - S_o(\lambda_i) - \frac{dS_o(\lambda)}{d\lambda} \delta \lambda \right\} \cdot \frac{dS_o(\lambda)}{da_k} \right) \quad (4.6)$$

The matrix  $\bar{\alpha}$  is referred to as the "curvature matrix" because of its relationship to the curvature of  $\chi^2$  in the coefficient space. Defining the symmetric matrix  $\bar{\gamma}$  as the inverse of matrix  $\bar{\alpha}$  we can obtain the expression for an approximate solution of the minimization problem given by Equation (3.1) as

$$\delta \bar{a} = \bar{\beta} \cdot \bar{\gamma} \quad \text{or} \quad \delta a_j = \sum_{k=1}^n (\gamma_{jk} \cdot \beta_k) \quad (4.7)$$

where  $\bar{\gamma} = \bar{\alpha}^{-1}$ .

To find the accuracy of the parameter estimation by least-squares fit we note that each of our experimental data points  $S_i$  has been used in the determination of the parameters, and each has contributed some fraction of its own noise to the uncertainty in the computed parameters. Therefore, the accuracy (standard deviation) of any parameter  $a_j$  can be expressed as the square root of the sum of squares of the rms noise levels of each data point multiplied by the effect which that data point has on the determination of the parameter  $a_j$

$$\sigma_{a_j}^2 = \sum_{i=1}^N \sigma_i^2 \cdot \left( \frac{da_j}{dS_i} \right)^2 = \sum_{i=1}^N \sigma_i^2 \cdot \left( \frac{d\delta a_j}{dS_i} \right)^2 \quad (4.8)$$

The partial derivatives of the parameters with respect to each experimental data point can be obtained by differentiating Equation (4.7) as

$$\frac{d\delta a_j}{dS_i} = \sum_{k=1}^n \left[ \gamma_{jk} \cdot \frac{1}{\sigma_i^2} \cdot \frac{dS_o(\lambda)}{da_k} \right] \quad (4.9)$$

Performing the substitution of the partial derivatives given by Equation (4.9) into Equation (4.8) and taking into account the fact that matrix  $\bar{\gamma}$  is the inverse of the matrix  $\bar{\alpha}$  we obtain the final expression for the standard deviations of the parameters of the theoretical model fitted to the experimentally measured values of the detected IR imager signal:

$$\sigma_{a_j}^2 = \sum_{i=1}^N \sigma_i^2 \cdot \left\{ \sum_{k=1}^n \left[ \gamma_{jk} \cdot \frac{1}{\sigma_i^2} \cdot \frac{dS_o(\lambda)}{da_k} \right] \right\}^2 = \gamma_{jj} \quad (4.10)$$

At this point it should be noted that in order to implement the error analysis described above we have to obtain analytical expressions for the partial derivatives of the signal model with respect to each of its parameter.

To derive the expressions of the partial derivatives of the signal model with respect to temperature and wavelength let us define the normalized derivative of the blackbody spectral radiance with respect to temperature as

$$L_T = \frac{1}{L_{\lambda,b}(\lambda_o, T)} \cdot \frac{dL_{\lambda,b}(\lambda, T)}{dT} = \frac{x e^x}{T(e^x - 1)} \quad (4.11)$$

where  $x$  is given by Equation (3.21).

We will also define the relative derivative of the filter shape factor  $K(\lambda, T)$  with respect to temperature as

$$K_T = \frac{1}{K(\lambda, T)} \cdot \frac{dK(\lambda, T)}{dT} \quad (4.12)$$

where  $dK/dT$  can be evaluated by differentiating Equation (3.29) as

$$\frac{dK(\lambda, T)}{dT} = G \cdot A_2 \cdot \left( \frac{\Delta\lambda}{\lambda_o} \right)^2 \frac{d\Sigma_2(T)}{dT} \quad (4.13)$$

The expression for  $d\Sigma_2(T)/dT$  may be obtained by differentiating Equation (3.26b) to find

$$\frac{d\Sigma_2(T)}{dT} = \lambda_o^2 \cdot \left[ \frac{dL_2(T)}{dT} + (r_1 + \varepsilon_1) \cdot \frac{dL_1(T)}{dT} \right] \quad (4.14)$$

where  $L_1$ ,  $L_2$ ,  $r_1$ , and  $\varepsilon_1$  are defined in Equations (3.16) through (3.18).

The values of  $dL_1/dT$  and  $dL_2/dT$  can be evaluated based on Wien's approximation

$$\frac{dL_1(T)}{dT} = \frac{x^2 e^x}{C_2(e^x - 1)} \cdot \left[ \frac{x}{(e^x - 1)} - 1 \right] \quad (4.15)$$

and

$$\frac{dL_2(T)}{dT} = \frac{x}{\lambda^2 T} \cdot [6 - x] \quad (4.16)$$

Finally, we note that  $\epsilon_1$  defined in Equation (3.17) is equal to zero for blackbody radiator and  $r_1$  can be estimated by performing the substitution from Equation (4.29) into Equation (3.16) as

$$r_1 = -\frac{2\Psi_{ms}}{1.24} \cdot \sqrt{\frac{C}{R(\lambda)}} \quad (4.17)$$

At this point we can use Equations (4.11) and (4.12) in order to write the partial derivative of the signal expression given by Equation (3.31) with respect to temperature as follows

$$\begin{aligned} \frac{dS(\lambda, T)}{dT} &= \frac{K(\lambda, T)}{dT} \cdot \epsilon(\lambda) \cdot R(\lambda) \cdot L_{\lambda, b}(\lambda, T) \\ &\quad + K(\lambda, T) \cdot \epsilon(\lambda) \cdot R(\lambda) \cdot \frac{L_{\lambda, b}(\lambda, T)}{dT} \\ &= S(\lambda, T) \cdot [K_T + L_T] \end{aligned} \quad (4.18)$$

We will now derive the expressions for the partial derivatives of the signal model with respect to the parameters of the emissivity model. For the sake of clarity only a linear emissivity model with two unknown parameters  $a$  and  $b$  will be considered. Let us define the relative partial derivatives of the emissivity with respect to the coefficients  $a$  and  $b$  by analogy with Equation (3.17) as

$$\epsilon_a = \frac{1}{\epsilon(a, b)} \cdot \frac{d\epsilon(a, b)}{da} = \frac{1}{\epsilon(a, b)} \quad (4.19)$$

and

$$\epsilon_b = \frac{1}{\epsilon(a, b)} \cdot \frac{d\epsilon(a, b)}{db} = \frac{\lambda_o}{\epsilon(a, b)} \quad (4.20)$$



Similarly, the relative partial derivatives of the shape coefficient  $K(a,b,T)$  can be defined as

$$K_a = \frac{1}{K(a,b,T)} \cdot \frac{dK(a,b,T)}{da} \quad (4.21)$$

and

$$K_b = \frac{1}{K(a,b,T)} \cdot \frac{dK(a,b,T)}{db} \quad (4.22)$$

where  $dK/da$  and  $dK/db$  can be obtained by differentiating (3.29) as

$$\frac{dK(a,b,T)}{da} = -G \cdot A_2 \cdot \lambda_o^2 \cdot \frac{b}{\epsilon^2(a,b)} \cdot \left( \frac{\Delta\lambda}{\lambda_o} \right)^2 \cdot (r_1 + L_1) \quad (4.23)$$

and

$$\frac{dK(a,b,T)}{db} = G \cdot A_2 \cdot \lambda_o^2 \cdot \frac{a}{\epsilon^2(a,b)} \cdot \left( \frac{\Delta\lambda}{\lambda_o} \right)^2 \cdot (r_1 + L_1) \quad (4.24)$$

Using the definitions of Equations (4.19) through (4.22) we can now obtain the expressions for the partial derivatives of the signal with respect to the coefficients  $a$  and  $b$  of the emissivity model

$$\frac{dS(a,b,T)}{da} = S(a,b,T) \cdot (\epsilon_a + K_a) \quad (4.25)$$

and

$$\frac{dS(a,b,T)}{db} = S(a,b,T) \cdot (\epsilon_b + K_b) \quad (4.26)$$

Having defined all the necessary partial derivatives of the signal model we are now ready to proceed with the numerical evaluation of the temperature accuracy achievable by the least-squares based M-WIP. In order to perform these computations we have to assume

some values of the coefficients  $a$  and  $b$  which would be realistic and representative of the practical situations. For the purpose of this analysis the data on the spectral emissivity of pure silicon published by Sato [23] and shown in Figure 4.1 has been used. The coefficients of the linear emissivity model were obtained by performing the least-squares fit of the first degree polynomial to the data given in this figure for the spectral emissivity of silicon at 1073K and the wavelength range from 1.5 to 5.0  $\mu\text{m}$ .

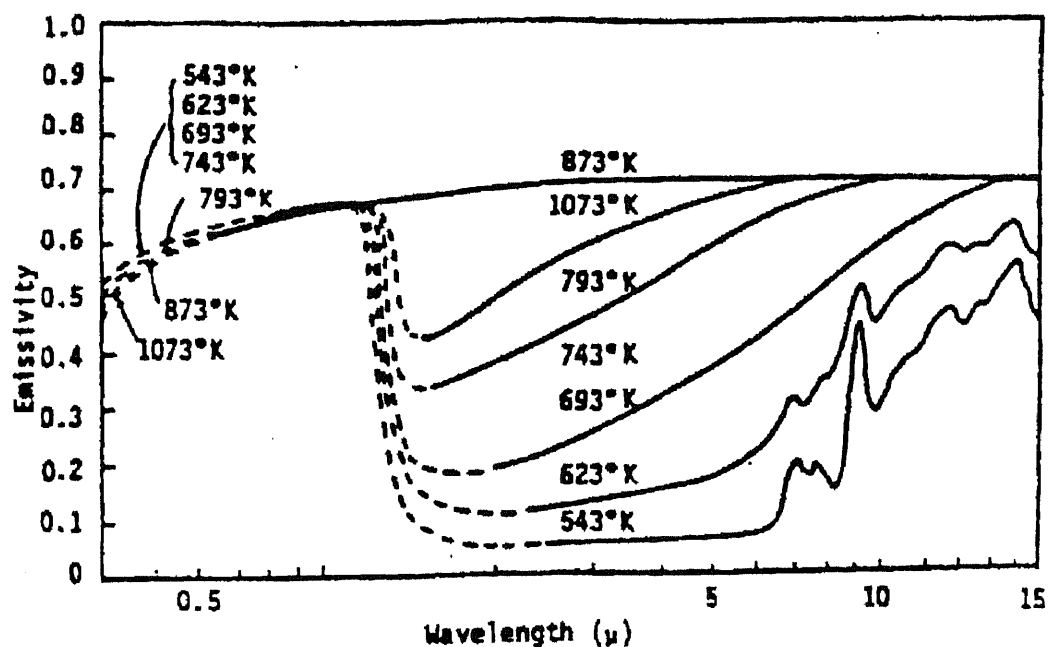


**Figure 4.1** Spectral emissivity of single crystal n-type silicon disc [23]

The coefficients of the nonlinear emissivity model were obtained by fitting the second degree polynomial to the spectral emissivity data corresponding to 793K for wavelength interval given above. The results of this fitting procedure show that the spectral emissivity of pure silicon at 1073K can be represented by a first degree polynomial as

$$\varepsilon_{1073\text{K}}(\lambda) = 0.6871 + 0.0086 \cdot \lambda \quad (4.27)$$

whereas for the specimen at 793 K the expression of the spectral emissivity requires second degree polynomial

$$\varepsilon_{793K}(\lambda) = 0.2253 + 0.1586 \cdot \lambda + 0.0148 \cdot \lambda^2 \quad (4.28)$$

We will now proceed with the performance analysis of the three M-WIP systems based on an array of PtSi Schottky-barrier detectors, InGaAs line array and, finally, on microbolometer Uncooled Focal Plane Array (UFPA). In order to utilize the methodology of this Chapter we will need the models of the spectral response for each of the above systems along with the model of noise fluctuations affecting their performance.

## **4.2 Performance of M-WIP Systems Based on PtSi Imagers with Schottky-Barrier IR Detectors (SBDs)**

### **4.2.1 320x244 IR CCD and 640x480 IR MOS Image Sensors**

The radiometric analysis presented in Section 4.1 will now be applied to the 320x244 IR CCD and 640x480 IR MOS image sensors (imagers) developed at the David Sarnoff Research Center. The IR detectors used in these imagers are the PtSi Schottky-barrier detectors (SBDs) which are most sensitive to the radiation emitted in the SWIR (1 to 3  $\mu\text{m}$ ) and MWIR (3 to 5  $\mu\text{m}$ ) bands.

The 320x244 IR CCD imager has 40- $\mu\text{m}$  x 40- $\mu\text{m}$  pixels and a fill factor of 43%. This imager employs buried-channel CCD (BCCD) readout registers and has the pixel layout shown in Figure 4.2 [28]. The BCCD readout registers of this imager provide maximum charge handling capacity of  $1.4 \times 10^6$  electrons per pixel.

The 640x480 IR MOS imager has 24- $\mu\text{m}$  x 24- $\mu\text{m}$  pixel size and fill factor of 38%. This imager has a low-noise X-Y addressable readout multiplexer with two MOS switches per SBD, and a MOS source follower at the output of each row with 8:1 multiplexing to a shared on-chip output amplifier. The readout noise of this device is under 300 rms

electrons per pixel [28]. The readout structure of this imager is shown in Figure 4.3. Its saturation charge level is  $1.5 \times 10^6$  electrons per pixel. It should also be noted that the Sarnoff 640x480 IR MOS imager can be operated with subframe imaging capability for any subframe size and location. In addition, this imager provides electronic integration time control down to a minimum of 60  $\mu\text{s}$  for operation at 30 frames per second.

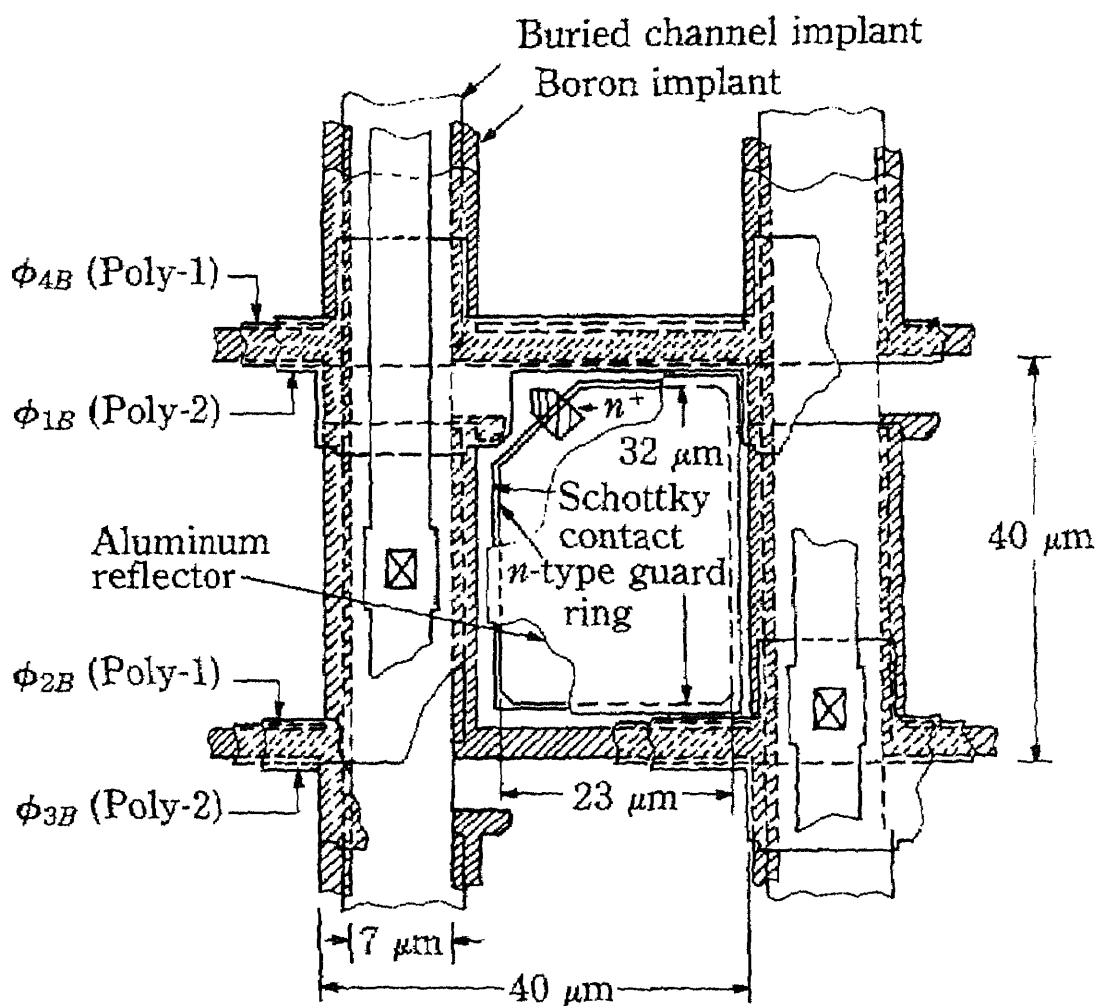
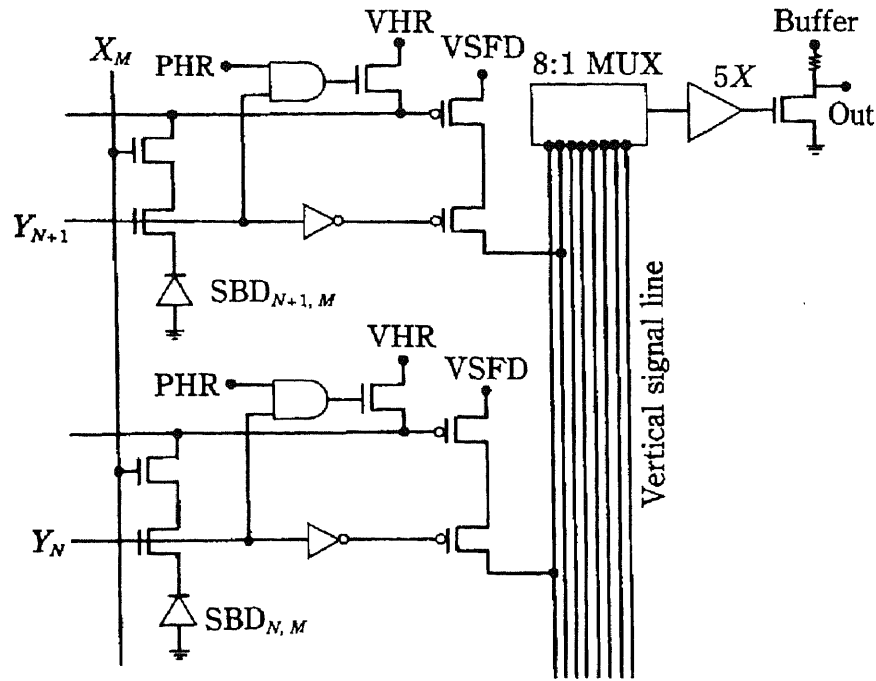


Figure 4.2 Pixel layout of Sarnoff 320x244 IR imager [28]



**Figure 4.3** Low-noise MOS readout MUX of Sarnoff 640x480 IR MOS imager [28]

#### 4.2.2 PtSi Schottky-Barrier Detector

Both IR imagers described in the previous section employ PtSi Schottky-barrier photon detectors. The basic construction and operation of PtSi SBD is illustrated in Figure 4.4.

The infrared radiation with photon energy less than the bandgap of silicon ( $E_g=1.12$  eV) is transmitted through the substrate. The absorption of the infrared radiation in the silicide layer results in the excitation of photocurrent across the Schottky-barrier ( $\Psi_{ms}$ ) by internal photoemission. The Schottky-barrier is the barrier that is formed between the silicide layer and the p-type silicon substrate. The absorbed IR photons excite the valence electrons above the Fermi level, generating hole-electron pairs. The holes with energy levels exceeding the Schottky-barrier are injected into the silicon substrate. The result of this process is the accumulation of negative charge on the silicon electrode. The detection of the optical signal is completed by transferring the negative charge from the silicide electrode into the readout structure.

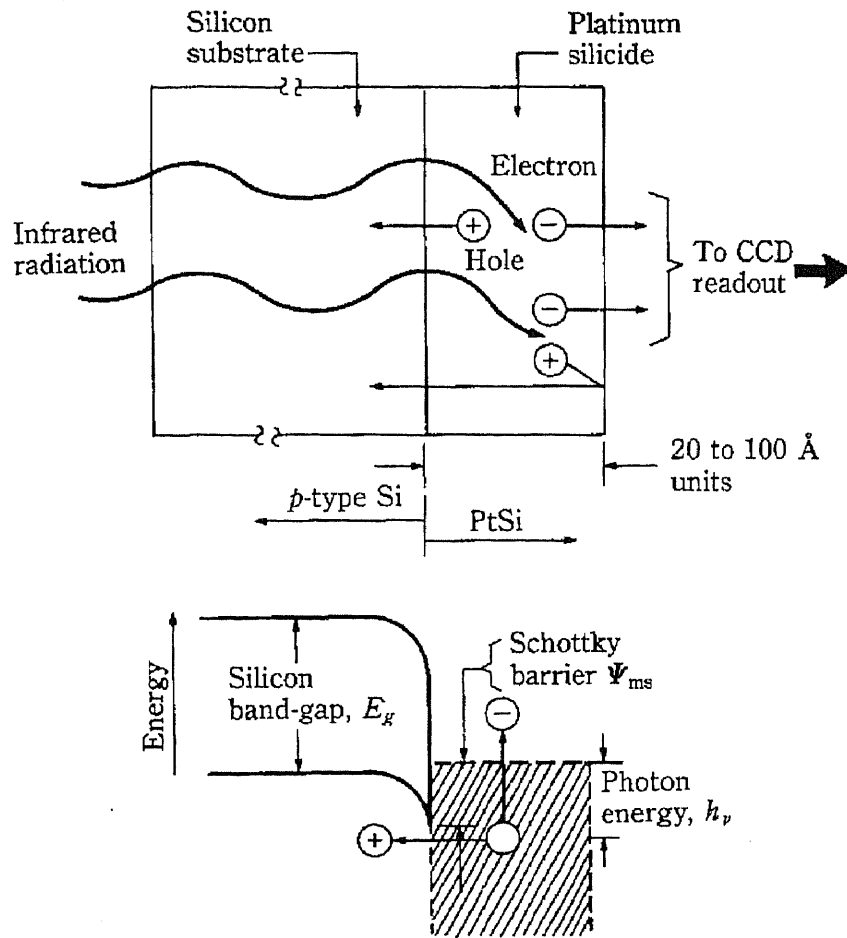


**Figure 4.4** Operation of Schottky-barrier detector [29]

The spectral responsivity  $R(\lambda)$  of the IR imager depends on the quantum efficiency of the PtSi Schottky-barrier detectors and can be approximated by the Fowler equation [28] as

$$R(\lambda) = C_1 \left( 1 - \frac{\Psi_{ms} \cdot \lambda}{1.24} \right)^2 \quad (4.29)$$

The spectral responsivity and quantum efficiency of the PtSi SBD array corresponding to  $C_1 = 0.124 \text{ eV}^{-1}$  and  $\Psi_{ms} = 0.2272 \text{ eV}$  is shown in Figure 4.5.

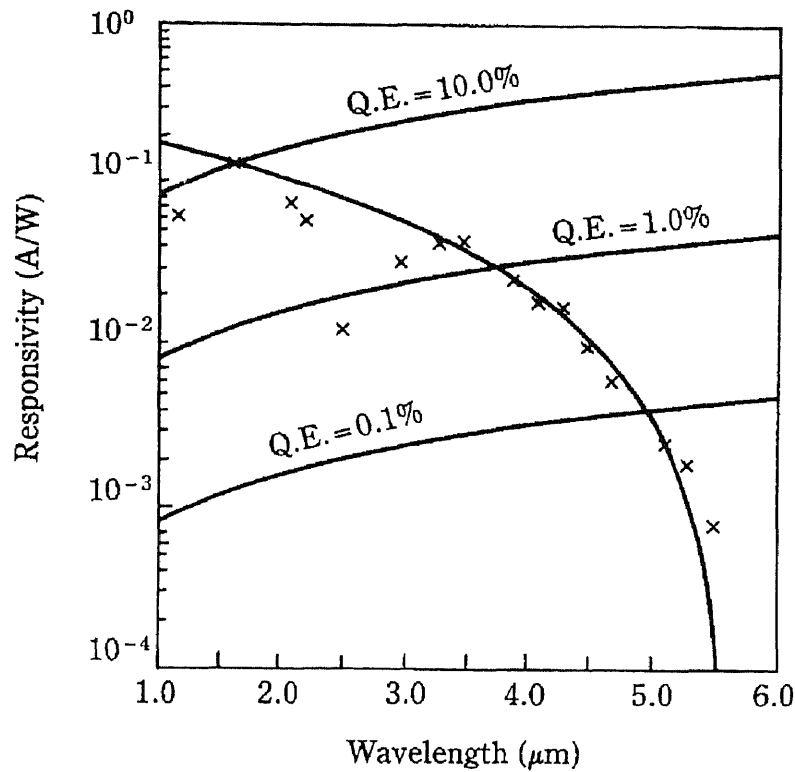


**Figure 4.5** Measured responsivity of PtSi Schottky-Barrier detector array [28]

#### 4.2.3 Accuracy of M-WIP Temperature Measurements based on IR FPA with PtSi Schottky-Barrier Detectors

At this point we can estimate the performance of the M-WIP system based on IR FPA with PtSi Schottky-barrier detectors by one of the two methods. The first method is based on the “computational experiment” whereas the detected signal is simulated using the signal model given by Equation (3.31) with the spectral emissivity model given by Equations (4.27) and (4.28). As part of these simulations we utilized a random number generator in order to simulate normally distributed noise in the signal with the rms value given by Equation (2.20). We then performed the least-squares fit of the imager model given by Equation (2.20) to the above simulated signal. The temperature accuracy (standard deviation of the parameter  $T$ ) was obtained by a comparison of the results of the least-squares fit with the “true” value of the signal used in the simulation experiments. The second method is based on the development given in Section 4.1 and involves direct computation of the standard

deviation from Equation (4.10). It should be noted, however, that this method is based on the first order approximation of the outcome of the least-squares fit and, as illustrated in Figure 4.6, leads to higher errors in the estimation of the temperature accuracy in comparison to what is achievable by MWIP.

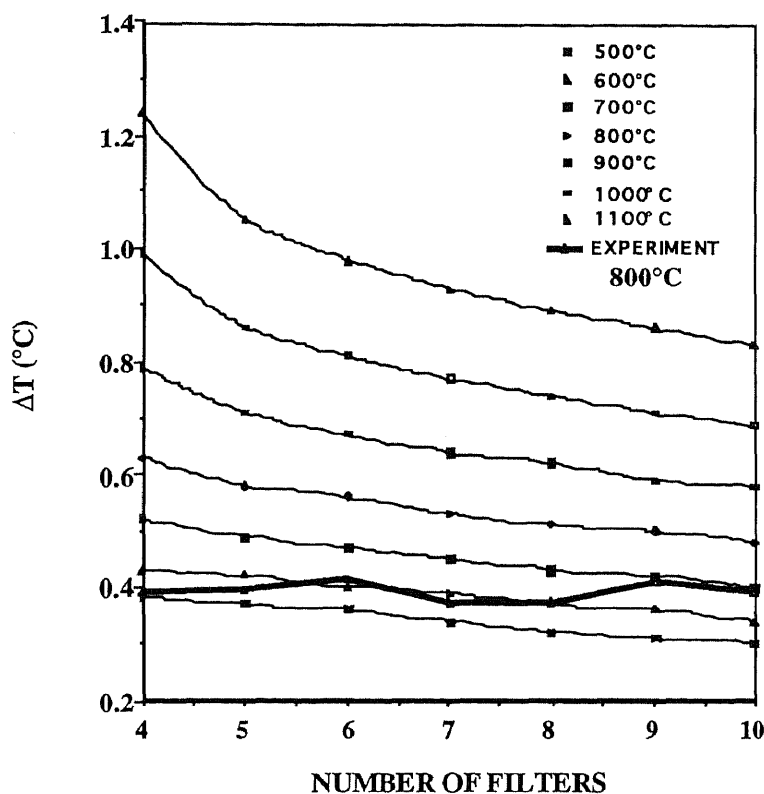


**Figure 4.6** Temperature accuracy of MWIP for linear emissivity model. The computations assume 100-nm-wide Gaussian filters and  $Q_{\max}=10^6$  electrons per pixel

### 4.3 Performance of M-WIP Systems Based on InGaAs Photodetector Array

Experimental and theoretical study of the performance of M-WIP systems based on InGaAs photodetector arrays was conducted under DARPA contract ARPA-93-DAAH01-93-C-R272 "Compact NIR Spectral Radiometer for CVD Non-Contact Temperature Measurements". Equipment and proprietary information of Sensors Unlimited, Inc., Princeton, NJ, were utilized in this study.



#### 4.3.1 Experimental M-WIP System

The prototype M-WIP system used in this study consisted of a Sensors Unlimited Model SU256L-1.7RT-250A linear InGaAs photodiode array mounted on Jarrell-Ash 0.27 meter Czerny-Turner Spectrograph and controlled with EG&G Model 1470A optical multichannel analyzer. Schematics of this prototype M-WIP system is shown in Figure 4.7.

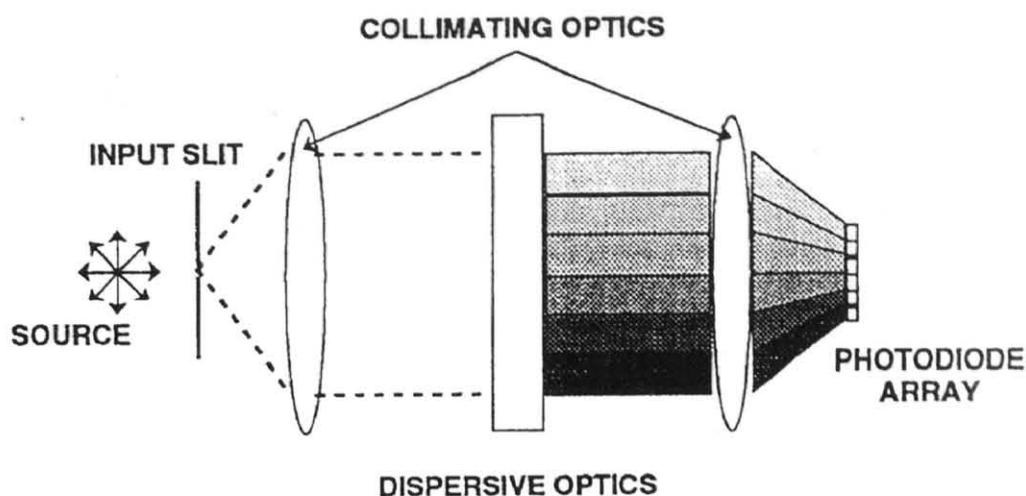


**Figure 4.7** Schematics of prototype M-WIP based on InGaAs photodetector array

In this system, target radiation enters the input slit where it is collected and collimated by a concave mirror with a focal length of 0.27 meters. The light is then dispersed into its spectral components by a ruled grating and subsequently focused onto the photodiode array by the second concave mirror. The utilization of the diffraction grating with 150 grooves/mm yields dispersion of 24nm/mm at the photodiode array. The system uses 0.25 mm - wide input slit and the photodetector array with 1.2 nm pixel pitch resulting in the effective instrument resolution of 6 nm. The photograph and layout schematics of 256-element Sensors Unlimited InGaAs photodiode array are shown in Figure 4.8 and Figure 4.9, respectively. This array was fabricated using  $\text{In}_{.53}\text{Ga}_{.47}\text{As}$  as the active material with a long wavelength cutoff of 1.7  $\mu\text{m}$ .

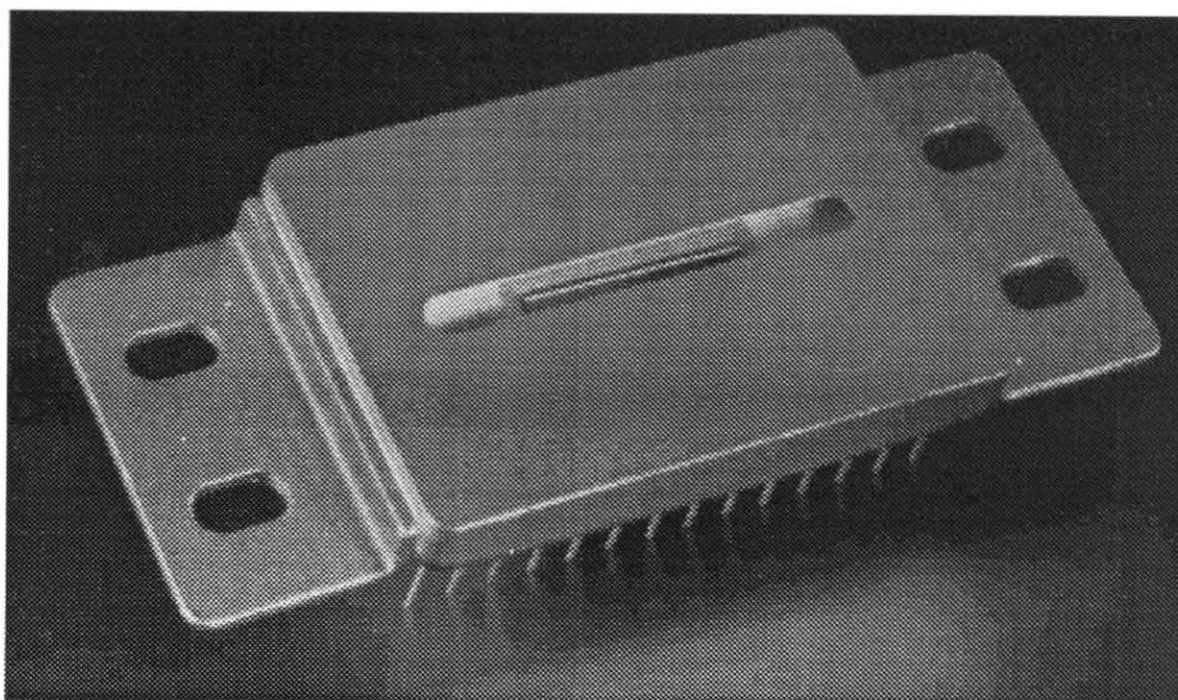


**Figure 4.8** Photograph of Sensors Unlimited SU256L-1.7RT-250A linear array

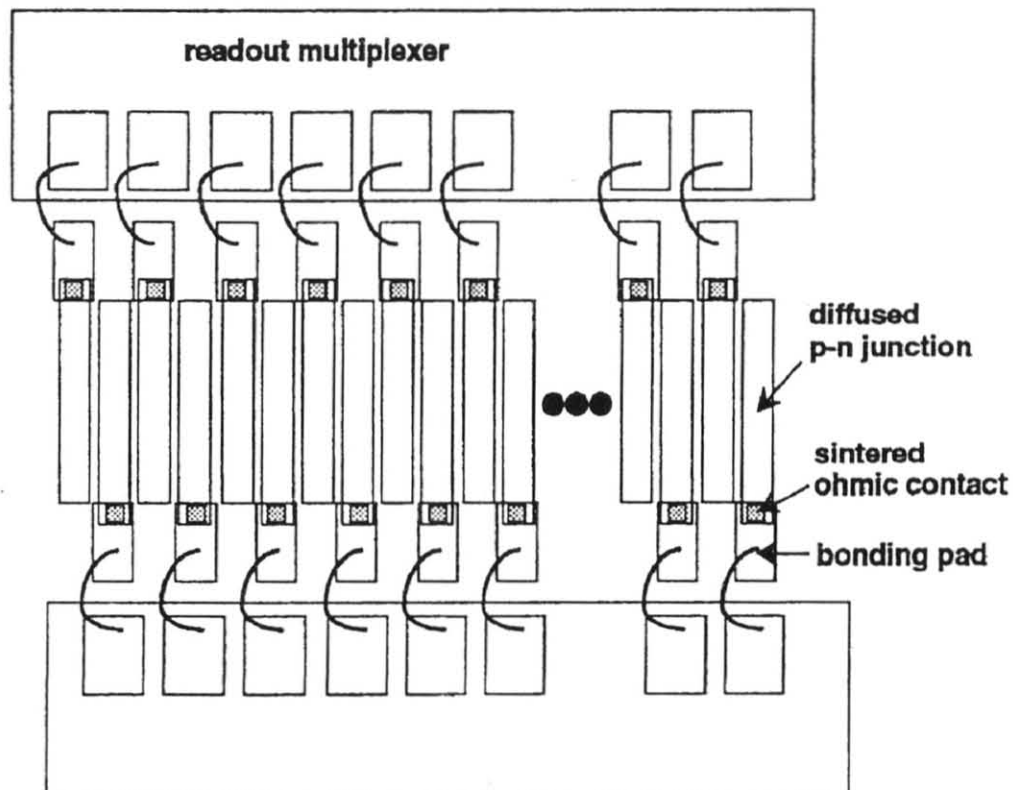


**Figure 4.9** Schematics of Sensors Unlimited SU256L-1.7RT-250A InGaAs array

### 4.3.2 Theoretical Performance Prediction

For the purpose of present analysis the experimentally measured responsivity,  $R(\lambda)$ , of InGaAs IR detectors was approximated by a polynomial function of wavelength as illustrated in Figure 4.10. The approximating polynomial is given by:

$$R(\lambda) = 41.891 - 122.2 \cdot \lambda + 141.8 \cdot \lambda^2 - 81.933 \cdot \lambda^3 + 23.743 \cdot \lambda^4 - 2.755 \cdot \lambda^5 \quad (4.30)$$

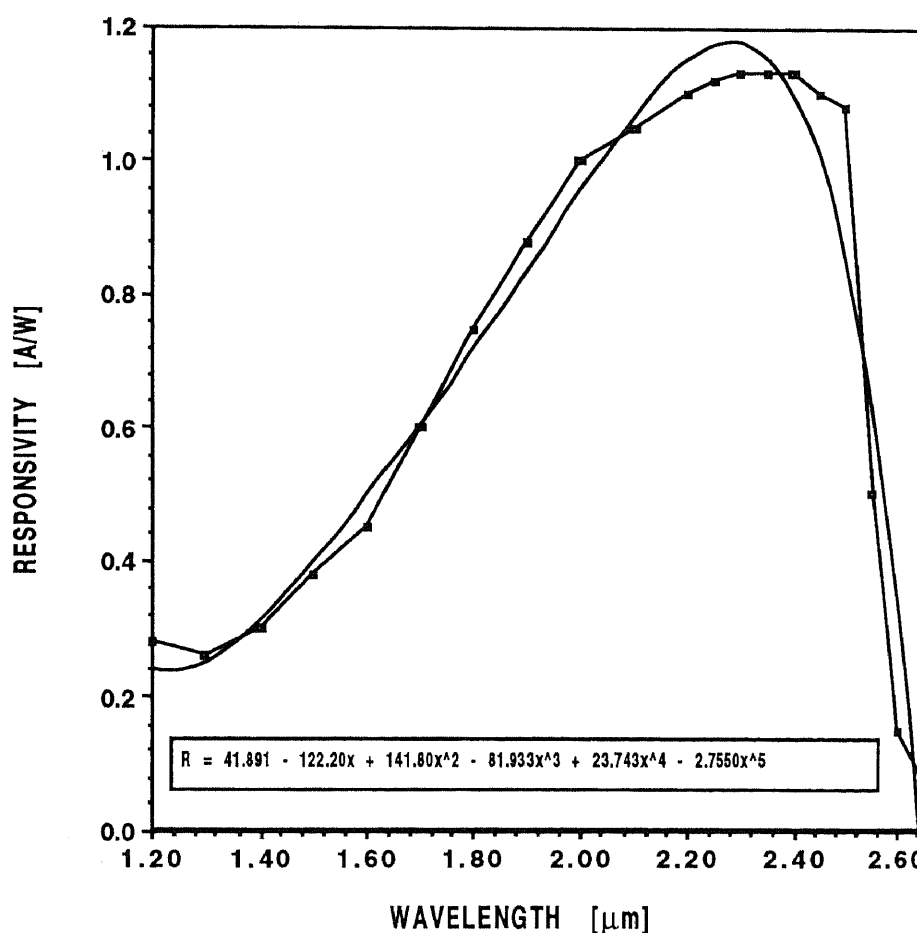


**Figure 4.10** InGaAs responsivity approximation

Figure 4.11 illustrates the theoretical values of the detected signal that were calculated for InGaAs line sensor illuminated by blackbody radiation and operated with 2ms optical integration time,  $f/10$  optics, and a variable IR filter with bandwidths equal to the 3% of

The accuracy of M-WIP temperature measurements was estimated from the actual least squares fits of the described above "noisy" signal to the "true" signal as described in Section 4.2.3. The results of these computations for the case of blackbody targets are illustrated in Figure 4.12. Inspection of this figure shows that the accuracy better than 0.5 K can be achieved for a wide range of temperatures in excess of 450K. Below this temperature the large portion of the emitted radiation does not correspond to the spectral bandwidths of the InGaAs IR detectors (1.3  $\mu\text{m}$  to 2.6 $\mu\text{m}$ ) and, therefore, high signal-to-noise ratio can not be achieved.

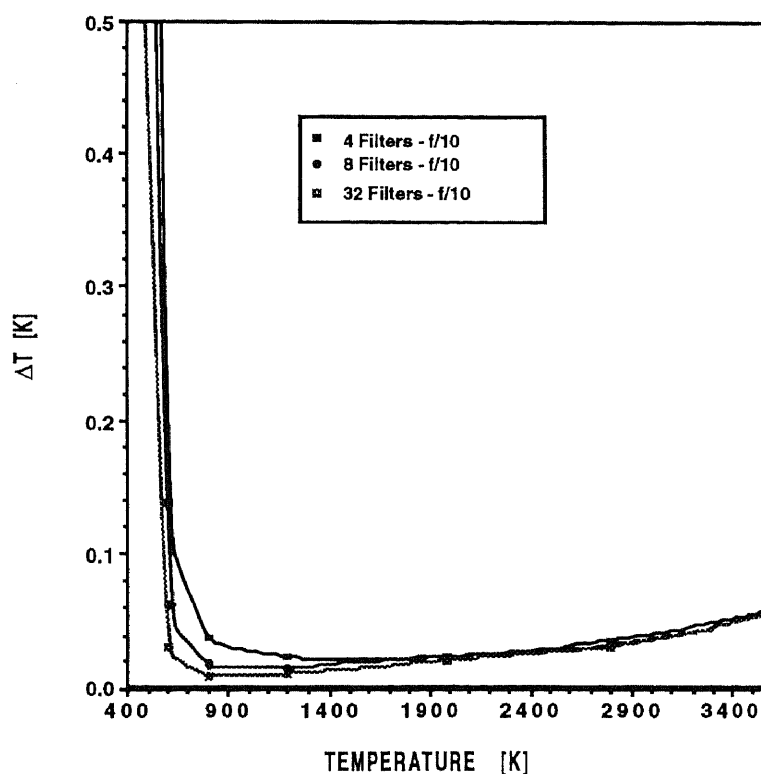


**Figure 4.12** M-WIP performance estimated for InGaAs sensor viewing blackbody target

The accuracy of M-WIP temperature measurements was also analyzed for the case of linear dependence of the target spectral emissivity on wavelength. The results of this analysis are illustrated in Figure 4.13. In this case, assuming no prior knowledge of the absolute values of spectral emissivity, accuracy of better than 1.0°C can be achieved by InGaAs IR sensor for targets temperatures in the range from 700K to 4500K.

The accuracy of M-WIP temperature measurements was estimated from the actual least squares fits of the described above "noisy" signal to the "true" signal as described in Section 4.2.3. The results of these computations for the case of blackbody targets are illustrated in Figure 4.12. Inspection of this figure shows that the accuracy better than 0.5 K can be achieved for a wide range of temperatures in excess of 450K. Below this temperature the large portion of the emitted radiation does not correspond to the spectral bandwidths of the InGaAs IR detectors (1.3  $\mu\text{m}$  to 2.6 $\mu\text{m}$ ) and, therefore, high signal-to-noise ratio can not be achieved.

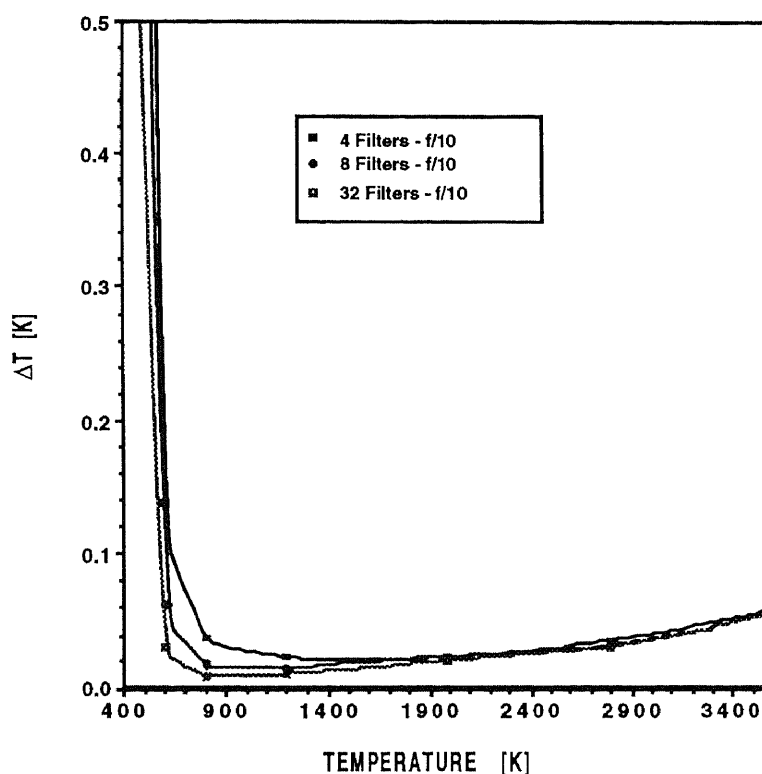


**Figure 4.12** M-WIP performance estimated for InGaAs sensor viewing blackbody target

The accuracy of M-WIP temperature measurements was also analyzed for the case of linear dependence of the target spectral emissivity on wavelength. The results of this analysis are illustrated in Figure 4.13. In this case, assuming no prior knowledge of the absolute values of spectral emissivity, accuracy of better than 1.0°C can be achieved by InGaAs IR sensor for targets temperatures in the range from 700K to 4500K.

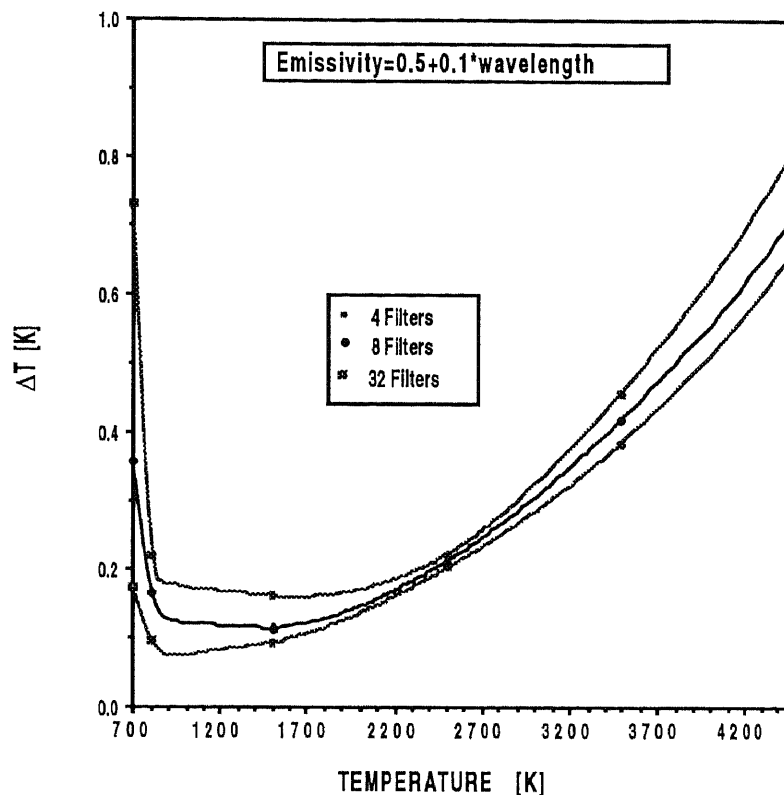


**Figure 4.13** M-WIP performance estimated for InGaAs sensor viewing linear radiator

It may be noted, that the very high estimated accuracy of the M-WIP illustrated in Figure 4.12 and Figure 4.13 is due to the fact that only temporal noise sources were taken into account. It can be concluded from the present analysis that in the case of IR sensor with maximum charge handling capacity of  $5 \times 10^8$  electrons/detector the readout, radiation and dark current noise sources do not significantly limit the accuracy of M-WIP temperature measurements.

However, it should be pointed out that high signal-to-noise ratio of the M-WIP measurements does not guarantee the accuracy of temperature estimation. Among factors that can significantly limit the accuracy of M-WIP is the non-linearity of detector response due to signal-level-dependent variation in the readout capacitance. Another factor strongly affecting the accuracy of M-WIP measurements is the insufficient knowledge of the spectral characteristics of the M-WIP system itself.

For the purpose of analyzing the effect of detector response non-linearity on the accuracy of M-WIP measurements, the "non-linear" signal was simulated using the linear-response model and parabolic function tangent to the linear model at zero signal level and deviating from the linear model by a given percentage at the prespecified signal level. For the purpose of present analysis, the non-linearity was expressed in terms of signal level differences between linear and non-linear signal at 80% of the maximum charge handling capacity. In this case the correction between linear and non-linear signals is given by:

$$\Delta S = S_{\text{linear}} - S_{\text{non-linear}} = \frac{S_{\text{linear}}^2}{0.8Q_{\text{max}}} n \quad (4.31)$$

where  $n$  - is the fraction of non-linearity at 80% of  $Q_{\text{max}}$ .

The simulated M-WIP performance as a function of the detector response non-linearity is shown in Figure 4.14.

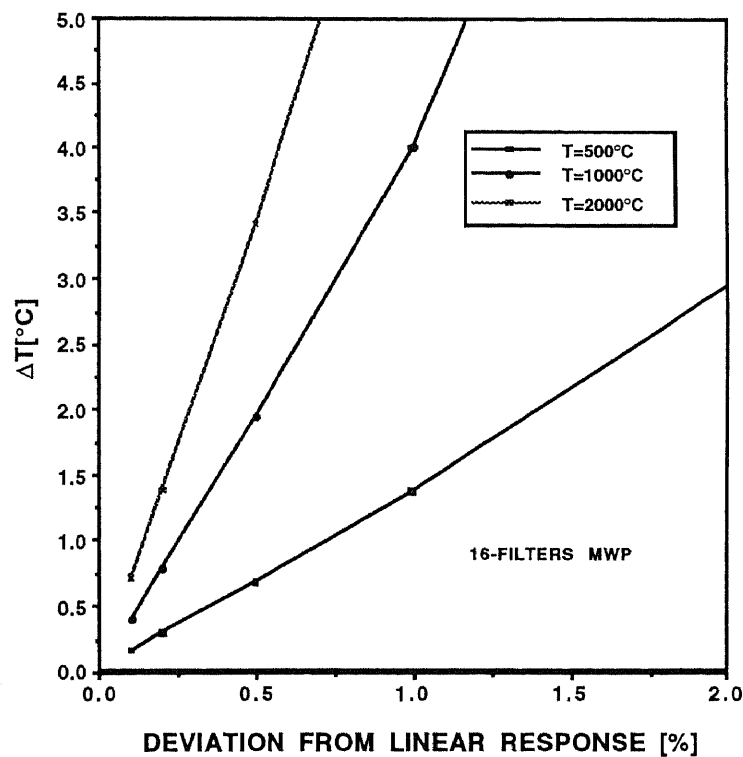


**Figure 4.14** Effect of detector response non-linearity on M-WIP performance

Inspection of Figure 4.14 shows that temperature resolution of better than 1°C can only be achieved with an extremely linear IR detectors, with response non-linearity of less than 1%.

In order to evaluate the effect of uncertainty in the spectral characteristics of the system on the accuracy of M-WIP temperature estimation we can utilize approach described in Section 4.1. For the purpose of this analysis we extend our definition of the rms noise in the detected signal,  $\sigma_i^2$ , to include the effect of uncertainty in our knowledge of the spectral wavelengths of M-WIP channels,  $\sigma_{\lambda_i}$ , as:

$$\sigma_i^2 = \sigma_{S_i}^2 + \left( \sigma_{\lambda_i}^2 \frac{\partial S(\lambda, T)}{\partial \lambda_i} \right)^2 \quad (4.32)$$

where  $S(\lambda, T)$  is the detected signal (electrons/pixel) and  $\sigma_{S_i}$  is the temporal (radiation and readout) noise (electrons/pixel).

Using the extended definition of rms signal noise as given by Equation (4.32) we can now utilize Equation (4.10) to estimate the effect of uncertainty in our knowledge of central wavelengths of M-WIP channels on InGaAs M-WIP performance. The results of these computations are shown in Figure 4.15.

Inspection of Figure 4.15 shows that increase in the number of filters used for M-WIP beyond 16 does not lead to substantial improvement in the accuracy of the temperature measurements.

Figure 4.15 also illustrates high sensitivity of the measurement results to the precise knowledge of spectral characteristics of M-WIP system. Therefore, it should be stressed that prior to actual M-WIP measurements, the spectral characteristics of the entire MWP system should be calibrated against reference radiation source with known spectral emittance (usually blackbody). Furthermore, the precision of the calibration source itself should be given special consideration, as it will affect the actual accuracy of the M-WIP temperature measurements.



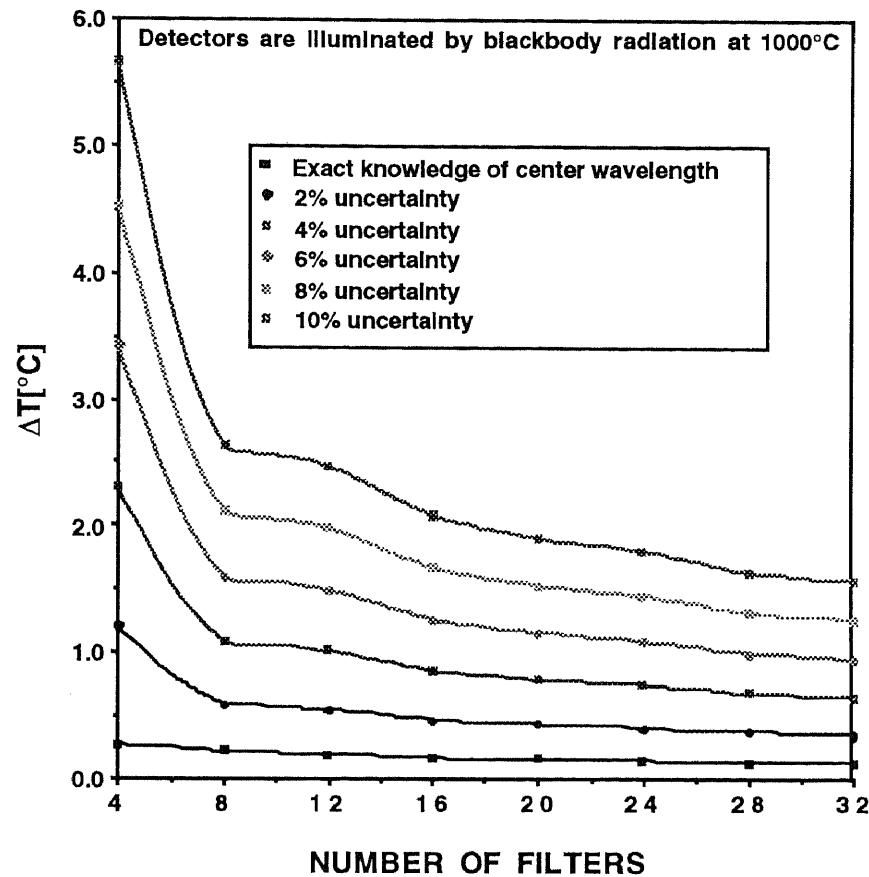


**Figure 4.15** InGaAs M-WIP performance vs. uncertainty in filter wavelengths

#### 4.3.3 Experimental Evaluation of InGaAs M-WIP Performance

The experimental system described in Section 4.3.1 was utilized to demonstrate the performance of InGaAs-based M-WIP. For the purpose of this experiment, 256-element InGaAs line sensor was positioned at the output slit of the commercial spectrometer characterized by spectral dispersion corresponding to 1.2nm per pixel and spectral resolution of approximately 6nm (5 pixels). The input slit of the spectrometer was illuminated by blackbody radiation from Infrared Industries Blackbody Source. In order to maximize the accuracy of the M-WIP measurements, the blackbody radiation was sampled at two slightly overlapping spectral intervals from 1000nm to 1450nm and from 1400nm to 1750nm, thus covering the entire range of NIR sensitivity of InGaAs detectors. In the course of the experiment the response of IR detectors corresponding to various

temperatures of the blackbody source in the range from 600°C to 800°C was recorded for a number of optical integration times from 30ms to 240ms.

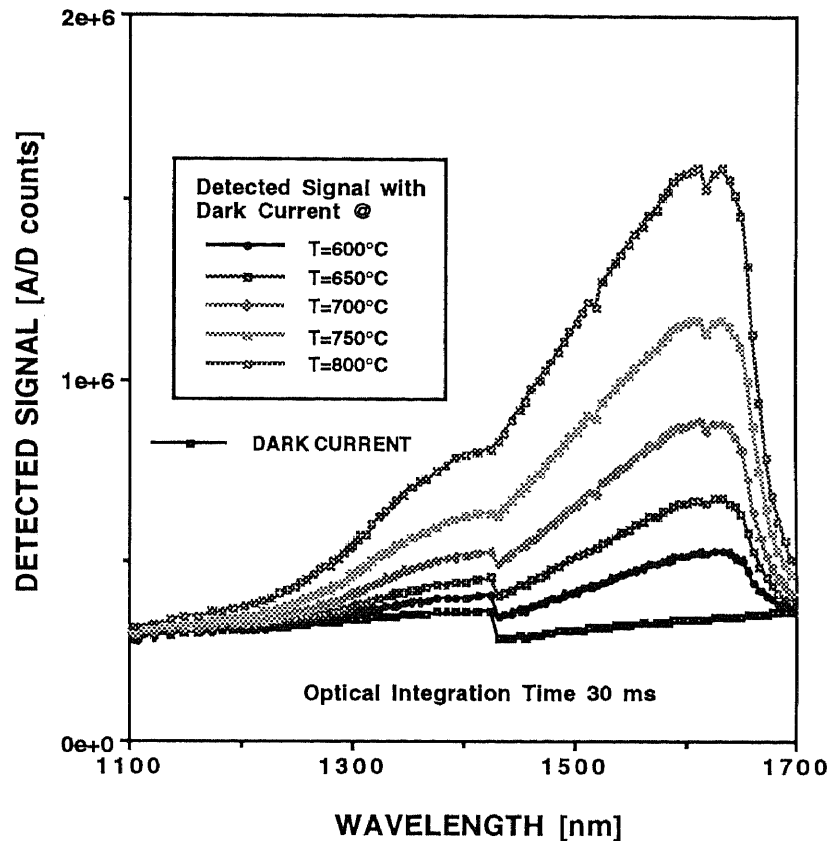


**Figure 4.16** Experimental measurements of blackbody radiance and dark current obtained with Sensors Unlimited InGaAs detector array

The "bad" pixels (#1-6,26,122,182,183,184) corresponding to the spectral peculiarities in the detected signal were eliminated from the analysis. The remaining 245 pixels were grouped in 49 groups of 5 pixels each with the values of the detected signal averaged over all detectors within the group. Next, each of the 49 detector groups was assigned two values of center wavelengths corresponding to the two spectral regions used in the experiment. The actual values of center wavelengths of each detector were determined based on the calibration of spectrometer against emission lines of krypton. The above experimental procedure resulted in 98 distinct spectral measurements obtained for

each temperature of the blackbody source and each value of the optical integration time. These experimental measurements obtained with 30 ms optical integration time are illustrated in Figure 4.16 along with corresponding "closed-aperture" dark current measurements.

Due to variation of the detector dark current with the bias voltage, the rate of the generation of the dark current charge depends on the magnitude of the accumulated signal. In order to estimate this effect "closed aperture" measurements were also performed with optical integration times in the range from 30ms to 1s. Based on this data the values of the dark current charge corresponding to various intensities of the incident radiative flux were estimated in accordance with algorithm described in Section 6.1.1. The results of these computations are illustrated in Figure 4.17 for pixel group with center wavelength of 1600 nm and temperatures of the blackbody source in the range from 600°C to 800°C.

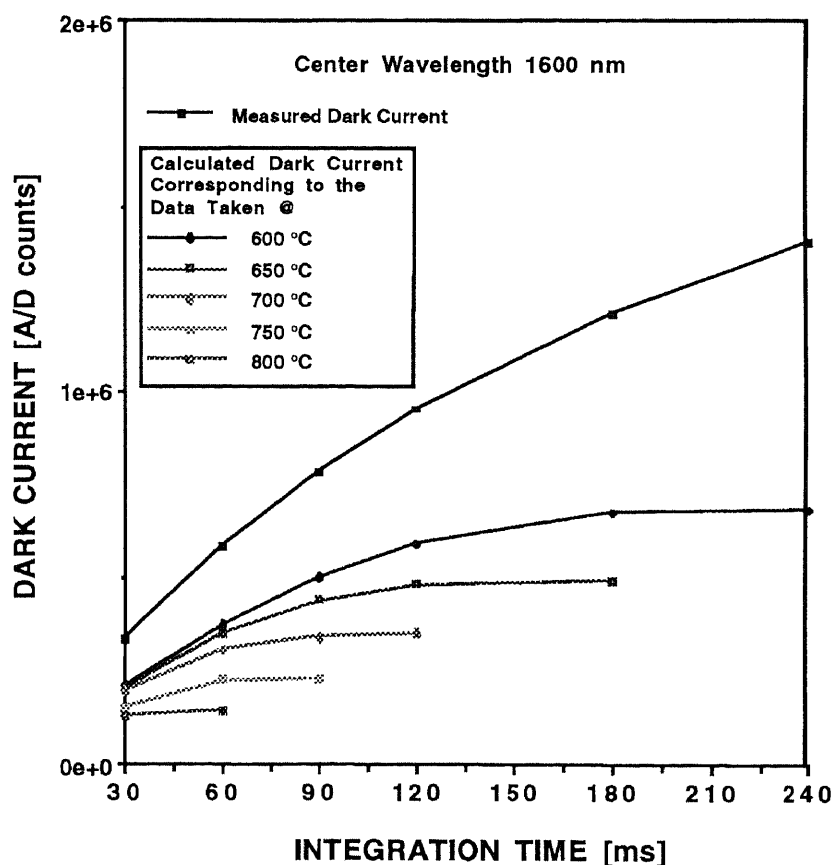
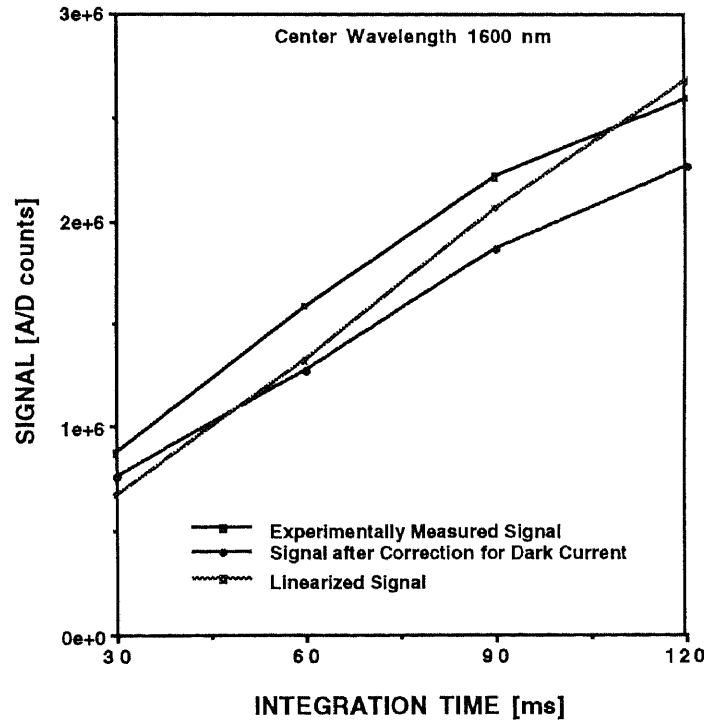


Figure 4.17 Measured and estimated dark current for Sensors Unlimited InGaAs array

Due to the variation in depletion-layer capacitance of the photodiode with change in bias voltage, the detector response retains some non-linearity even after correction for dark current charge. In order to compensate for this signal-level-dependent non-linearity the corrected for dark current signal was approximated by the second degree polynomial of the optical integration time. For the purpose of this analysis it was assumed that the signal non-linearity is negligibly small at low signal levels. Based on this assumption the non-linearity correction,  $\Delta S$ , was computed as the difference between parabolic approximation of the signal and the line tangent to it at the lowest integration time used in the experiment,  $t_0=30\text{ms}$ . Expressing the non-linearity correction,  $\Delta S$ , as function of detected signal level we obtain:

$$\Delta S^i(\tilde{S}) = S_{\text{linear}}^i - \tilde{S}^i = \left( \sqrt{(p_2^i)^2 - 4p_3^i(p_1^i - \tilde{S}^i)} - p_2^i \right) \left( t_0 + \frac{p_2^i}{2p_3^i} \right) + p_1^i - p_3^i t_0^2 - \tilde{S}^i \quad (4.33)$$

where  $S_{\text{linear}}$  is the linearized signal,  $\tilde{S} = p_1 + p_2 t_{\text{int}} + p_3 t_{\text{int}}^2$  is the detected signal corrected for the dark current charge.



**Figure 4.18** Corrections for inherent non-linearity of InGaAs detector response

Figure 4.18 illustrates originally detected signal, signal corrected for dark current charge, and linearized signal for the detector group with central wavelength of 1600 nm.

The linearized signal measurements were used for calibration of spectral characteristics of InGaAs sensor. This calibration was based on the least-squares fit of theoretical model of the sensor response to the linearized values of signal detected by line sensor viewing blackbody source at various temperatures. This method of sensor calibration is further described in Section 6.2.1. Figure 4.19 illustrates the effective spectral responsivity of the InGaAs line sensor obtained as the result of the calibration procedure.

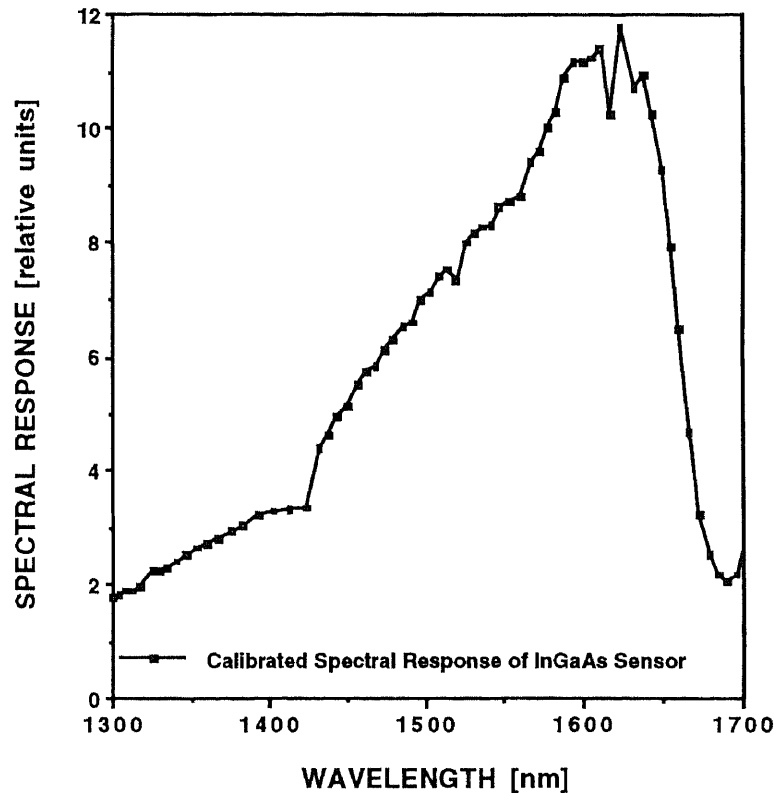


**Figure 4.19** Calibrated response of Sensors Unlimited InGaAs line sensor array

In order to demonstrate the accuracy of temperature measurements based on InGaAs M-WIP, the least-squares fit given by Equation (3.1) were performed on the corrected experimental data. Comparing the results of these fits to the "true" values of the blackbody

temperature used in experiment we can obtain the actual errors of the M-WIP temperature measurements. The magnitude of the resulting temperature error,  $\Delta T$ , does not exceed  $4^{\circ}\text{C}$  within the temperature range from  $600^{\circ}\text{C}$  to  $800^{\circ}\text{C}$  as illustrated in Figure 4.20. It should be noted, however, that this value of  $\Delta T$  is comparable to the accuracy of the calibration ( $\pm 3^{\circ}\text{C}$ ) of the blackbody source used in experiment.

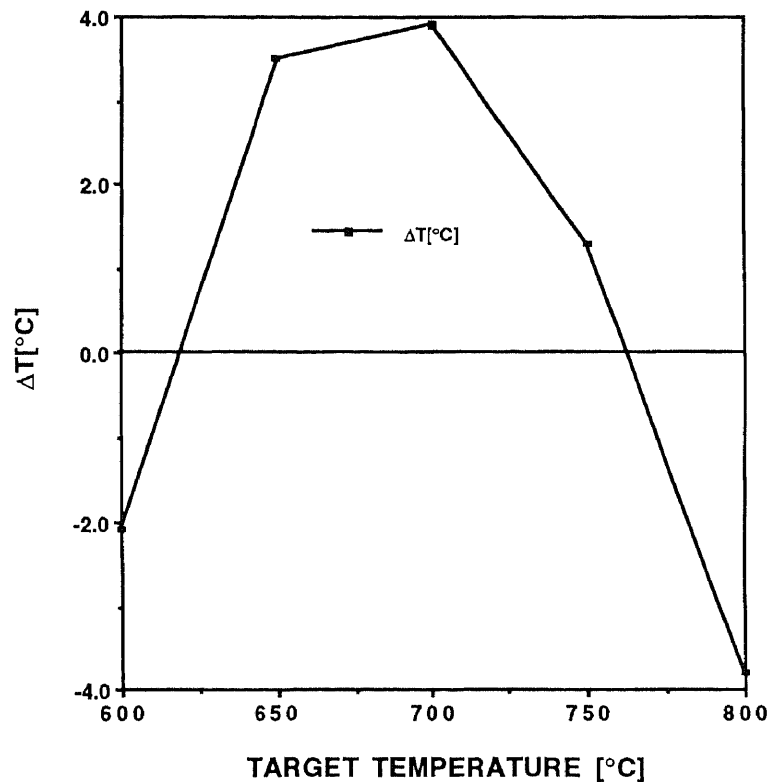


**Figure 4.20** Demonstrated accuracy of M-WIP temperature measurements with Sensors Unlimited InGaAs linear photodetector array

#### 4.4 Performance of M-WIP System based on Uncooled Microbolometer Focal Plane Array

##### 4.4.1 Design and Operational Principle of Microbolometer UFPA

Uncooled microbolometer arrays represent a new capability in staring imager development. Uncooled imager sensitivity demonstrated by Honeywell [30] is now better than  $0.05^{\circ}\text{C}$ ,

surpassing the sensitivity of some cooled scanned systems. The microscope photograph of Honeywell microbolometer array is illustrated in Figure 4.21.

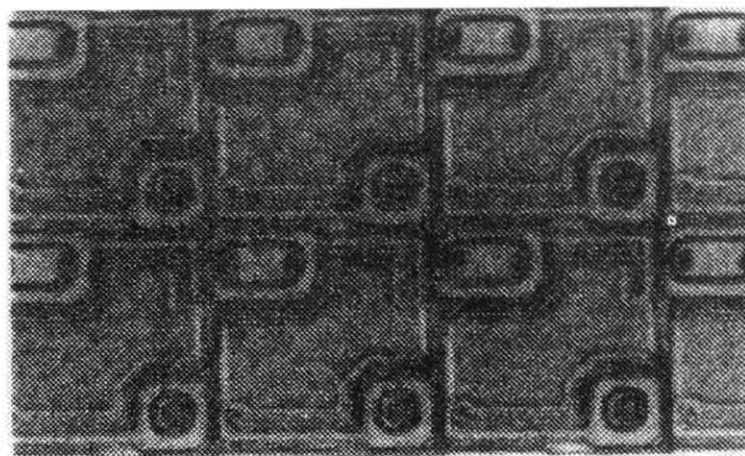


**Figure 4.21** Microscope photograph of Honeywell microbolometer array [30]

Honeywell's microbolometer pixel consists of a  $0.5\text{-}\mu\text{m}$ -thick plate suspended clear of the underlying silicon by two legs as illustrated in Figure 4.22. The legs provide the required high thermal resistance between the suspended plate and its surroundings, allowing the plate to respond to incident IR radiation by being heated or cooled. The temperature changes in the suspended plate cause changes in the electrical resistance, which are sensed by circuitry that is integrated into the underlying silicon and connected to the suspended plate by thin-film metallization on the legs.

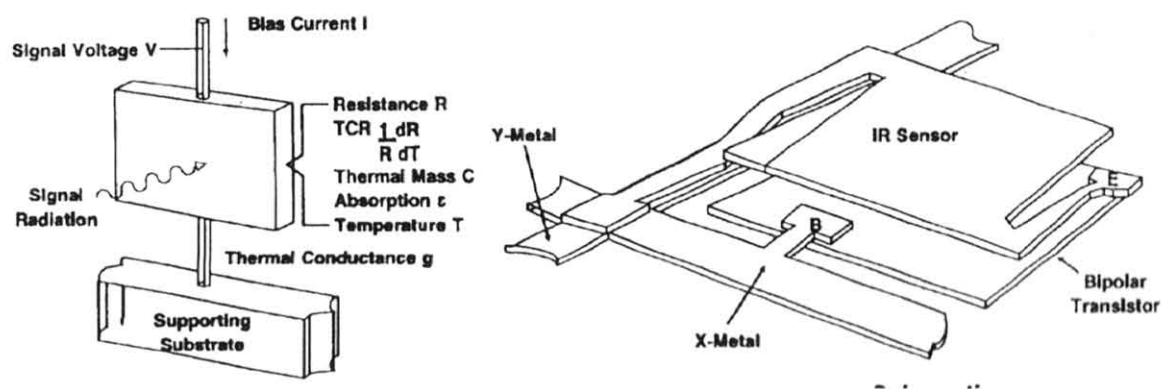


**Figure 4.22** Schematics and operational principle of microbolometer [31]

#### 4.4.2 Responsivity of Microbolometer Detectors

In order to derive the expression for the responsivity of microbolometer pixel we shall consider the heat-balance equation relating the temperature of the detector,  $T_d$ , to the incident target radiation,  $\Phi_{in}$ :

$$C \cdot \frac{dT_d}{dt} + G_{th} \cdot (T_d - T_0) = \varepsilon \cdot \Phi_{in} \quad (4.34)$$

where  $\varepsilon$  is the detector absorptivity illustrated in Figure 4.23;  $C$  is the heat capacity of the bolometer (J/K);  $G_{th}$  is the effective thermal conductance to the bolometer surroundings, including both radiation and conduction (W/K);  $T_0$  is the ambient temperature (K).

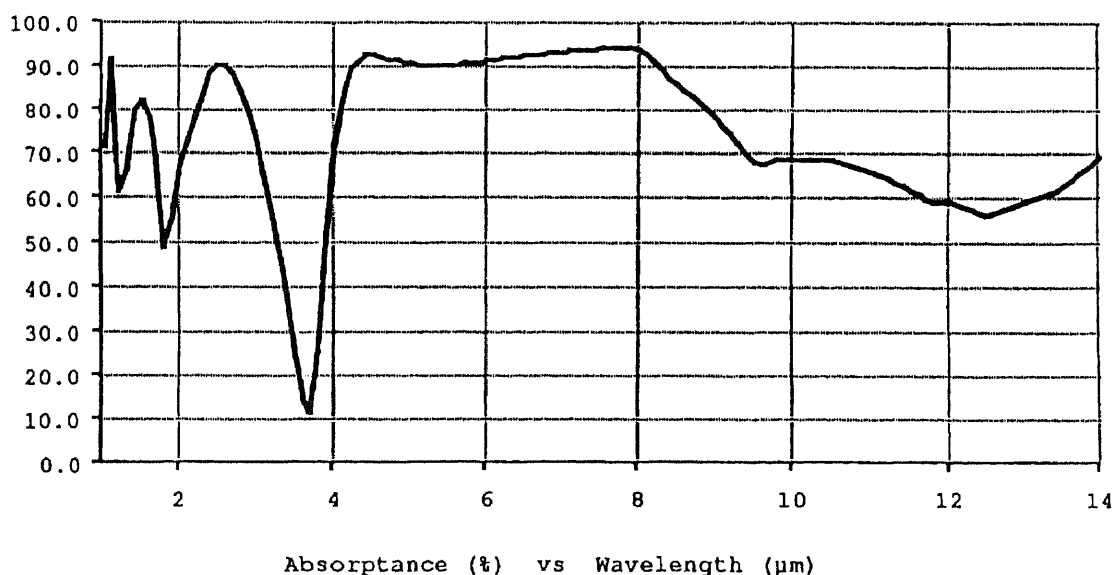


**Figure 4.23** Absorptance of Honeywell microbolometer detector [Honeywell, Inc.]

In many practical situations the incident target radiation is modulated by the chopper and can be expressed as:

$$\Phi_{in} = \Phi_{in}^0 \cdot e^{j\omega t} \quad (4.35)$$

where  $\omega$  is the modulation frequency of the incident radiation;



For small incremental change in the detector temperature,  $\Delta T_d$ , due to change in the incident radiation,  $\Delta \Phi_{in}$ , the Equation (4.34) can be re-written as:

$$C \cdot \frac{d\Delta T_d}{dt} + G_{th} \cdot \Delta T_d = \varepsilon \cdot \Delta \Phi_{in}^0 \cdot e^{j\omega t} \quad (4.36)$$

where  $\Delta T_d = T_d - T_0$ ;

Solving Equation (4.36) for  $\Delta T_d$  we obtain:

$$|\Delta T_d| = \frac{\varepsilon \cdot \Delta \Phi_{in}^0}{G_{th}(1 + \omega^2 \tau^2)^{1/2}} \quad (4.37)$$

where  $\tau = C/G_{th}$  is the thermal time constant;

The change in the electrical resistance of the bolometer element,  $dR_d$ , resulting from change in the bolometer temperature,  $dT_d$ , can be expressed in terms of so-called temperature coefficient of resistance (TCR),  $\alpha$ , as:

$$\alpha \cdot R_d = \frac{dR_d}{dT_d} \quad (4.38)$$

Therefore, small change in the detector temperature,  $\Delta T_d$ , results in the voltage change across the detector as given by:

$$\Delta V_d = I \cdot \Delta R_d \approx \alpha I R_d \Delta T_d = \frac{\varepsilon \Phi_{in}^0 I R_d \alpha}{G_{th}(1 + \omega^2 \tau^2)^{1/2}} \quad (4.39)$$

where  $I$  is the readout current;

Taking the ratio of the voltage change across the detector to the change in the incident target radiation we obtain the expression for the responsivity of the bolometer,  $R$ :

$$R = \frac{\varepsilon I R_d \alpha}{G_{th}(1 + \omega^2 \tau^2)^{1/2}} \quad (4.40)$$

#### 4.4.3 Noise Sources Affecting Bolometer Operation

In order to predict the performance of the microbolometer-based M-WIP system the noise sources affecting the bolometer signal must be analyzed. Study of the radiometric literature suggests that so-called Johnson noise and temperature fluctuation noise have the most significant effect on the total noise in the bolometer output signal [15,32].

**Johnson noise.** Johnson noise represents the voltage fluctuation across the resisting element due to Brownian motion of the charge carriers. Local random thermal motion of carriers sets up fluctuating charge gradients, even though an overall charge neutrality exists across the detector. The Johnson noise voltage is given by [32]:

$$V_{\text{Johnson}} = \sqrt{4kT_d R_d \Delta f} \quad (4.41)$$

where  $k$  is the Boltzmann's constant and  $\Delta f$  is the frequency bandwidth of the detector.

**Temperature Fluctuation Noise.** The temperature and energy of the bolometer are subject to random fluctuations due to a random nature of heat exchange (conduction and radiation) processes. In particular, randomness of multiple photon emissions leads to fluctuations in the power of radiative heat fluxes. Likewise, the Brownian motion of the electrons in the conductors leads to the random fluctuations in the conductive power flow. The fluctuations in the thermal energy of the bolometer element,  $\Delta E_d$ , and fluctuations of its temperature,  $\Delta T_d$ , are connected by the equation:

$$\Delta E_d = C \cdot \Delta T_d \quad (4.42)$$

On the other hand, it is well known from statistical mechanics that mean square energy fluctuations of any system with multiple degrees of freedom are given by [15]:

$$\overline{\Delta E^2} = kT^2 C \quad (4.43)$$

Combining Equations (4.42) and (4.43) we obtain the expression for the mean square temperature fluctuation of the bolometer,  $\overline{\Delta T_d^2}$ :

$$\overline{\Delta T_d^2} = \frac{kT_d^2}{C} \quad (4.44)$$

The heat flux fluctuations due to multiple random photon emissions and Brownian motion of the electrons can be closely approximated by the white noise, since the above elementary events are independent of each other. Therefore, the mean square heat flux fluctuations,  $\overline{\Phi^2}$ , can be represented as:

$$\overline{\Phi^2} = B \cdot \Delta f \quad (4.45)$$

where B is a positive constant.

Similarly to Equation (4.37), the detector temperature fluctuations,  $\overline{T^2}$ , can be related to power fluctuations,  $\overline{\Phi^2}$ , as:

$$\overline{T^2} = \frac{\overline{\Phi^2}}{G_{th}^2 (1 + (2\pi f\tau)^2)} \quad (4.46)$$

where f is the frequency modulation of the incident radiation.

To obtain the total mean square temperature fluctuation of the bolometer,  $\overline{\Delta T_d^2}$ , we substitute Equation (4.45) into Equation (4.46) and integrate over all frequencies:

$$\overline{\Delta T_d^2} = \int_0^\infty \overline{T^2} df = \int_0^\infty \frac{B \cdot df}{G_{th}^2 (1 + (2\pi f\tau)^2)} = \frac{B}{4G_{th}^2 \cdot \tau} \quad (4.47)$$

Combining Equations (4.44) through (4.47) we obtain:

$$\overline{T^2} = \frac{4kT_d^2 \Delta f}{G_{th} (1 + (2\pi f\tau)^2)} \quad (4.48)$$

Substitution of Equation (4.48) into Equation (4.46) yields mean square value of the fluctuation of the power flow into bolometer:

$$\overline{\Phi^2} = 4kT_d^2 G_{th} \Delta f \quad (4.49)$$

We now turn our attention to the nature of the energy exchange between bolometer element and its surroundings. As was already mentioned, the bolometer absorbs target and background thermal radiation as well as emits thermal radiation itself. In addition, there is conductive energy flow through the bolometer support and readout structure. Therefore, the generalized thermal conductance coefficient,  $G_{th}$ , can be represented as:

$$G_{th} = \frac{d\Phi}{dT} = \frac{d\Phi_{rad}^{target}}{dT} + \frac{d\Phi_{rad}^{bckg}}{dT} + \frac{d\Phi_{cond}}{dT} = G_{rad}^{target} + G_{rad}^{bckg} + G_{cond} \quad (4.50)$$

For a microbolometer-based M-WIP system the target radiation incident on the bolometer surface is filtered through narrow-band interference filter with effective bandwidth  $\Delta\lambda$  and transmission  $\tau(\lambda)$ . Taking into account the detector field of view defined by the  $f/\#$  of the optics and the area  $A_d$ , of the detector we obtain:

$$\begin{aligned} G_{rad}^{target} &= \frac{\epsilon_d \epsilon_{target} \pi A_d}{4(f/\#)^2} \cdot \frac{d(L_{\lambda,b}(\lambda, T_{target}))}{dT_{target}} \cdot \tau(\lambda) \cdot \Delta\lambda = \\ &= \frac{\epsilon_d \epsilon_{target} \pi A_d}{4(f/\#)^2} \cdot \frac{C_1 C_2}{\lambda^6 T_{target}^2} \frac{e^{C_2/\lambda T_{target}}}{(e^{C_2/\lambda T_{target}} - 1)^2} \cdot \tau(\lambda) \cdot \Delta\lambda \end{aligned} \quad (4.51)$$

where  $\epsilon_d$  and  $\epsilon_{target}$  are the emissivities of the detector and target, respectively.

The radiation exchange between the bolometer at temperature  $T_d$  and its surroundings at temperature  $T_0$  can be obtained from the Stephan-Boltzmann law described in Chapter 2:

$$G_{rad}^{bckg} = 4\sigma\epsilon_d\epsilon_{bckg}A_d(T_d^3 + T_{bckg}^3) \quad (4.52)$$

Combining Equations (4.49) through (4.52) we obtain the expression for the total mean square fluctuation of the power flow into bolometer element as:

$$\begin{aligned} \overline{\Phi^2} = & 16k\sigma\epsilon_d\epsilon_{\text{bckg}}A_d(T_d^5 + T_{\text{bckg}}^5) \cdot \Delta f + \\ & + \frac{\epsilon_d\epsilon_{\text{target}}\pi A_d}{4(f/\#)^2} \cdot \frac{kC_1C_2}{\lambda^6} \frac{e^{C_2/\lambda T_{\text{target}}}}{(e^{C_2/\lambda T_{\text{target}}} - 1)^2} \cdot \tau(\lambda) \cdot \Delta\lambda \cdot \Delta f + \\ & + 2kG_{\text{cond}}(T_d^2 + T_0^2) \cdot \Delta f \end{aligned} \quad (4.53)$$

Using the expression for the bolometer pixel responsivity given by Equation (4.40) and taking into account Johnson noise defined by Equation (4.41) we can express the mean square fluctuation of the voltage signal across the bolometer with electrical bandwidth  $\Delta f$  as

$$\overline{V_{\text{noise}}^2} = R^2 \overline{\Phi^2} + 4kT_d R_d \Delta f \quad (4.54)$$

where mean square fluctuation of the power flux,  $\overline{\Phi^2}$ , is given in Equation (4.53).

#### 4.4.4 Predicted Performance of Microbolometer-Based M-WIP

Based on the proprietary data supplied by Andrew Wood of Honeywell, Inc. the radiometric model of microbolometer-based M-WIP was developed using general sensor model given by Equation (2.19). The simulated detected signal, computed based on this model, is shown in Figure 4.24 for 11-filter M-WIP with filters in the spectral range from 4  $\mu\text{m}$  to 14  $\mu\text{m}$  and 10% fractional bandwidth.

Using the performance prediction method described in Section 4.1 the M-WIP performance of microbolometer UFPA was analyzed for gray targets as well as for targets with spectral emissivity linearly dependent on wavelength. This analysis takes into account the thermal fluctuation noise (both radiation and conduction) as well as Johnson noise defined by Equation (4.54). The resulting performance predictions are shown in Figure 4.25 for blackbody targets and targets with emissivities linearly dependent on wavelength.

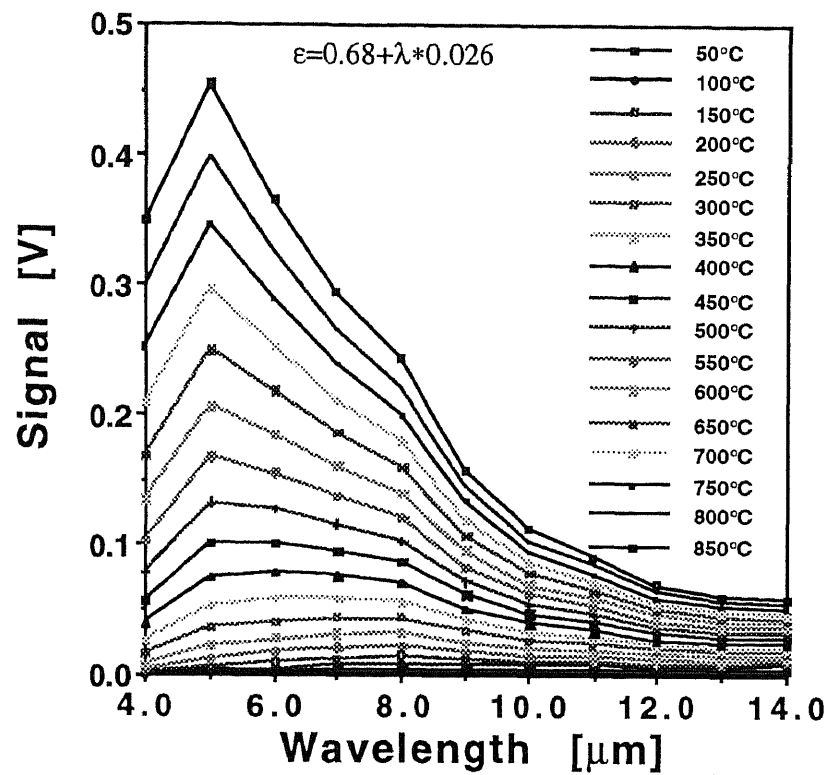


Figure 4.24 Simulated UFPA signal for IR filters with 10% fractional bandwidth

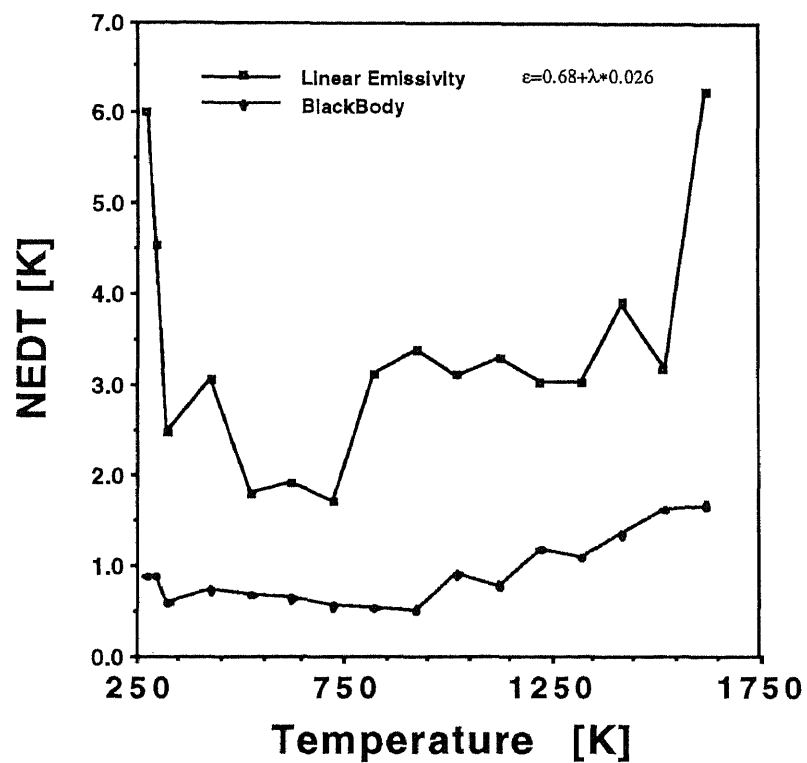


Figure 4.25 UFPA M-WIP performance for filters with 10% fractional bandwidth

## CHAPTER 5

### EXPERIMENTAL 7-FILTER LINE-SENSING M-WIP SYSTEM

#### 5.1 General Description of the System

As illustrated by the schematic diagram shown in Figure 5.1, the experimental M-WIP system consists of an IR camera with associated electronics, an IR filter assembly, and an image data processing system [33].

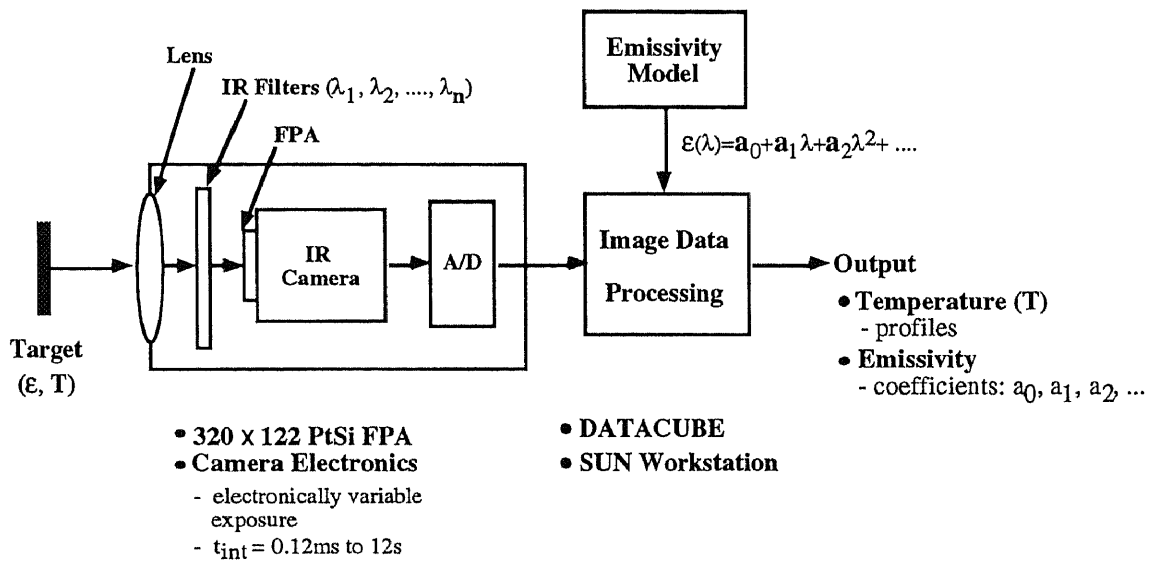


**Figure 5.1** Schematics of experimental NJIT Multi-Wavelength Imaging Pyrometer

**Hardware.** The experimental Multi-Wavelength Imaging Pyrometer uses a Sarnoff 320x244 PtSi IR-CCD imager with custom-built electronics allowing for imager operation with variable optical integration time as described in Section 5.3. A line-sensing filter assembly with 7 narrow-band IR filters having center wavelengths in the range from 1790nm to 4536nm is positioned in front of the imager FPA. The filter assembly and associated optics is further described in Section 7.2. The image processing system, described in more detail in Section 5.4, consists of a 10 MHz DATACUBE MaxVideo system hosted by SUN 4/330 workstation.

**Software.** The existing M-WIP system uses DATACUBE ImageFlow software for image processing as well as X-windows-based interface. A software package for least-squares-based calibration and real-time M-WIP measurements, presented in Chapter 6, has been developed under UNIX platform.

## 5.2 M-WIP Filters and Optics

The initial configuration of experimental M-WIP system utilized mosaic filter assembly proposed by Dr. C. N. Manikopoulos. This filter assembly consisted of six rectangular IR filters of various sizes as illustrated in Figure 5.2. This filter assembly provided for spectral measurements of radiance for point targets. However, due to disjoint nature of resulting distribution of the spectral information across focal plane array, this assembly did not allow to obtain continuous temperature profiles on the target surface.

To better utilize two-dimensional imaging capability of the M-WIP imager the filter assembly described above was substituted with a line-sensing filter assembly consisting of 7 narrow-band striped filters mounted on FPA packaging. The line-sensing assembly currently employed at NJIT uses  $f/1.4$  spherical lens in order to focus the image of the radiant target on the narrow horizontal slit. The image of the target area defined by the slit aperture is then refocused on FPA in horizontal direction using cylindrical lens as illustrated in Figure 5.3. As the result, the image of the horizontal line on the target surface is "spread" across all M-WIP filters in vertical direction while preserving horizontal resolution.

The line-sensing assembly fabricated by Optical Filter Corporation (OFC), Natick, MA, consists of seven filter stripes, 15x3mm each. Two additional filters are positioned at the edges of the assembly to provide mounting borders. All filter stripes are epoxied together with inter-filter gaps painted by opaque material in order to eliminate the optical leakage and crosstalk.



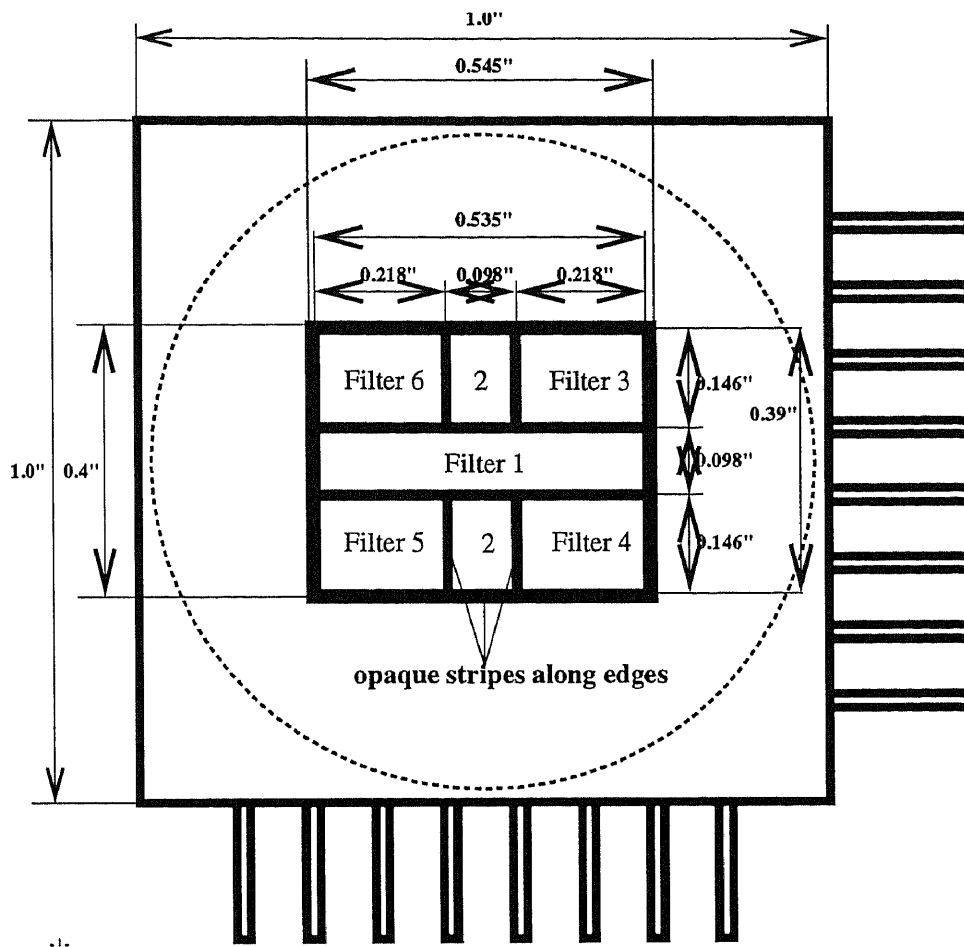


**Figure 5.2** Mosaic filter assembly initially utilized in experimental M-WIP system

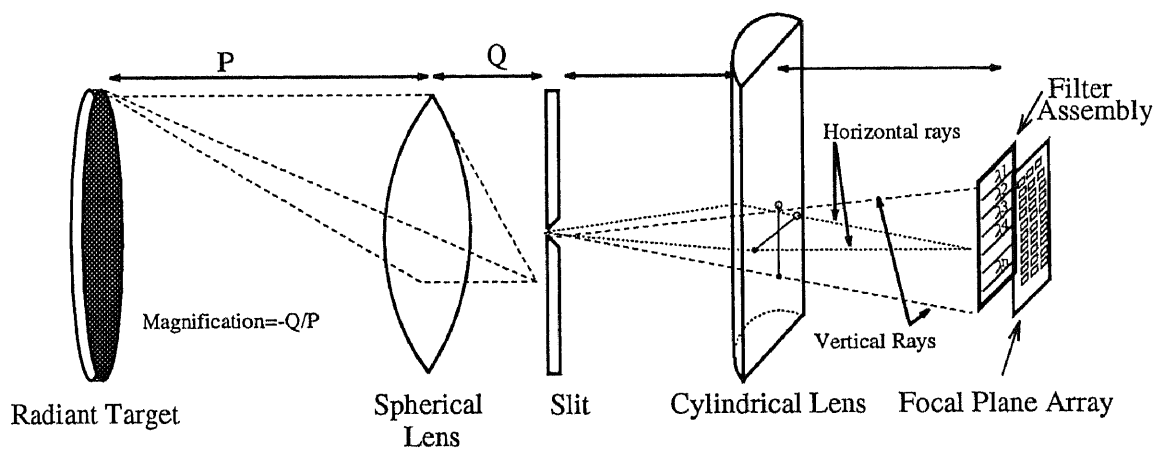


**Figure 5.3** Filter optics employed in experimental line-sensing NJIT M-WIP system

An image of this filter assembly captured from the actual video frame is shown in Figure 5.4. The central wavelengths,  $\lambda_0$ , of the filters ranging from 1790nm to 4536nm (at cryogenic temperature of 77K) correspond to the spectral sensitivity of the PtSi Schottky-barrier detectors (SBDs) used in the camera. As shown in Table 5.1, the bandwidths of the filters at half of peak transmission range from 51 nm for the 1790-nm filter to 102 nm for the 4536-nm filter. The values of the peaks of the filter transmissions were individually attenuated in order to provide approximately equal detected signal at all wavelengths for blackbody target at 700°C. The attenuation of the IR filters in this manner partially compensates for the spectral variations in the detected signal levels and, therefore, reduces the requirements on the dynamic range of the camera.

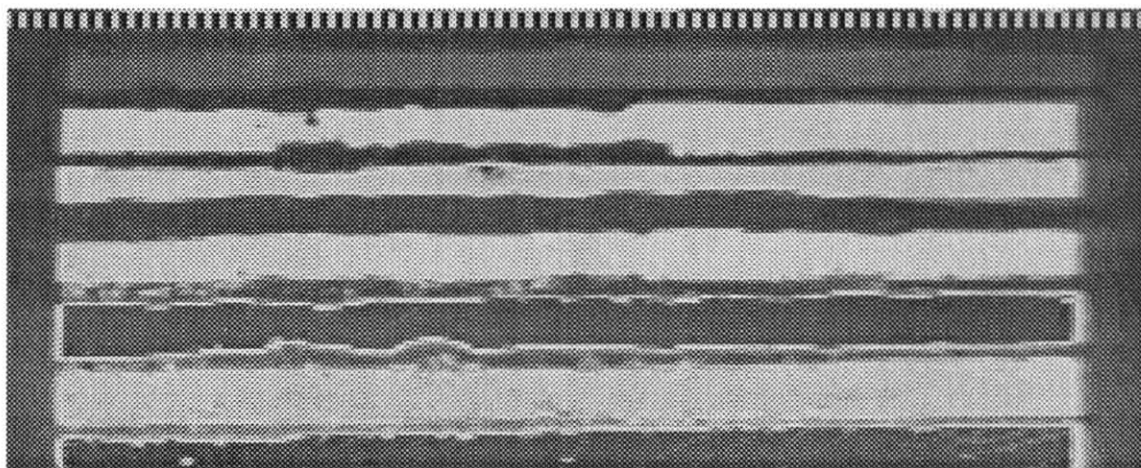


**Figure 5.4** Video image of line-sensing filter assembly

The spectral scans of all filters prior and subsequent to attenuation were performed by OFC in order to verify the need for blocking of high order transmission peaks. Furthermore, the effects of cryogenic temperature (77K) on the spectral characteristics of the filters were investigated. As illustrated in Table 5.1, the thermal contraction at cryogenic temperature has the effect of increasing filter bandwidths by approximately 4% and decreasing the values of central wavelengths by about 1%.

**Table 5.1** Spectral characteristics of M-WIP filters (Optical Filter Corporation)

Filter No.	Prior to Attenuation			Subsequent to Attenuation				
	Room Temperature			Room Temperature			77K	
	CW [nm]	BW [nm]	TR [%]	CW [nm]	BW [nm]	TR [%]	CW [nm]	BW [nm]
1	1797	47	60	1803	49	14	1790	51
2	2189	55	82	2192	61	13	2180	64
3	2596	57	61	2595	58	12.5	2580	60
4	3180	44	66	3179	36	25	3158	38
5	3462	53	48	3467	57	35	3447	60
6	3993	73	33	N/A	N/A	N/A	3970	77
7	4512	106	79	N/A	N/A	N/A	4536	102

CW - Center Wavelength; BW - Bandwidth; TR - Peak Transmission

### 5.3 320x244 PtSi IR-CCD Camera and It's Operation

An experimental NJIT M-WIP system is based on an infrared CCD camera system that was constructed to operate the Sarnoff (David Sarnoff Research Center, Princeton, NJ) 320X244 Schottky-barrier IR-CCD Focal Plane Array (FPA) as a non-interlaced 320X122-element multi-wavelength imaging radiometer [34].

To achieve wide dynamic range required for M-WIP, the imager was operated in a non-interlaced format with variable optical integration times ranging from 120 $\mu$ sec to 12sec. Subframe integration time control was achieved by employing a double detector readout. To facilitate this operation, camera circuitry was developed for automatically controlling the CCD waveforms to operate at the required integration time. This imager was

also operated in a multi-frame integration mode with a single detector readout for optical integration times in multiples of 33 ms. The analog video signal was digitized to 12-bits resolution. Circuits were also developed to embed critical information in the video signal to facilitate radiometric post-processing. An optoelectronically buffered digital interface was developed to connect the camera system to a DATACUBE image processing system hosted by SUN workstation [16].

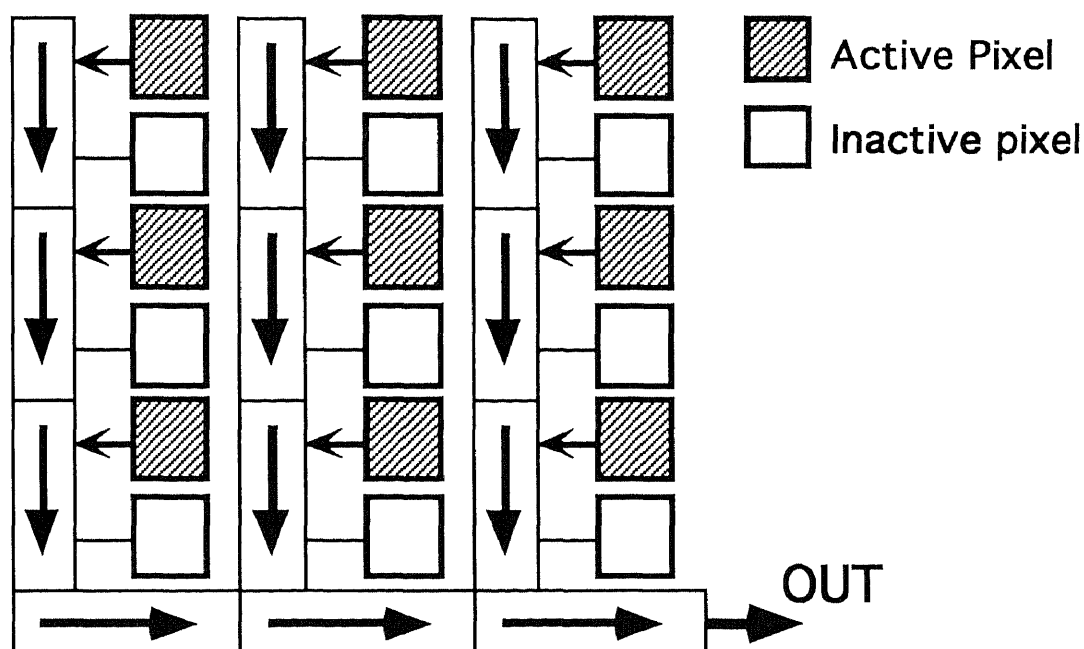


**Figure 5.5** Schematic of the Sarnoff 320X244 IR-CCD FPA

The imager utilized in the experimental M-WIP system uses PtSi Schottky-barrier detectors (SBDs) with internal photoemission generating electrical charge proportional to the incident optical signal. The useful spectral bandwidth is from 1.5 to 5.5 $\mu\text{m}$ . The camera is operated in a non-interlaced mode utilizing 122 vertical elements (single field) per frame. Shown in Figure 5.5 is a representation of the imager geometry. Two vertically adjacent photodetectors share a common vertical transfer register CCD. By utilizing only one field, one detector is assigned to a vertical register. This charge is transferred

downward at the rate of one register per line time ( $63.55\mu\text{s}$ ). At the bottom of these registers, a horizontal register (C) clocks the charge out to an on-chip output amplifier at the photodetector rate.

The camera can operate with two choices of integration time control. For integration times less than 33 milliseconds, i.e. for sub-frame integration time, the imager is operated with a double SBD transfer per frame where the detectors are allowed to saturate until the first transfer pulse dumps this charge into the registers. After clearing this charge and integrating for a precisely controlled time, the second transfer pulse reads out the detected signal. Without a built-in drain to clear excess detected charge, this charge is swept out through the normal readout channels. During the sweep out procedure, signal charge is being integrated in the detectors. Therefore, to obtain short integration times, the dumped charge needs to be swept out in the shortest possible time. The sweep out procedure begins as the charge that has accumulated in the detectors from the last transfer pulse is transferred to the B-registers through a transfer pulse. The B-registers are then clocked rapidly and charge immediately saturates the C-registers that are simultaneously clearing charge through the output drain. The charge is cleared from the B-registers in two line times but three additional line times are required to clear the C-registers. The minimum sub-frame optical integration time available for this camera is two line times or  $127\mu\text{s}$  [35].

For integration times greater than or equal to 33 milliseconds, the camera operates with a single SBD transfer pulse per optical integration time. This mode will be referred to as the multi-frame integration mode. The multi-frame integration mode is used for imaging scenes of low temperature. In this case the reduction in the radiant flux causes a reduction in the amount of charge signal integrated over standard 33 ms operation. This decreases the signal to noise ratio and the response of the camera tends to deviate from linearity. To improve the radiometric performance, the optical integration time should be increased. This is accomplished by suppressing the SBD readout for a (N) number frames (while the

imager operates at the frame rate of 30 frames/sec). However, for every N frames only one frame contains the detected signal charge. For operation in multi-frame integration mode with integration time of 33 ms or multiples of 33 ms, the SBD are readout only once per optical integration time [35].

#### **5.4 Signal Processing System**

Image data processing for M-WIP is based on the DATACUBE MaxVideo system using a SUN workstation as the host computer [36]. The DATACUBE MaxVideo system is a user configurable real-time image acquisition and processing system. It consists of a number of modules that can be interconnected to suit the image processing task. The modules are housed in a 20 slot VME chassis box (MAX-BOX) while a SUN 4/330 acts as the host computer. The system can operate at a maximum data rate of 10 MHz. DATACUBE MaxVideo system used in this work has one MAX-SCAN data acquisition module, two ROI-STORE 512Kbytes memory modules, three MAX-SP general purpose signal processing modules and one MAX-GRAPH video and graphics display module. A custom developed display board is used to reformat the 320x122 image for standard RS-170 display. The development software for the MaxVideo system is ImageFlow which consists of a set of C-callable libraries.

## CHAPTER 6

### CALIBRATION OF M-WIP SYSTEM AND EXPERIMENTAL RESULTS

#### 6.1 Compensation for Inherent System Non-Linearities

In order to obtain high radiometric accuracy of the M-WIP measurements we have found it necessary to compensate for non-linearities of the IR imager response [33]. In the case of the PtSi IR-CCD imager used in the experimental M-WIP system, both the dark current and the spectral responsivity of the Schottky-barrier detectors (SBDs) depend on the SBD bias voltage and decrease with increasing level of integrated charge signal. This dependence of the dark current and responsivity on the detected signal is especially pronounced at high signal levels resulting in a "saturation" non-linearity. On the other hand, the reduction of the signal due to apparent charge trapping losses is especially evident at low signal levels and represents "offset" nonlinearity.

##### 6.1.1 Dark Current Compensation

In order to compensate for the dark current charge signal, its generation rate was measured for a wide range of optical integration times. These measurements were performed with the imager shielded from IR radiation with a square sheet of indium placed over the photosensitive area, with the indium being in thermal contact with the dewar cold finger. The integration time was varied by operating the camera in the normal full-frame (33 millisecond integration time) mode and suppressing an integer number of charge transfer pulses to allow the detectors to integrate charge for multiple frame times. The computer was synchronized to the active signal by gating the vertical sync signal to pass only after dark current charge was transferred to the CCD registers.

Dark current measurements were taken for integration times greater than 66 milliseconds in increments of 33 milliseconds. Shown in Figure 6.1 is the dark current

signal versus integration time. It is seen from this figure that the generation rate of the dark current charge decreases with increasing optical integration time [16].

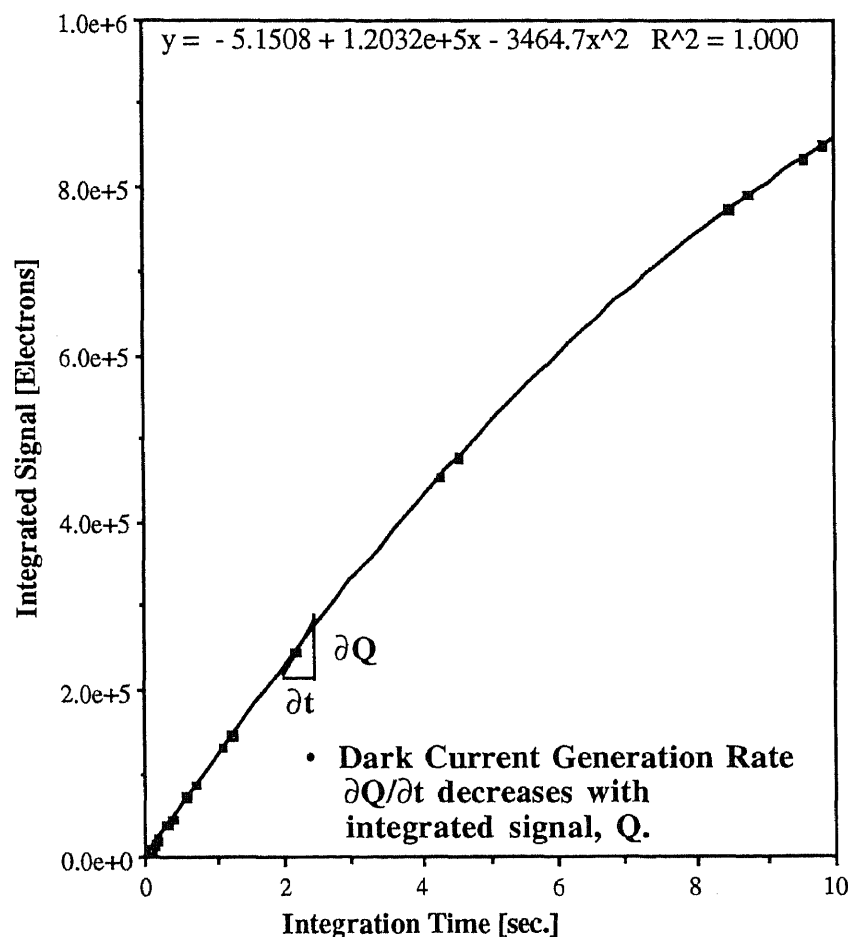


**Figure 6.1** Dark current signal for the 320x122 IR-CCD camera versus integration time

Our study of the dark current generation concluded that due the pixel-to-pixel non-uniformity the dark current compensation should be performed individually for each pixel. The dark current was measured for each pixel in the imager area that is used in normal operation. Shown in Figure 6.2 is a plot of the dark current for twenty representative pixels as function of the optical integration time.



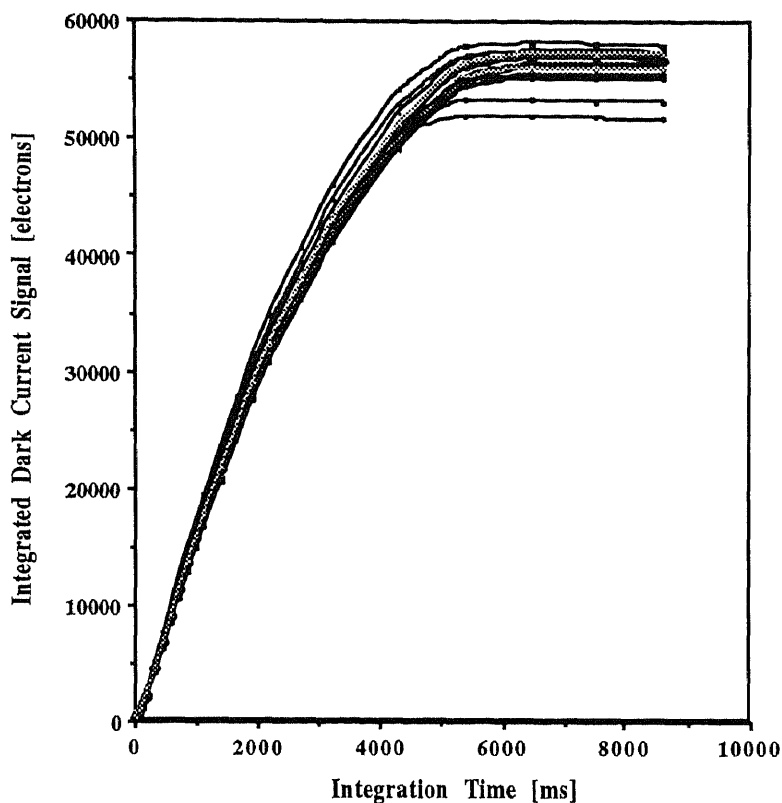


**Figure 6.2** Dark current non-uniformity for the 320x122 PtSi IR-CCD camera

In order to correct the detected signal for the dark current, the variation of the dark current as function of the signal level can be estimated according to the following algorithm:

1. Using cold-shield to prevent radiative flux from reaching the detectors, the dark current charge is experimentally measured for the wide range of optical integration times. The dark current is then approximated by an exponential function of integration time,  $t_{\text{int}}$ , as:

$$S_{\text{DC}}^{\text{measured}} = ae^{bt_{\text{int}}} + c \quad (6.1)$$

A derivative of Equation (6.1) with respect to the optical integration time,  $t_{\text{int}}$ , represents the dark current which can be expressed as function of the accumulated signal:

$$I_{DC}(S_{DC}^{\text{measured}}) = I_{DC}(S) = \frac{\partial S_{DC}^{\text{measured}}}{\partial t_{\text{int}}} = b(S_{DC}^{\text{measured}} - c) = b(S - c) \quad (6.2)$$

where  $S$  represents the total accumulated charge, regardless of its source.

It should be noted that right hand side of Equation (6.2) reflects the assumption that dark current is solely dependent on the magnitude of the accumulated signal level.

2. The dark current component of the signal integrated by the imager viewing the radiant target can now be expressed as:

$$S_{DC}^{\text{estimated}}(T, t_{\text{int}}) = \int_0^{t_{\text{int}}} I_{DC}(S(T, t)) dt = \frac{b}{k_2} (S(T, t_{\text{int}}) - k_1 - k_3) + b(k_3 - c)t_{\text{int}} \quad (6.3)$$

where  $S(T, t_{\text{int}}) = k_1 e^{k_2 t_{\text{int}}} + k_3$  - is the detected signal approximated by the exponential function of the optical integration time,  $t_{\text{int}}$ , and  $T$  is the temperature of the radiant target.

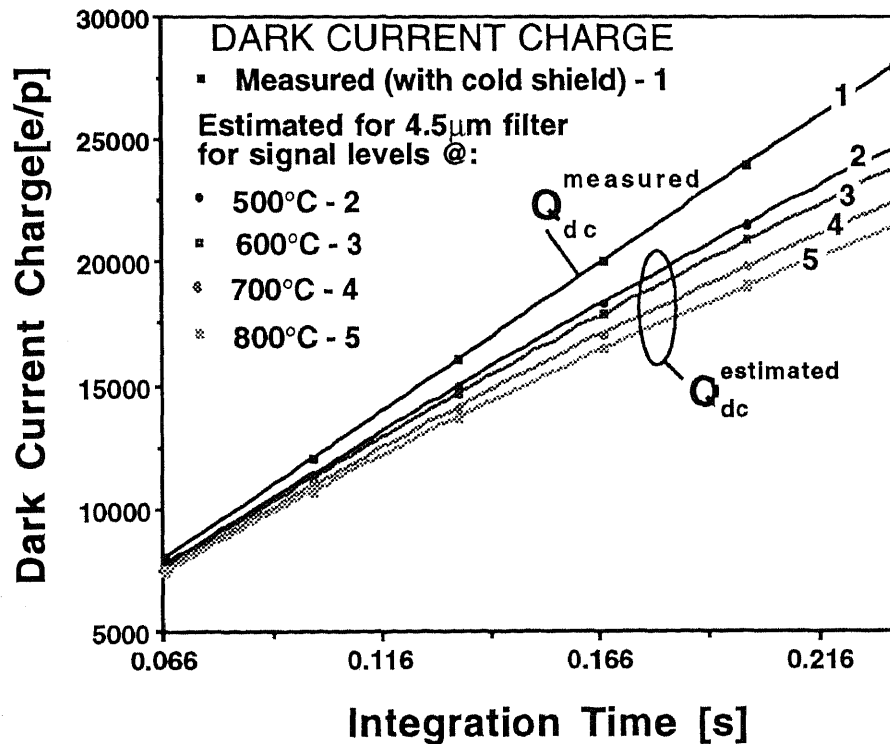


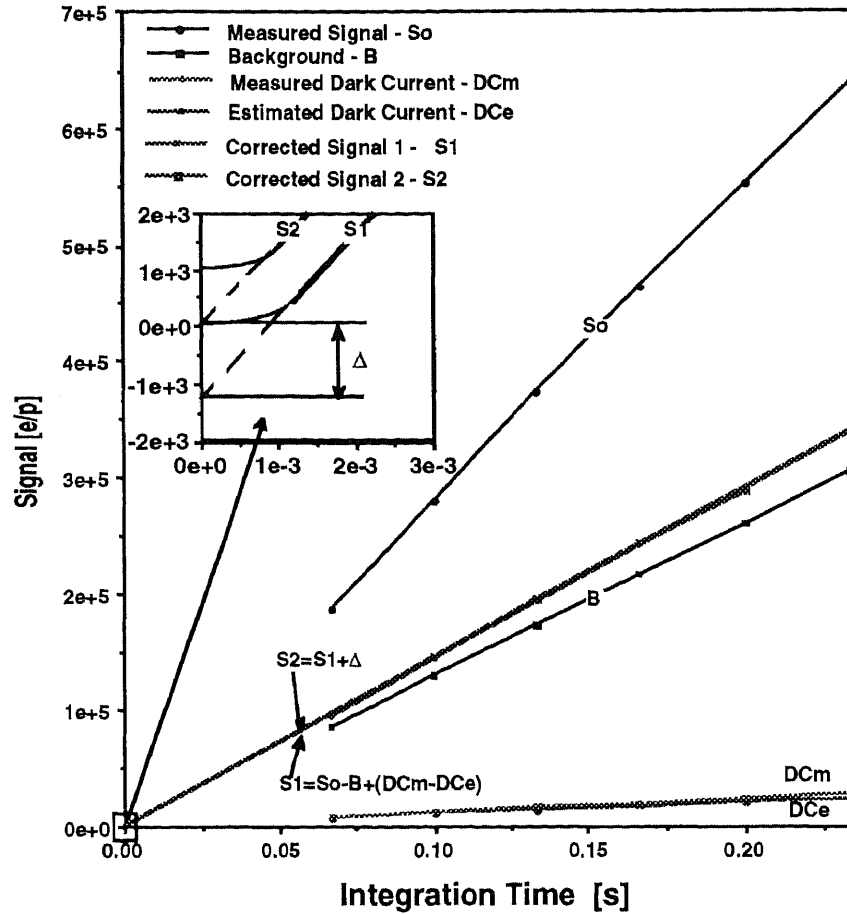
Figure 6.3 Measured and estimated dark current

Figure 6.3 illustrates the experimentally measured dark current charge,  $S_{DC}^{measured}$ , and the dark current charge estimated from Equation (6.3),  $S_{DC}^{estimated}$ , corresponding to the imager viewing the blackbody target at 500°C, 600°C, 700°C and 800°C through the 4.5- $\mu\text{m}$  filter.

At the early stages of this research the imager nonlinearities described above were compensated by the following algorithm [33]:

- The background measured at each optical integration time,  $t_{int}$ , was stored and subtracted from the detected signal.
- The dark current charge component of the background signal (to be subtracted from the detected signal) exceeds the dark current charge accumulated in the presence of the incoming radiant flux due to the dark current suppression at high signal levels. The excess dark current charge was computed based on Equations (6.1) and (6.3) and added back to the detected signal.
- Finally, the "offset" correction was performed in order to compensate for charge loss due to the apparent effect of charge trapping. The value of this correction was found from the linear projection of the signal to zero integration time. Subtraction of thus determined offset assures direct proportionality of the detected signal to the optical integration time.

The "evolution" of the detected signal due to the successive application of the above corrections is illustrated in Figure 6.4. It should be noted, that the initial version of the experimental M-WIP software did not include compensation for the saturation nonlinearity of imager response at high signal levels. Instead, initial M-WIP algorithm was limiting the consideration of the experimental data to the optical integration times for which the signal level does not exceed 50% of maximum charge handling capacity,  $Q_{max}$ . By limiting all M-WIP computations to relatively low signal levels, the "saturation" effects were reduced to less than 8%.



**Figure 6.4** Signal corrections employed by initial M-WIP algorithm

Based on the corrected for the dark current signal measurements we were able to demonstrate a temperature resolution of  $\pm 1$  °C for off-line M-WIP temperature measurements of the blackbody target in the range from 600°C to 900 °C, as illustrated in Figure 6.5. It should be noted, that these measurements were based on the pre-recorded data and did not include compensation for the non-linearity of the imager response. Furthermore, the same data set was used for system calibration and subsequent “restoration” of the target temperatures.

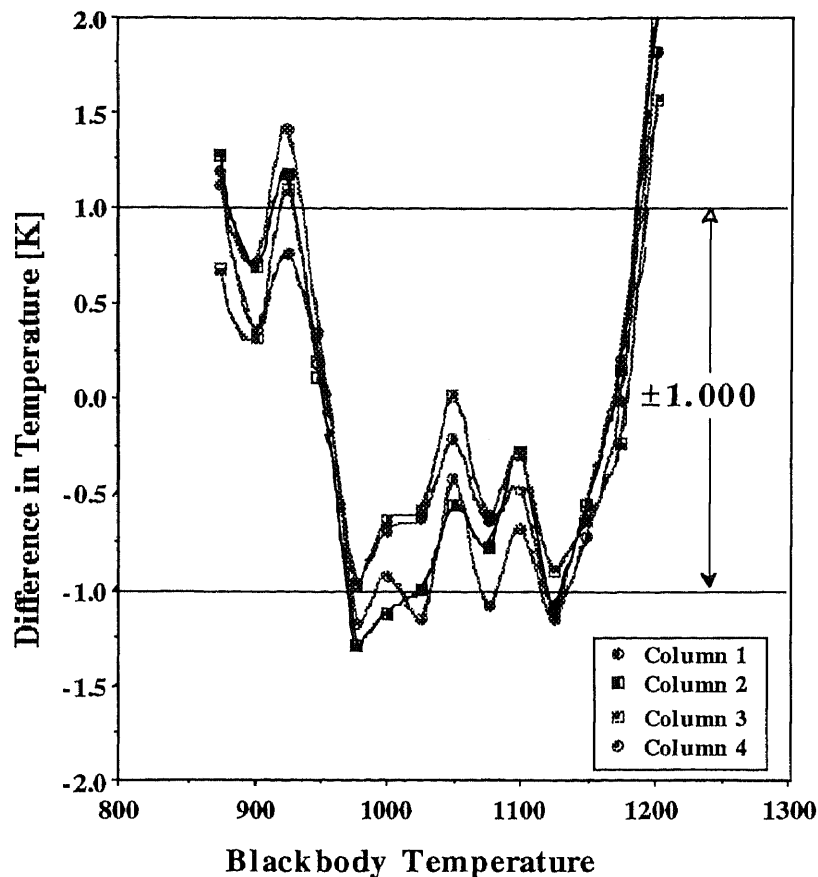


**Figure 6.5** Initial measurements of blackbody temperature based on prerecorded data

However, the "saturation" non-linearity of detector response resulted in very poor accuracy of the real-time M-WIP temperature measurements due to substantial variations in the detected signal levels. Therefore, the correction for "saturation" response non-linearity was subsequently incorporated into the M-WIP algorithm.

### 6.1.2 Correction for Saturation Non-Linearity of the Imager Response

In order to compensate for saturation non-linearity of the imager response it was assumed that this non-linearity represents the loss of the detector responsivity with rising bias voltage and, therefore, is primarily a function of the detected signal level. However, due to approximate nature of the dark current compensation described in the previous Section,

corrected for the dark current signal still exhibits some integration time dependent non-linearity. Therefore, our approach to signal linearization takes into account not only the absolute signal level,  $S^{\text{detected}}$ , but the intensity of the incident radiative flux,  $F$ , as well.

The pixel-by-pixel correction for offset and saturation non-linearities of IR imager response was achieved according to the following algorithm [33, 37, 38]:

1. Based on the experimental signal measurements for a wide range of the optical integration times, the detected signal is approximated by an exponential function of optical integration time,  $t_{\text{int}}$ , for each temperature,  $T_i$ , of the calibration source, as:

$$S^{\text{detected}} = a_1^i e^{a_2^i t_{\text{int}}} + a_3^i \quad (6.4)$$

2. For  $N$  various radiative fluxes corresponding to  $N$  various temperatures of the calibration blackbody source,  $T_i$ , the intensity of the incident on IR detectors radiative flux,  $F_i$ , is characterized by the ratio of the detected signal,  $S(T_i, t_{\text{int}})$ , to the value of optical integration time,  $t_{\text{int}}$ , as:

$$F_i = \frac{S(T_i, t_{\text{int}})}{t_{\text{int}}}, i = 1, \dots, N \quad (6.5)$$

3. The linearized signal corrected for off-set at zero integration time can now be expressed as function of the detected signal and the intensity of the incident radiative flux as:

$$S^{\text{linear}} = \left. \frac{\partial S^{\text{detected}}}{\partial t_{\text{int}}} \right|_0 \times t_{\text{int}} = a_1^k \cdot a_2^k \cdot t_{\text{int}} = a_1^k \cdot \ln \left( \frac{S^{\text{detected}} - a_3^k}{a_1^k} \right) \quad (6.6)$$

where index  $k$  is determined from the following condition (assuming that  $F_k$  are sorted in the ascending order):

$$\frac{F_k + F_{k-1}}{2} < \frac{S^{\text{detected}}}{t_{\text{int}}} < \frac{F_k + F_{k+1}}{2} \quad (6.7)$$

The radiative flux intensities used for M-WIP calibration,  $F_i$ , are stored in the ascending order along with corresponding coefficients  $a_1^i$  and  $a_3^i$  in the correction table for each pixel. During the on-line M-WIP temperature measurements these tables are searched according to the criteria given by Equation (6.7). Once the appropriate flux level,  $F_k$ , has been determined, the corresponding correction coefficients  $a_1^k$  and  $a_3^k$  are then used for signal linearization according to Equation (6.6).

Figure 6.6 illustrates the correction for saturation non-linearity resulting from application of the above algorithm to the signals detected by M-WIP through 4500nm filter illuminated by the blackbody source at 600°C.

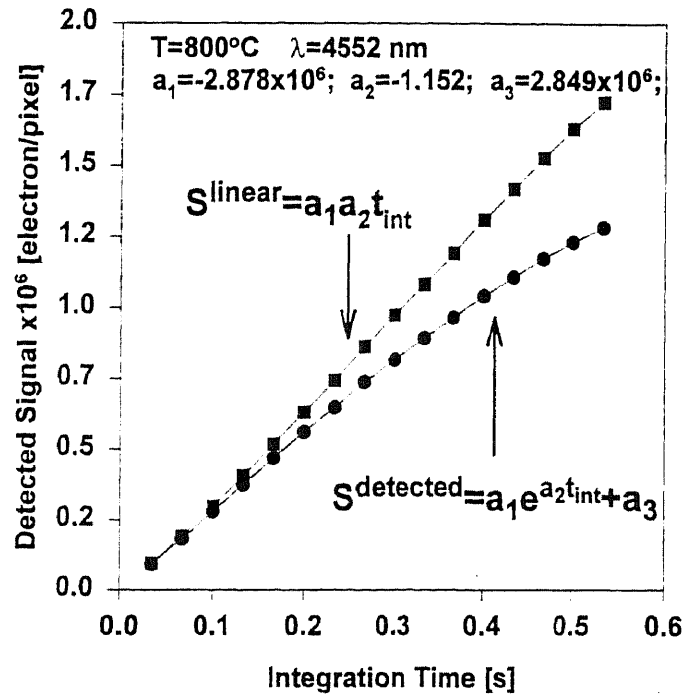


**Figure 6.6** Saturation non-linearity correction

In addition, it was found that response non-linearity at low signal levels is approximately equal that of the background signal. Based on this observation the direct "offset" correction was eliminated, resulting in the following approach to the compensation of response non-linearities:

- First, the dark current charge levels corresponding to radiant target and background signals are estimated from Equation (6.3) for the current value of the optical integration time based on the above described algorithm. The estimated dark current charges are then subtracted from radiant target and background signals, respectively.
- Next, the correction for saturation non-linearity is applied to both radiant target and background signals based on the algorithm given by Equations (6.4)-(6.7).
- Finally, the linearized background signal is subtracted from the linearized radiant target signal.

## **6.2 Fixed Signal Level M-WIP Operation for Non-Linearity Independent Real-Time Temperature Sensing**

The compensation for non-linearity of IR imager response, as described in Section 6.2, is based on pre-stored correction coefficients does not completely linearize the signal due to on-line gain and offset fluctuations. Consequently, the accuracy of M-WIP temperature measurements was somewhat reduced due to the residual non-linearity of the imager response.

To avoid the problem of inaccurate non-linearity compensation we have developed an algorithm that provides, to a large degree, non-linearity independent real-time M-WIP temperature estimation [39]. This algorithm exploits the ability of the imager to change on-line the duration of the optical integration time by suppressing the detector readout pulse for a number of frames. Using this capability, we are able to find the value of optical integration time yielding the pre-selected signal level for any target temperature. Thus, for each M-WIP spectral channel the imager always integrates electron charge up to the same pre-selected signal level with corresponding values of the optical integration time being used for least-squares estimation of target temperature and emissivity. Due to the M-WIP operation at the constant signal level for each spectral channel, the signal non-linearity is the



same for all target temperatures and is compensated for by the calibration algorithm without affecting the accuracy of M-WIP temperature sensing. This concept is illustrated in Figure 6.7 for the case of equal pre-selected signal levels for all spectral channels.

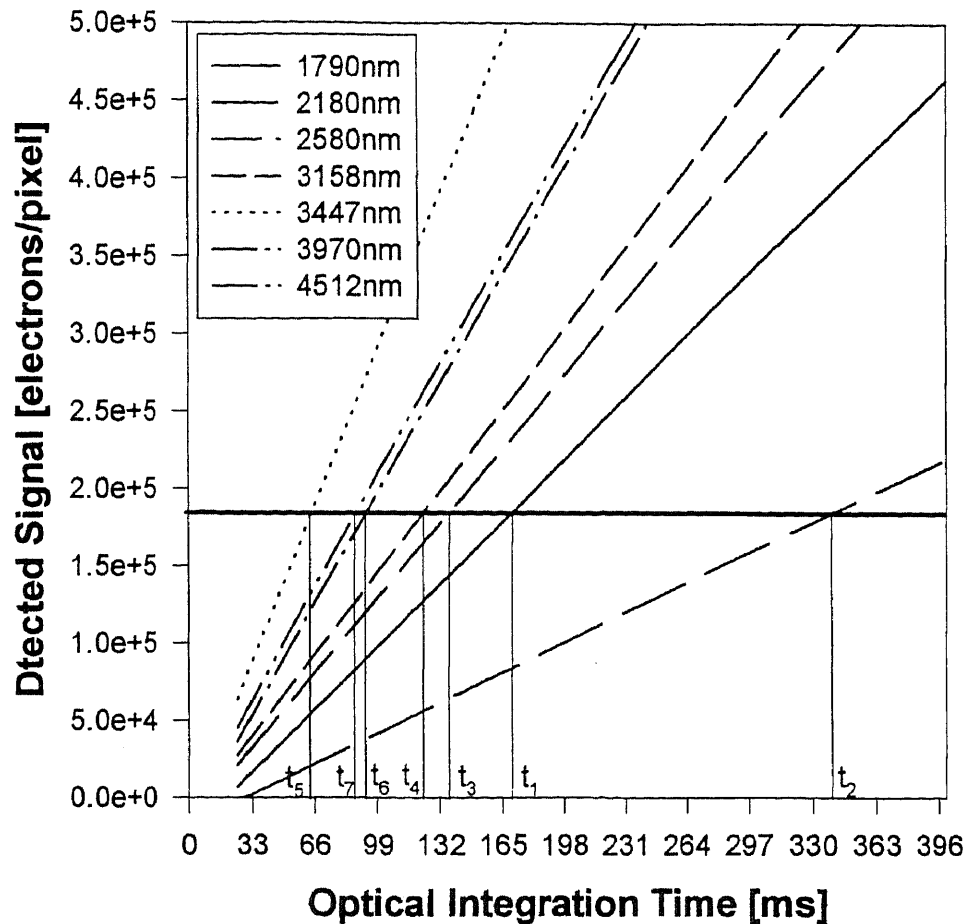


**Figure 6.7** Optical integration times corresponding to fixed pre-selected signal level

The algorithm for on-line estimation of the values of the optical integration times corresponding to the pre-selected operational signal levels is as follows:

- The duration of the optical integration time is increased in frame-time increments with computer workstation supplying the appropriate integration time codes to the timing circuitry of the imager. This process is continued until the detected signal levels at all spectral channels exceed the corresponding pre-selected signal levels. In other words,

the integration time is increased until:

$$S_{\lambda_i}^{\text{detected}}(k \cdot t_{\text{frame}}) > S_{\lambda_i}^{\text{fixed}}, \text{ for all } i = 1, \dots, M \quad (6.8)$$

where  $M$  is the number of M-WIP spectral channels;  $S_{\lambda_i}^{\text{detected}}$  is the signal level detected at the  $i$ -th spectral channel;  $S_{\lambda_i}^{\text{fixed}}$  is the pre-selected fixed signal level for the  $i$ -th spectral channel;  $t_{\text{frame}} = 8.32\text{ms}$  is the frame time;  $k$  is the number of the current integration time step;

- Next, the detected signal levels bracketing corresponding pre-selected signal level are determined for each spectral channel from:

$$S_{\lambda_i}^{\text{detected}}((m_i - 1) \cdot t_{\text{frame}}) < S_{\lambda_i}^{\text{fixed}} < S_{\lambda_i}^{\text{detected}}(m_i \cdot t_{\text{frame}}) \quad (6.9)$$

where  $m_i$  is the number of the time step for which the detected signal at the  $i$ -th spectral channel just exceeds the corresponding pre-selected signal;

- Finally, the value,  $t_i$ , of the optical integration time yielding the pre-selected signal level at the  $i$ -th channel is determined by linear interpolation as:

$$t_i = t_{\text{frame}} \times \left[ m_i + \frac{S_{\lambda_i}^{\text{fixed}} - S_{\lambda_i}^{\text{detected}}(m_i \cdot t_{\text{frame}})}{S_{\lambda_i}^{\text{detected}}(m_i \cdot t_{\text{frame}}) - S_{\lambda_i}^{\text{detected}}((m_i - 1) \cdot t_{\text{frame}})} \right] \quad (6.10)$$

- Once the integration times,  $t_i$ , have been determined, we proceed to evaluate the corresponding background signal levels,  $B_i(t_i)$ , as:

$$B_{\lambda_i}(t_i) = B_{\lambda_i}^{\text{detected}}(m_i \cdot t_{\text{frame}}) + \left[ \left( \frac{t_i}{t_{\text{frame}}} + m_i \right) \times \right. \\ \left. \times (B_{\lambda_i}^{\text{detected}}(m_i \cdot t_{\text{frame}}) - B_{\lambda_i}^{\text{detected}}((m_i - 1) \cdot t_{\text{frame}})) \right] \quad (6.11)$$

- At the final step we perform background subtraction and dark current compensation to obtain corrected signal levels,  $S^{\text{corrected}}$ , to be used for M-WIP temperature estimation:

$$S_{\lambda_i}^{\text{corrected}} = S_{\lambda_i}^{\text{fixed}} - B_{\lambda_i}(t_i) + S^{\text{DC}}(B_{\lambda_i}(t_i), t_i) - S^{\text{DC}}(S_{\lambda_i}^{\text{fixed}}, t_i) \quad (6.12)$$

where  $S^{\text{DC}}(B_{\lambda_i}(t_i), t_i)$  and  $S^{\text{DC}}(S_{\lambda_i}^{\text{fixed}}, t_i)$  are the dark current charges estimated from Equation (6.3) for signal levels  $B_{\lambda_i}(t_i)$  and  $S_{\lambda_i}^{\text{fixed}}$ , respectively.

We now turn our attention to the problem of selecting the fixed operating signal levels to be used in the above algorithm. We note, that the above algorithm provides for the integration of the radiative target signal up to a pre-selected fixed signal level for each M-WIP channel, regardless of target temperature. It can be seen from Equations (6.11) and (6.12) that the detected signal is being corrected for the background, with background evaluated at the same optical integration time as the signal detected from the radiative target. Therefore, background signal levels used for background compensation vary depending on the intensity of the emitted by the target radiative flux. Consequently, the effect of the imager response non-linearity on background signals vary with intensity of the target radiation, making result of M-WIP measurements somewhat dependent on the magnitude of background signals. Thus, the choice of the appropriate signal level for each M-WIP spectral channel involves a compromise between poor signal-to-noise-ratio at low signal levels and high background non-linearity and dark current at long integration times corresponding to elevated levels of operating signals.

In practice, we choose operating signal levels for all channels based on pre-recorded calibration data, as to minimize the M-WIP temperature estimation error. For an N-channel M-WIP this procedure calls for the minimization of a function of N variables. This minimization is accomplished by the method of simulated annealing as follows:

- First, the signals detected by an M-WIP imager viewing the blackbody calibration source are recorded for a wide range of blackbody temperatures.
- Next, the initial values of the operating signal levels are selected for all channels as 1/4 of the maximum charge handling capacity of the imager,  $Q_{\max} \approx 1.2E+6$  electrons/pixel. Based on these signal levels the corresponding integration times are then computed for all channels and all calibration temperatures from Equation (6.10). The effective values of central wavelengths and peak transmissions of all M-WIP channels are subsequently determined based on the calibration algorithm given by Equation (6.16).
- Next, we form an error function,  $\Delta T^2$ , as:

$$\Delta T^2 = \max \left\{ \left( T_k^{\text{calibration}} - T_k^{\text{estimated}} \right)^2 \right\}, \quad k = 1, \dots, L \quad (6.13)$$

where:  $L$  is the total number of blackbody temperature set-points used for M-WIP calibration;  $T_k^{\text{calibration}}$  is the  $k$ -th blackbody set-point;  $T_k^{\text{estimated}}$  is M-WIP estimation of the  $k$ -th blackbody set-point based on pre-recorded signal measurements.

- Having defined error function and the initial values of the operating signal levels we utilize a simulated annealing algorithm to determine the optimum values of operating signal levels by solving the following minimization problem:

$$\min_{S_{\lambda_1}^{\text{fixed}}, \dots, S_{\lambda_N}^{\text{fixed}}} \left\{ \Delta T^2 \left( S_{\lambda_1}^{\text{fixed}}, \dots, S_{\lambda_N}^{\text{fixed}} \right) \right\} \rightarrow S_{\lambda_1}^{\text{fixed}}, \dots, S_{\lambda_N}^{\text{fixed}} \quad (6.14)$$

Typical values of operating signal levels,  $S_{\lambda_i}^{\text{fixed}}$ , as determined from Equation (6.14), are shown in Table 6.1 along with corresponding values of optical integration times. The inspection of Table 6.1 shows that typical operating signal levels are significantly smaller than the maximum charge handling capacity of the imager,  $Q_{\max} \approx 1.2E+6$  electrons/pixel.

Consequently, M-WIP operates at relatively short optical integration times, minimizing the effect of background non-linearity and dark current on the accuracy of temperature estimation.

**Table 6.1** Fixed operating signal levels and corresponding optical integration times

Target Temp. °C	M-WIP Spectral Channels, nm						
	1790	2180	2580	3158	3447	3970	4536
	Operating Signal Levels, x1000 electron/pixel						
	191	194	404	247	330	574	705
	Optical Integration Times, ms						
500	203	159	254	139	117	220	193
550	175	127	195	112	93	188	171
600	146	99	150	91	75	161	152
650	119	76	115	73	60	138	135
700	94	58	90	60	49	119	120
750	73	45	71	50	41	103	107
800	57	35	56	41	35	90	96
850	44	27	46	35	29	79	87
900	35	22	37	30	25	70	78
950	27	18	31	25	22	62	71
1000	22	14	26	22	19	56	65

### 6.3 Calibration of NJIT M-WIP System

As was explained in Chapter 3 the M-WIP temperature measurements are based on the detection of the target thermal radiance at several distinct wavelengths/channels. Therefore, the accurate knowledge of the spectral characteristics of each M-WIP channel is crucial to the overall performance of the system. The simulations show that 5% error in the

specification of the central wavelengths of the M-WIP channels leads to reduction of the accuracy of M-WIP temperature measurements by approximately factor of 2 [12].

In the case of M-WIP systems based on narrow-band interference IR filters, the spectral characteristics of each M-WIP channel depend not only on the “area” of the prime transmission bands of the filters, but also on the out-of-band rejection and the spectral transmission of the optics throughout the optical path of the system. Therefore, the effective M-WIP calibration algorithm should provide for the evaluation of the effective spectral characteristics of M-WIP channels taking into account the spectral properties of all optical components of the system.

### 6.3.1 Initial Calibration of M-WIP Spectral Characteristics

The initial calibration of experimental NJIT M-WIP system relied on a least-squares-based calibration algorithm for the evaluation of the effective values of peak filter transmissions ( $\tau_o$ ) and center wavelengths ( $\lambda_o$ ) based on the detection of radiation emitted by the pre-calibrated blackbody source over a wide range of temperatures:

$$\min_{\tau_o, \lambda_o} \sum_{i=1}^M \left\{ \frac{1}{\sigma_i^2} \left[ S_i - \tilde{S}(T_i^{BB}, \tau_o, \lambda_o) \right]^2 \right\} \rightarrow \tau_o, \lambda_o \quad (6.15)$$

where:  $T_i^{BB}$  is  $i$ -th temperature of the reference blackbody source (K),  $\sigma_i = \Delta S_i = \sqrt{S_i}$  is rms signal noise (rms electrons per pixel).

For the purpose of M-WIP calibration we have used an M360 blackbody source manufactured and calibrated by Micron Instrument Company, Inc., Wyckoff, New Jersey. According to manufacturer specifications the model M360 blackbody operates in the temperature range from 50°C to 1100°C with accuracy of  $\pm 0.2\%$  of reading  $\pm 1^\circ\text{C}$ . The M360 has heated cavity of spherical shape with aperture of 25 mm in diameter defining

solid angle of  $20^\circ$ . The M360 is controlled by digital self-tuning PID controller. The blackbody was calibrated against NIST-traceable metal freeze point calibration sources using zinc, aluminum and silver. The certificate of calibration is shown in Figure 6.9.

A seven-filter experimental M-WIP system was initially calibrated according to Equation (6.15) against a reference blackbody source over a temperature range from  $450^\circ\text{C}$  to  $900^\circ\text{C}$ . It should be noted, that the initial calibration did not include the compensation for saturation non-linearity of the imager response. This calibration resulted in an effective radiometric uniformity correction of all camera pixels used for the M-WIP measurements. However, due to self-compensation for non-linear response of the imager by the calibration algorithm, the initial calibration resulted in a shift of the effective center wavelengths of the filters in the range of 28 to 358 nm as compared to manufacturer specifications (see column II of Table 6.2). In order to study this effect, the M-WIP "calibration" was also performed on the basis of the simulated signal with various values of "offset" and "saturation" non-linearities. It was found, as illustrated in column III of Table 6.2, that "offset" non-linearity of 2.5% of  $Q_{\text{max}}$  at zero optical integration time (i.e.  $t_{\text{int}}=0$ ) and "saturation" non-linearity of 8% at 50% of  $Q_{\text{max}}$  results in similar shifts in effective center wavelengths of IR filters as was obtained for the experimental data not compensated for imager non-linearity.

As shown in the column IV of Table 6.2 the correction for "saturation" nonlinearity of the imager response resulted in the calibration of M-WIP filters with the center wavelengths representing a much closer match to the manufacturer specifications.

Figure 6.8 illustrates a simulation study of the expected M-WIP temperature resolution as a function of the "saturation" non-linearity for four different cases. Curves 1 and 2 show predicted temperature resolution for the case where the center wavelengths of the filters were optimized by the M-WIP calibration cycle. In the case of curves 3 and 4, the center wavelengths of M-WIP filters were obtained from the manufacturer specifications. It should be noted, that in all cases the filter bandwidths were determined from manufacturer

specifications. It has also been assumed in all cases that the M-WIP was calibrated against the blackbody reference source and that the same blackbody source served as the target for M-WIP measurements. Curves 1 and 3 illustrate simulated M-WIP measurements using constant spectral emissivity model ( $\epsilon = a_0$ ), which assumes that the target is a graybody radiator. However, curves 2 and 4 correspond to a color target characterized by a linear emissivity model ( $\epsilon = a_0 + a_1 \cdot \lambda$ ). A comparison of curves 1 and 3 demonstrates that the values of the filter wavelengths, determined by the least-squares-based M-WIP calibration cycle, effectively compensate for the response non-linearity of the IR imager. It should also be noted that the temperature resolution of  $\Delta T = 1.0^\circ\text{C}$  predicted by the curve 1 in Figure 6.8 corresponds to the "saturation" nonlinearity of about 6% and is consistent with the experimental results shown in Figure 6.13 Figure 6.15 and the data presented in Table 6.2.

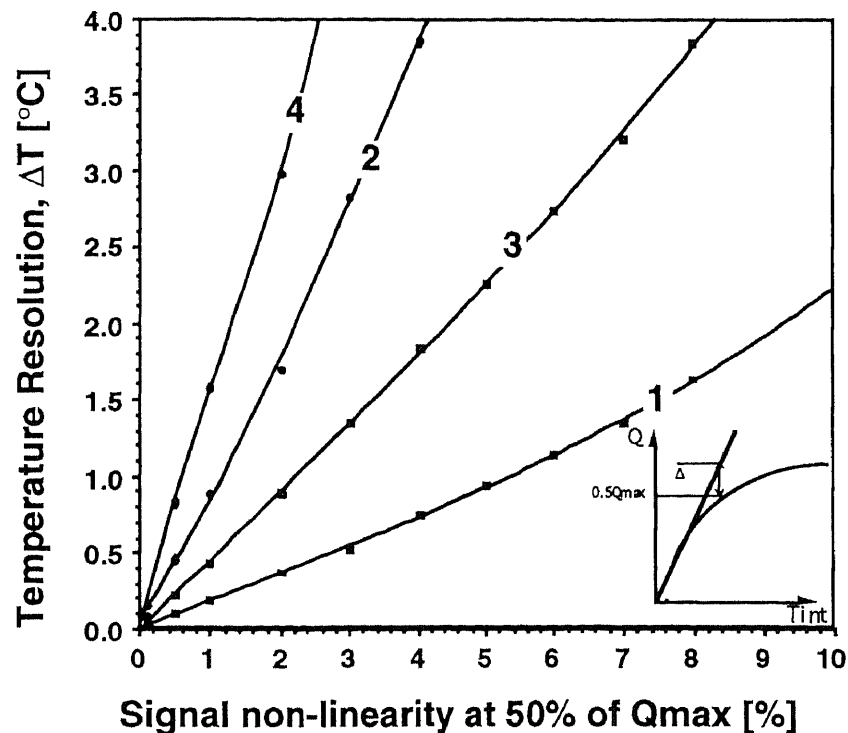


**Figure 6.8** Estimated effect of response nonuniformity on M-WIP temperature resolution:

- 1 - gray body & filter calibration, 2 - color body & filter calibration,
- 3 - gray body & pre-measured filters, 4 - color body & pre-measured filters



## CERTIFICATE OF CALIBRATION



MIKRON INSTRUMENT COMPANY, INC.  
445 W. MAIN ST., WYCKOFF, NEW JERSEY, 07481, U.S.A.

CERTIFICATE No.

0000723

**CUSTOMER:** NEW JERSEY INSTITUTE OF TECHNOLOGY

**STREET:** UNIVERSITY HEIGHTS

**CITY:** NEWARK

**STATE:** N.J. **ZIP:** 07102

**DATE OF CALIBRATION:** 21 AUG, 95

**NEXT CALIBRATION DATE:** 21 AUG, 96

**MODEL NO:** M360

**DESCRIPTION:** BLACKBODY SOURCE

**SERIAL NUMBER:** 39491-2

**CUSTOMER P/O NUMBER:** N/A

### DATA

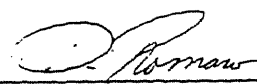
STANDARD READING	MIKRON READING	MIKRON CORRECTION
680.0 °C	680.0 °C	±0.0 °C
801.0 °C	800.0 °C	+1.0 °C
963.0 °C	961.0 °C	+2.0 °C

**AMBIENT TEMP.:** 24 °C  
**HUMIDITY:** 50 %

ALL ABOVE DATA ARE TRACEABLE TO NIST  
(NIST REFERENCE NUMBER)

EQUIPMENT USED	MODEL	PARAMETER	SERIAL NO.	REFERENCE NO.
MIKRON	M90VHG	TEMPERATURE	43672	844/251488-93
MIKRON	M90HSTD	TEMPERATURE	36409	TRANSFER STANDARD
MIKRON	M90QSTD	TEMPERATURE	40588	TRANSFER STANDARD

**CALIBRATED BY:**

  
D. ROMANO

**CERTIFIED BY:**

  
K. IRANI

**Figure 6.9** Certificate of calibration of Mikron M360 blackbody reference source

The magnitude of the saturation non-linearity was also confirmed experimentally by the following procedure [35]. To eliminate the dark current charge from the detected signal, the dark current generation was suppressed by reducing the operating temperature of the imager to approximately 68K using vacuum pumping on the N<sub>2</sub> dewar.

**Table 6.2** Calibration of M-WIP filters

Filter  No	$\Delta\lambda$  (nm)	Calibrated Center Wavelength of M-WIP Channels, $\lambda_0$ (nm)			
		I OFC Spec's	II Prior to Non-Linearity Correction	III Estimated Effect of Non-Linearity	IV After Non-Linearity Correction
1	51	1790	2004	2007	1758
2	64	2180	2220	2258	2174
3	60	2580	2721	2792	2446
4	38	3158	3186	3227	2961
5	60	3447	3696	3645	3113
6	77	3970	4175	4267	3756
7	102	4536	4870	4846	4594

Measurements of room temperature background were then performed for various integration times. The results of these measurements were fitted with a second-order polynomial having a small quadratic component as shown in Figure 6.10. The estimated

non-linear response shows a 6% error as compared with a linear prediction at  $0.5 Q_{\max}$ . This effect was shown to be independent of time and solely dependent on signal level. Therefore, in the absence of the dark current, a simple correction can compensate for this non-linear effect. Also shown in Figure 6.10 is a non-linear response at small signal levels. This non-linearity is attributed to charge trapping effect that may also be associated with a narrow trench that is built into the BCCD output register. This effect becomes negligible at  $0.1 \times Q_{\max}$ .

Therefore, a linear fit from zero signal at zero integration time to a point on the curve away from the small-signal nonlinearity is needed to precisely determine the exact background signal for small background levels. This linear fit is shown in the inset of Figure 6.10.

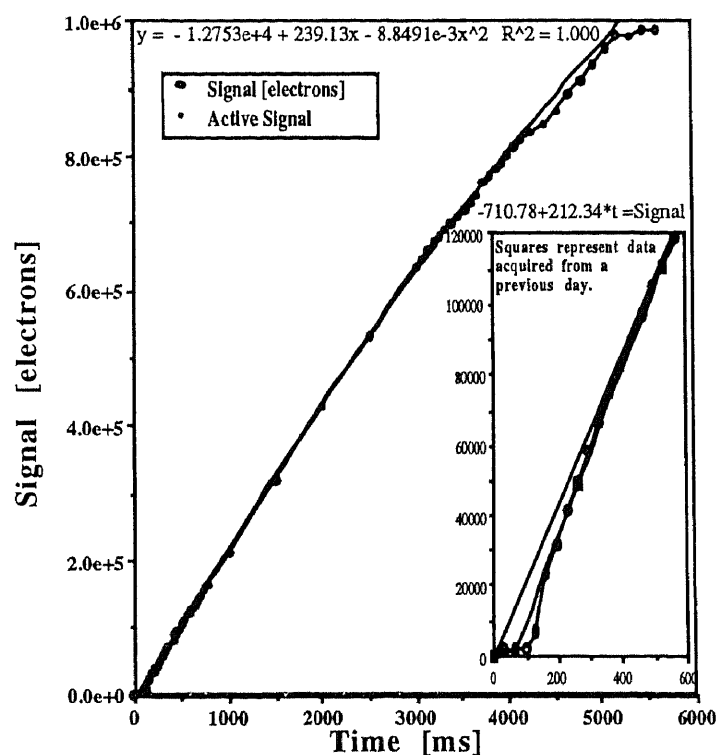


**Figure 6.10** The background signal of the 320X122 IR-CCD camera vs. optical integration time

### 6.3.2 Compensation for Secondary Transmission Bands of M-WIP Filters

Careful inspection of the spectral scans of the filters provided by the manufacturer (Optical Filter Corporation, Natick, MA) revealed that some of the M-WIP filters have secondary transmission bands with peak transmission of the order of 1% to 3% of the corresponding peaks of primary transmission bands. Therefore, the thermal radiation flux transmitted through the filters corresponds to a sum of radiation fluxes corresponding to primary and secondary transmission bands. Furthermore, the ratio of the radiation transmitted through the secondary transmission bands to that transmitted through the primary band depends not only on the ratio of the respective transmission peaks, but also on the spectral properties of the incident radiation and, therefore, the temperature of the radiant target. Consequently, the results of the calibration procedure given by Equation (6.15) are somewhat dependent on the range of blackbody temperatures utilized for calibration.

In order to better account for the effect of the secondary transmission bands on the calibration results, the original calibration procedure given by Equation (6.15) has been modified as follows:

$$\min_{\tau_o(T_j), \lambda_o(T_j)} \sum_{i=1}^M \left\{ \frac{1}{(\sigma_i(T_j))^2} \left[ S_i - \tilde{S}(T_i^{BB}, \tau_o(T_j), \lambda_o(T_j)) \right]^2 \right\} \rightarrow \tau_o(T_j), \lambda_o(T_j) \quad (6.16)$$

where:

$T_i^{BB}$  –  $i$ -th temperature of the reference blackbody source (K),

$\sigma_i(T_j) = \sigma_i^0 \cdot W^{|T_i - T_j|}$ ,  $i = 1, \dots, M$ ;  $j = 1, \dots, M$

$\sigma_i^0 = \Delta S_i = \sqrt{S_i}$  – rms signal noise (rms electrons/pixel).

The calibration results obtained by the described above temperature-dependent calibration algorithm are illustrated for 7 M-WIP filters in Figure 6.11. Figure 6.12 illustrates the deviations of the calibration results from the manufacturers specifications for individual filters.

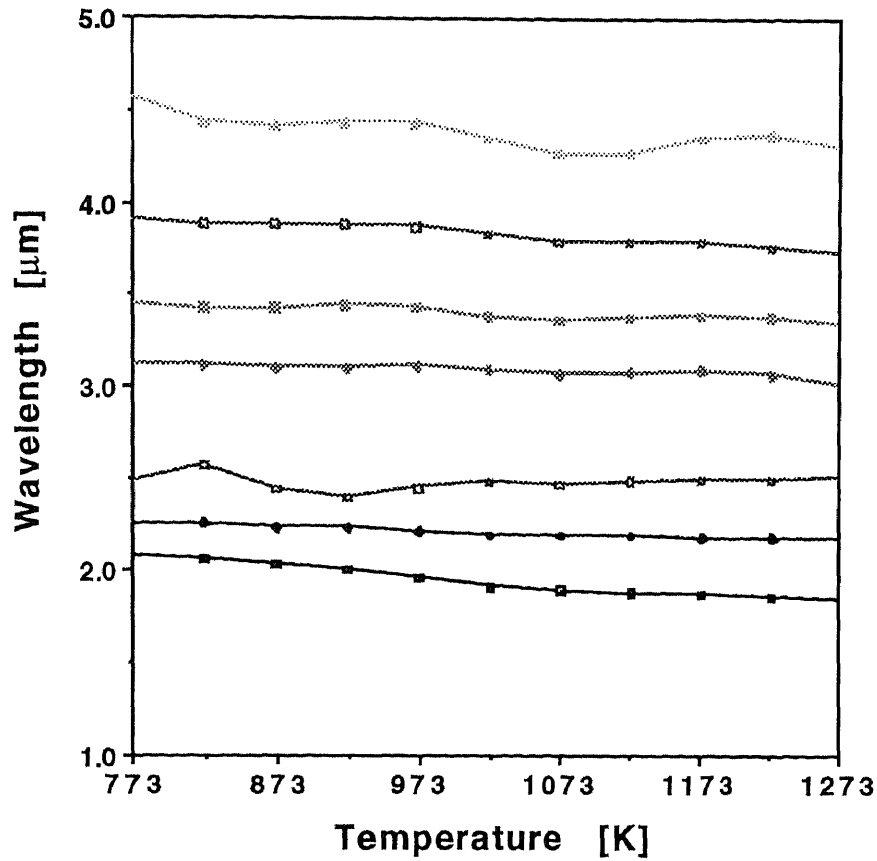


**Figure 6.11** Temperature-dependent calibration of M-WIP filters

In order to take advantage of the temperature-dependent results of the new calibration procedure the least-squares based M-WIP temperature measurement algorithm given by Equation (3.1) has been modified into following iterative procedure:

1. Initial estimate of the target temperature  $T^0$  is assumed based on the available information about the radiative target (during continuous real-time temperature monitoring  $T^0$  can be set equal to the last available measurement result);
2. Table of calibration values  $\lambda_0(T_j)$ ,  $\tau_0(T_j)$ ,  $j=1, \dots, M$  is searched to determine the value  $k$  such that

$$T_{k-1} < T^0 < T_k$$

The required values  $\lambda_0(T^0)$ ,  $\tau_0(T^0)$  are then obtained by linear interpolation based on  $\lambda_0(T_{k-1})$ ,  $\tau_0(T_{k-1})$  and  $\lambda_0(T_k)$ ,  $\tau_0(T_k)$ ;

3. The first approximation of the target temperature,  $T^1$ , is computed from Equation (3.1) using  $\lambda_0(T_j)$  and  $\tau_0(T_j)$  as the calibration parameters;
4. Using  $T^1$  as the new initial estimate of the target temperature (i.e., setting  $T^0=T^1$ ), the steps 2 and 3 are repeated.

It should be noted that in the case of real-time continuous M-WIP monitoring of targets with slowly varying temperature, a single pass through the above M-WIP measurement algorithm may yield an acceptable result. Therefore, new temperature-dependent calibration procedure will not necessarily lead to increase of computational burden.

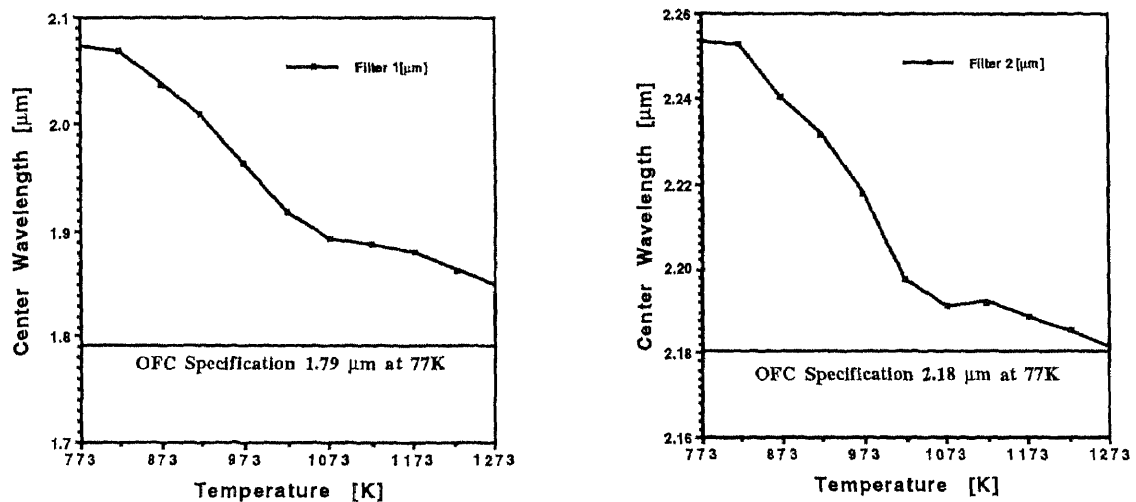


**Figure 6.12** Temperature-dependent calibration of M-WIP filters vs. manufacturers data

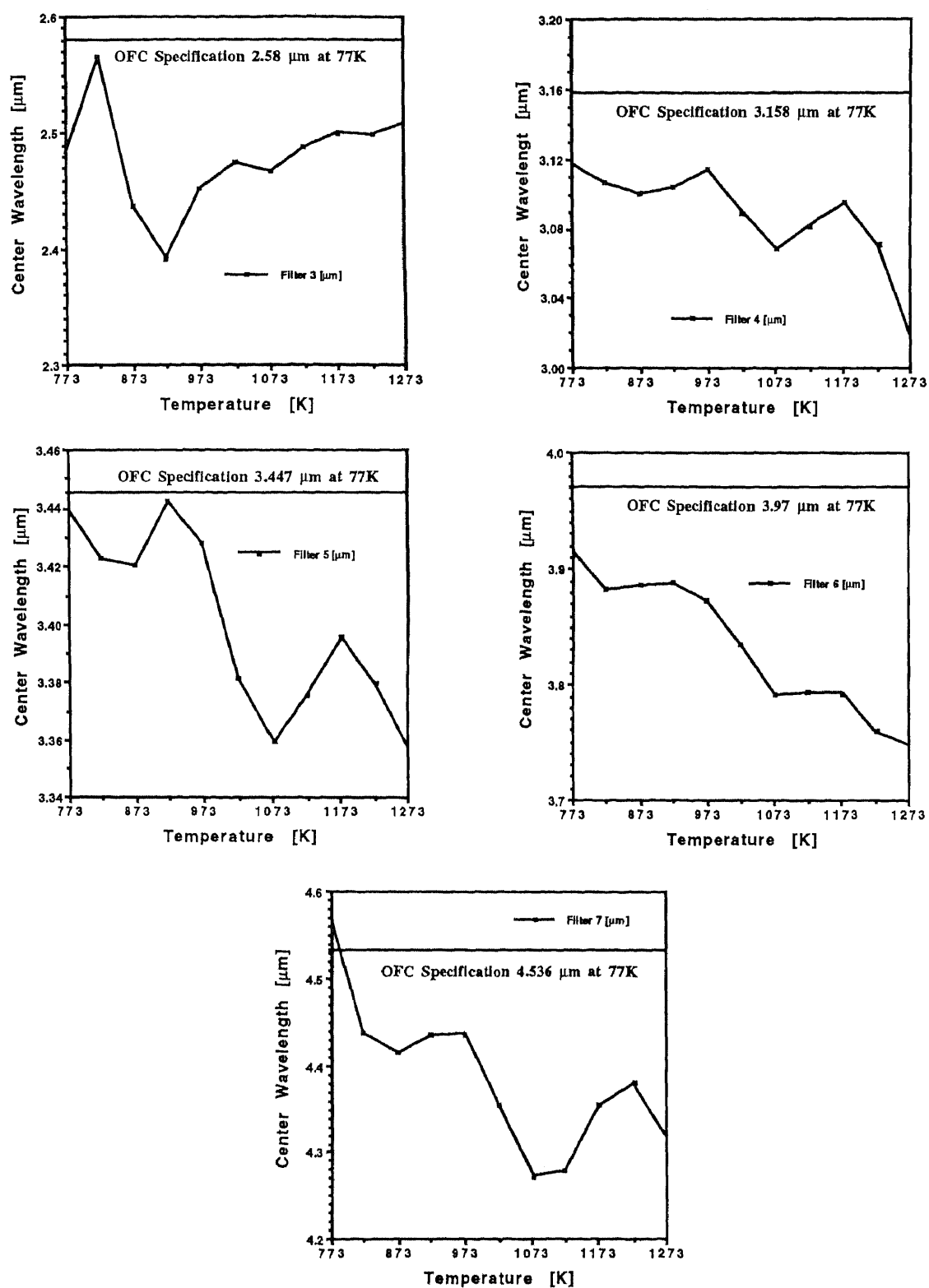
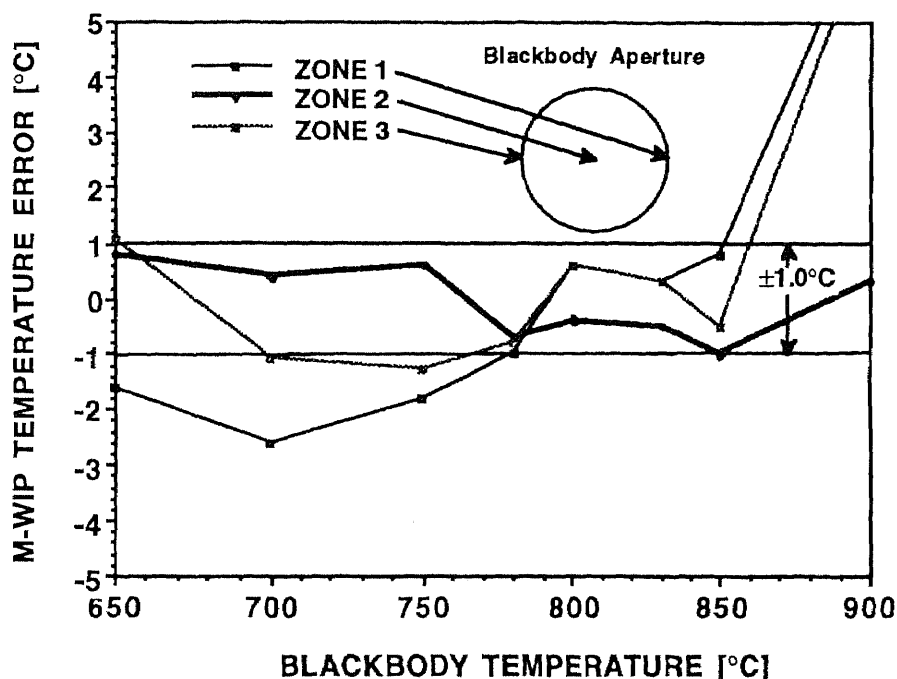


Figure 6.12 (cont.) Temperature-dependent calibration of M-WIP filters vs. manufacturer data

#### 6.4 Demonstrated Temperature Resolution of M-WIP based on PtSi IR FPA

Using the M-WIP calibration with the correction for “saturation” non-linearity, given by Equation (6.6), we have achieved an accuracy of  $\pm 1.0^{\circ}\text{C}$  for on-line real-time M-WIP temperature measurements of the center of the blackbody aperture in the range from  $650^{\circ}\text{C}$  to  $900^{\circ}\text{C}$ , as illustrated in Figure 6.13.



**Figure 6.13** Real-time M-WIP measurements of blackbody temperature after implementation of on-line correction for “saturation” nonlinearity

Upon upgrading the M-WIP software to include non-linearity independent algorithm described in Section 4.3 we were able to expand the temperature range of M-WIP measurements. Using fixed operational signal levels we demonstrated an accuracy of  $\pm 1.0^{\circ}\text{C}$  for real-time temperature measurements of the blackbody target in the range from  $500^{\circ}\text{C}$  to  $1000^{\circ}\text{C}$ , as illustrated in Figure 6.14.

In order to study the accuracy of M-WIP temperature measurements for targets with spectrally varying emissivity, a double side polished silicon wafer was placed in the optical



path of M-WIP system. The blackbody source was then imaged onto M-WIP filter assembly through the silicon wafer acting as a broadband filter with spectrally varying transmission. In this set-up, the spectral characteristics of the radiation incident on the M-WIP imager are given by the product of the blackbody radiation (given by the Planck's equation) and the spectral transmission of the double-polished silicon wafer. Therefore, for this test the radiation incident on the M-WIP imager corresponds to that of radiant target with temperature equal to the temperature of the blackbody source and the spectral emissivity equal to the transmittance of the double side polished silicon wafer.

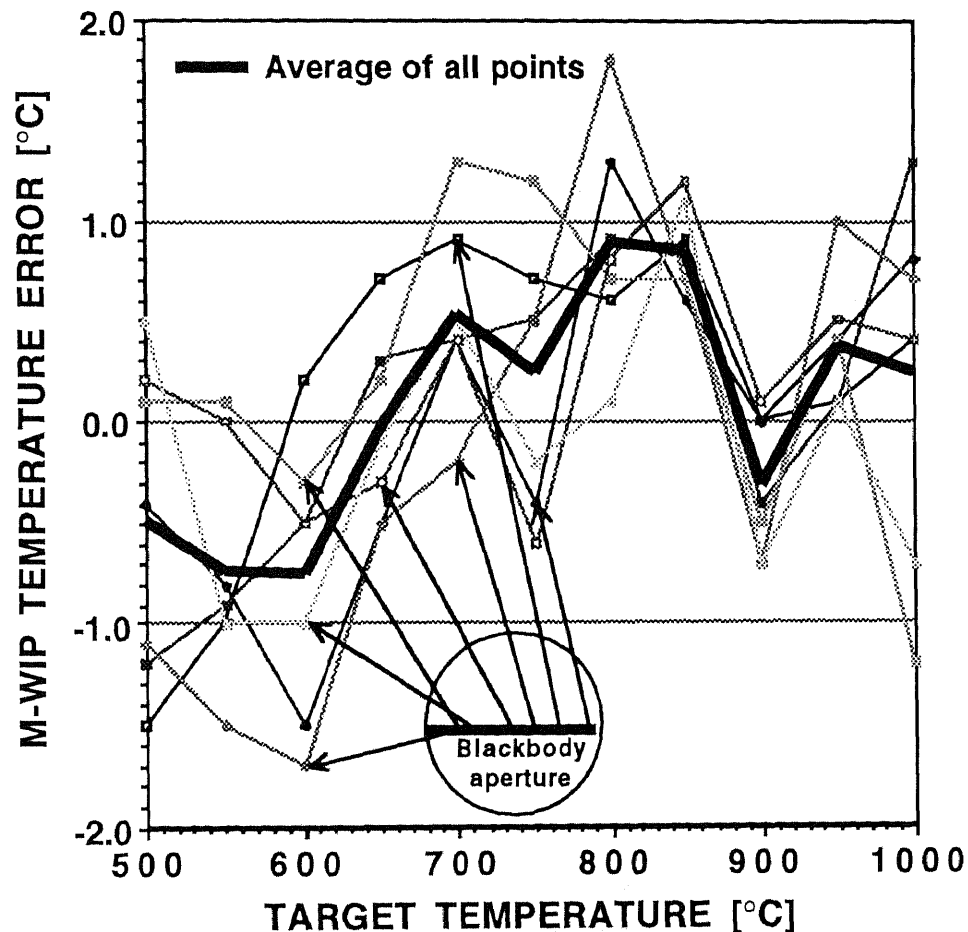


**Figure 6.14** Real-time M-WIP measurements of blackbody temperature after implementation of non-linearity independent M-WIP algorithm

Initially, to obtain accurate temperature estimation for the case of double side polished silicon wafer placed in the optical path of the M-WIP system we had to resort to off-line measurements based on the pre-recorded data. The detected radiometric signals were recorded for a wide range of optical integration times and target temperatures, to allow for accurate compensation for non-linearity of imager response according to the algorithm described in Section 4.2. Using this approach we have demonstrated the accuracy of  $\pm 4^\circ\text{C}$  for off-line temperature measurements of the location corresponding to the center of silicon wafer in the temperature range from  $500^\circ\text{C}$  to  $950^\circ\text{C}$ , as illustrated in Figure 6.15. The corresponding M-WIP estimate of the spectral transmissivity of the double side polished silicon wafer is:

$$\tau(\lambda) = 0.4893 + 0.017 \cdot \lambda \quad (6.17)$$

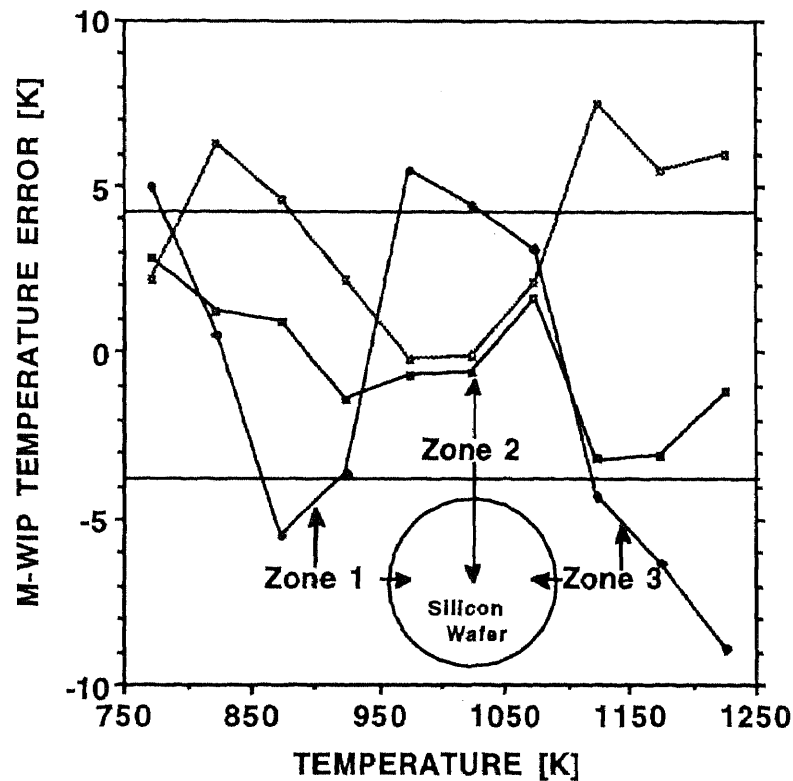


**Figure 6.15** M-WIP measurements of target temperature with effective emissivity equal to the transmissivity of double-polished silicon wafer

Poor accuracy of real-time M-WIP temperature measurements of blackbody target viewed through the silicon wafer led to the development of non-linearity independent M-WIP algorithm described in Section 4.3. Based on this algorithm we have demonstrated the accuracy of  $\pm 3^{\circ}\text{C}$  for real-time M-WIP temperature measurements of the blackbody target viewed through the double side polished silicon wafer in the temperature range from  $500^{\circ}\text{C}$  to  $900^{\circ}\text{C}$ , as shown in Figure 6.16.

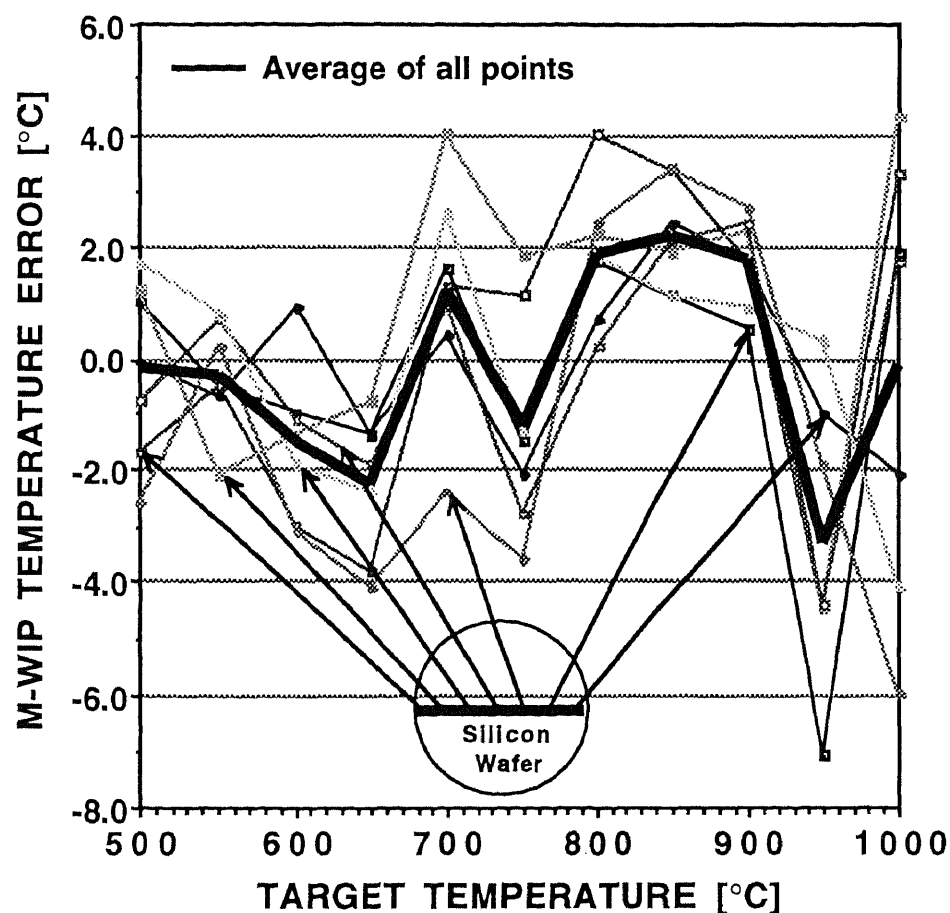


**Figure 6.16** Real-time M-WIP temperature measurements of blackbody target viewed through double-polished silicon wafer. Based on non-linearity independent algorithm

The quality of the least-squares fit of the theoretical M-WIP signal model to the experimentally detected signal corresponding to blackbody target at various temperatures is

illustrated in Figure 6.17. It should be noted that the presented results were normalized to the transmission characteristics of the filter No. 1.

As described in Chapter 3, in order to arrive at the estimates of the target temperature and emissivity M-WIP software employs combination of Levenberg-Marquardt and simulated annealing methods to find the minimum of the  $\chi^2$  surface given by Equation (3.1). As illustrated in Figure 6.18 and Figure 6.19 the algorithm reaches the close proximity of the  $\chi^2$  surface minima (corresponding to M-WIP estimates of target temperature and emissivity) after only a few iterations using as initial “guess” the value exceeding the true target temperature by 100°C.

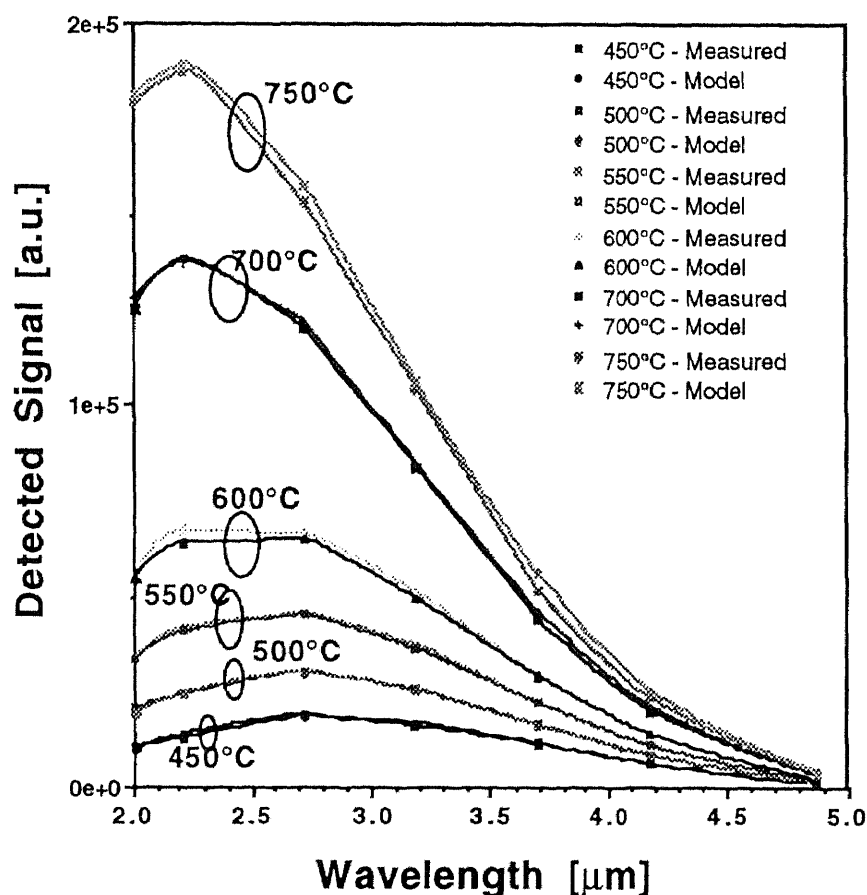


**Figure 6.17** Measured and M-WIP modeled signal levels for blackbody target in the temperature range from 450°C to 750°C

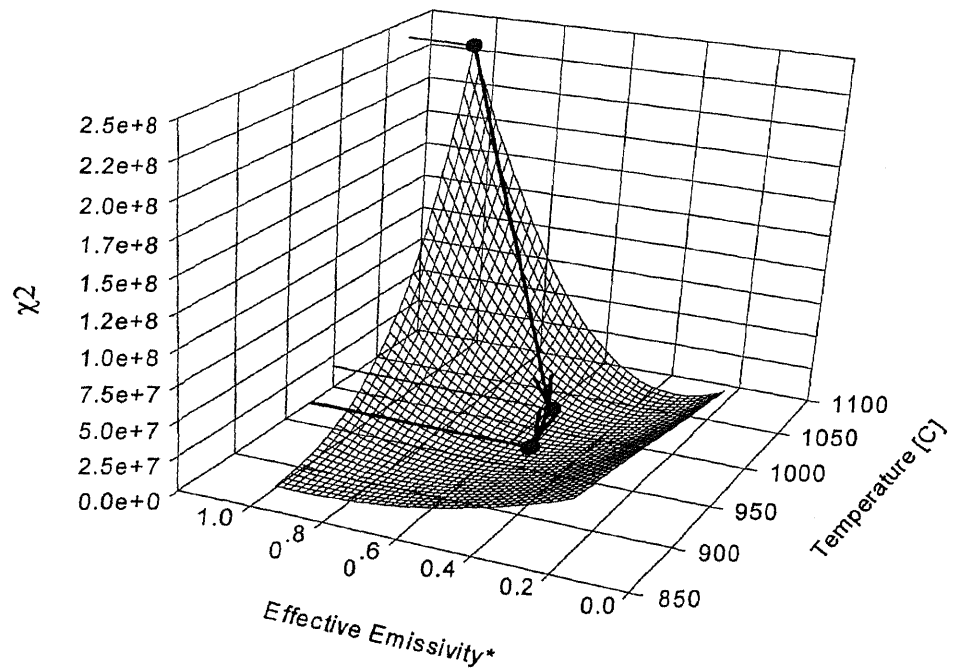


**Figure 6.18** First two steps of  $\chi^2$  - minimization by M-WIP algorithm for target at 973.3°C with effective emissivity equal to the transmissivity of the double side polished silicon wafer

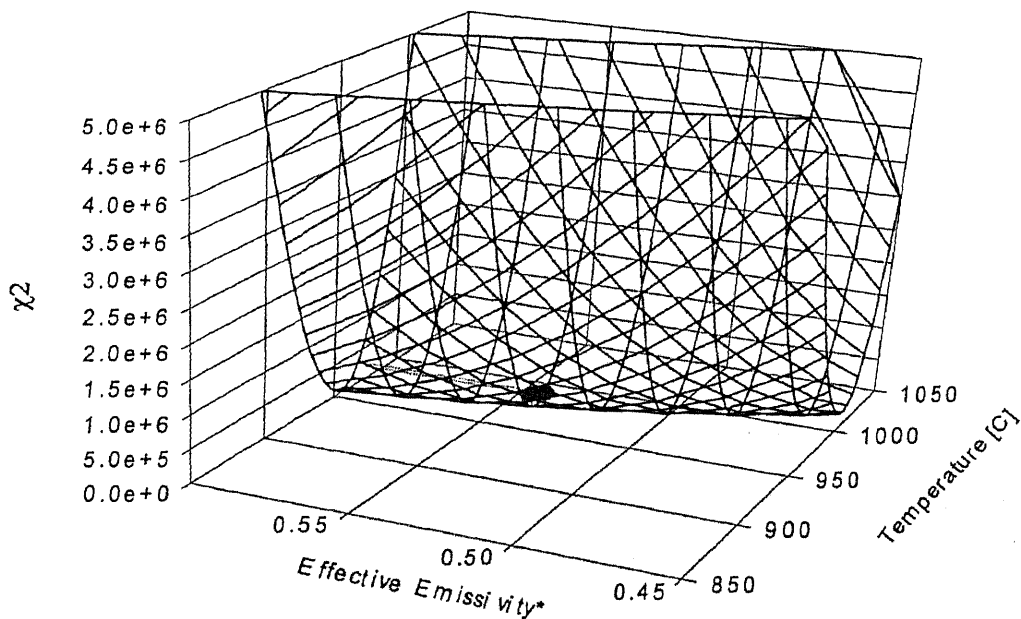


**Figure 6.19**  $\chi^2$  - minimization by M-WIP algorithm in the proximity of the solution for the same target as in Figure 6.18

## CHAPTER 7

### CONCLUSIONS

The research effort described in this dissertation demonstrated that least-squares based multi-wavelength pyrometric systems are capable of highly accurate non-contact temperature estimation for targets with unknown wavelength dependent surface emissivity. Presented in this dissertation are the development of an experimental Multi-Wavelength Imaging Pyrometer (M-WIP) and associated algorithms for real-time M-WIP temperature sensing, system calibration and non-linearity independent operation that advanced state-of-the-art and extended the practicality of multi-wavelength pyrometry.

The objectives of this research, outlined in Introduction, were met as follows:

- The radiometric model of multi-wavelength pyrometric systems for emissivity-independent non-contact temperature sensing was developed. Based on this model the algorithm for theoretical performance prediction of Multi-Wavelength Imaging Pyrometers (M-WIPs) has been introduced. Using this model the performance of a number of M-WIPs was investigated, including M-WIP systems based on IR FPAs with PtSi Schottky-barrier detectors, InGaAs line arrays, and microbolometer Uncooled Focal Plane Arrays (UFPAs). These performance predictions were based on the detailed analysis of noise sources affecting the signal output of the above sensors.
- A prototype Multi-Wavelength Imaging Pyrometer (M-WIP) was developed for remote sensing of temperature profiles of gray and color targets with unknown emissivities. An experimental 7-filter line-sensing M-WIP is developed based on a 320x122-element non-interlaced PtSi IR-CCD radiometric camera capable of operation with optical integration times ranging from 0.12ms to 12 s, thus providing wide dynamic range. The camera is equipped with an assembly of 7 striped interference filters in the spectral range from 1790 nm through 4536 nm. Video image processing for prototype M-WIP systems based on the DATACUBE MaxVideo system hosted by a SUN workstation.

- A number of M-WIP designs suitable for area, line, and point temperature sensing have been proposed.
- Real time M-WIP algorithm has been developed and implemented, providing for fast multi-point estimation of target temperature and emissivity. The algorithm employs the combination of Levenberg-Marquardt and simulated annealing minimization methods allowing for determination of the global minima of M-WIP least-squares minimization problem.
- Extensive experimental work was performed to study the inherent non-linearities in the response of PtSi IR-CCD imagers and InGaAs line sensor arrays. These experiments demonstrated that both dark current and spectral response of the above IR sensors depend on the bias voltage across photodetectors. The above sensors are usually operated in reverse bias mode, with detector bias voltage being allowed to float towards zero during the optical integration time. As a result, the dark current leakage is decreasing with increase of accumulated signal level. Furthermore, due to change in depletion layer thickness its capacitance depends on the detector bias voltage, leading to decrease in detector responsivity with increase of accumulated signal.
- The algorithm allowing to estimate the dark current charge as function of accumulated signal level and duration of optical integration time was developed and incorporated into real-time M-WIP software. This algorithm relies on off-line characterization of the time derivative of the dark current charge as function of the accumulated signal. During real-time M-WIP temperature measurements this dark current time derivative is integrated over current duration of optical integration time, taking into account the intensity of the incident radiative flux.
- In order to circumvent the problem of responsivity variation with magnitude of the detected signal, the algorithm providing for fixed level operation of the M-WIP sensor was developed and implemented. This algorithm exploits the ability of the imager to

change in-line the duration of optical integration time. Utilizing this capability, the algorithm determines the values of optical integration time yielding fixed pre-selected signal levels for all M-WIP spectral channels, regardless of target temperature. The resulting values of optical integration time, rather than detected signals themselves, are then used for M-WIP temperature estimation, providing for virtually non-linearity independent system operation.

- The experimental M-WIP system also includes least-squares based calibration software, allowing to determine effective spectral characteristics of all M-WIP channels based on a wide range of blackbody temperature measurements. In the case of poor out-of-band filter blocking, the calibration algorithm also compensates for the secondary transmission peaks of M-WIP filters.
- After calibration against a commercial NIST-traceable blackbody reference source, the temperature resolution of  $\pm 1^{\circ}\text{C}$  was demonstrated with the experimental M-WIP system for real-time temperature measurement of the blackbody source in the temperature range from  $500^{\circ}\text{C}$  to  $1000^{\circ}\text{C}$ .
- The study of the accuracy of M-WIP temperature measurements for targets with spectrally varying emissivity was conducted using double-polished silicon wafer placed in the optical path of M-WIP system. Temperature resolution of  $\pm 3^{\circ}\text{C}$  was demonstrated with the experimental M-WIP system for blackbody source viewed through the double polished silicon wafer with unknown spectral transmissivity in the temperature range from  $500^{\circ}\text{C}$  to  $900^{\circ}\text{C}$ .



## REFERENCES

- [1] A. Gat and M. French, "Bichannel Radiation Detection Apparatus," United States Patent 5,165,796 (1992).
- [2] M. Hirano, "Temperature Measuring Device," United States Patent 4,980,847 (1990).
- [3] J. Kyriakis, "Non-Contact Temperature Measurement of a Static or Moving Target," *United States Patent 4,693,615* (1987).
- [4] F. Tanaka and D. P. DeWitt, "Radiation Thermometry," *United States Patent 4,881,823* (1989).
- [5] N. Domarenok et al., "Thermovision Pyrometer for Remote Measurement of Temperature of an Object," *United States Patent 4,403,251* (1983).
- [6] W. H. Glenn, "Active Optical Pyrometer," United States Patent 4,818,102 (1989).
- [7] M. Tatsuwaki, S. Nemoto, S. Okuhara, "Temperature Pattern Measuring Method and Defice Therefor," *United States Patent 4,413,324* (1983).
- [8] M. A. Khan, C. Allemand, and T. W. Eagar, "Emissivity Independent Multiwavelength Pyrometer," *United States Patent 5,132,922* (1992).
- [9] D. L. Ng, "Multiwavelength Pyrometer for Gray and Non-Gray Surfaces in the Presence of Interfering Radiation," *United States Patent 5,326,172* (1994).
- [10] D. P DeWitt and F. P. Incropera, "Physics of Thermal Radiation," in *Theory and Practice of Radiation Thermometry*, John Wiley & Sons, New York (1988).
- [11] Nutter, G. D, "Radiation Thermometers," in *Theory and Practice of Radiation Thermometry*, John Wiley & Sons, New York (1988).
- [12] M.B. Kaplinsky, "Application of Imaging Pyrometry for Remote Temperature Measurement," *Masters Thesis*, Department of Electrical and Computer Engineering, New Jersey Institute of Technology, Newark, NJ (1993).
- [13] W. F. Kosonocky, M. B Kaplinsky, N. J. McCaffrey, E. S. Hou, C. N. Manikopoulos, N. M. Ravindra, S. Belikov, J. Li and V. Patel, "Multi-Wavelength Imaging Pyrometer," *SPIE Proceedings*, Vol. 2225-04, Orlando, FL (1994).
- [14] P. R. Bevington, *Data Reduction and Error Analysis for the Physical Sciences*, McGraw-Hill Book Co., New York (1969).
- [15] R. A. Smith, F. E. Jones, and R. P. Chasmar, *The Detection and Measurement of Infrared Radiation*, Oxford University Press, London (1968).
- [16] N. J. McCaffrey, M. B. Kaplinsky, B. Esposito, and W. F. Kosonocky, "Radiometric Performance of 640x480 and 320x244 PtSi IR Cameras," *SPIE Proceedings*, Vol. 2225-05, Orlando, FL (1994).

- [17] M.A Khan, et. al., "Noncontact Temperature Measurement: Least Squares Based Techniques," *Rev. Sci. Instrum.* 62, 403 (1991).
- [18] P. B. Coates, "Multi-Wavelength Pyrometry," *Metrologia* 17, 103 (1981).
- [19] M. A. Khan, et. al. "Noncontact Temperature Measurement: Interpolation Based Techniques," *Rev. Sci. Instrum.* 62, 393 (1991).
- [20] A. S. Tenney, "Radiation Ratio Thermometry," in *Theory and Practice of Radiation Thermometry*, John Wiley & Sons, New York (1988).
- [21] W.H. Press, S.A. Teukolsky, W.T. Vetterling, and B.P. Flannery, *Numerical Recipes in C: the art of scientific computing*, Cambridge University Press, New York, NY (1992).
- [22] D.P. DeWitt and J.C. Richmond, "Thermal Radiative Properties of Materials," in *Theory and Practice of Radiation Thermometry*, John Wiley & Sons, New York, NY (1988).
- [23] T. Sato, "Spectral Emissivity of Silicon," *Japanese J. of Appl. Phys.* 6, 339 (1967).
- [24] N.M. Ravindra, et. al., "Development of Emissivity Models and Induced Transmission Filters for Multi-Wavelength Imaging Pyrometry," *SPIE Proceedings*, Vol. 2245-48, Orlando, FL (1994).
- [25] N. Ansari and E. Hou, *Computational Intelligence for Optimization*, Kluwer Academic Publishers, Boston, MA (1997).
- [26] M. B. Kaplinsky, N. J. McCaffrey, and W. F. Kosonocky. "Multi-Wavelength Imaging Pyrometer," *Patent disclosure submitted to U.S. Office of Patents and Trademarks* (1995).
- [27] P.B. Coates, "Wavelength Specification in Optical and Photoelectric Pyrometry," *Metrologia*, 13, 1 (1977)
- [28] W. F. Kosonocky, *Review of Infrared Image Sensors with Schottky-Barrier*, Mita Press, Tokyo (1991).
- [29] W.F. Kosonocky, "State-of-the-Art in Schottky-Barrier IR Image Sensors," *SPIE Proceedings*, Vol. 1685-2, Orlando, FL (1992).
- [30] R. A. Wood, "Uncooled Thermal Imaging with Monolithic Silicon Focal Planes," *SPIE Proceedings*, Vol. 2020, San Diego, CA (1993).
- [31] S. B. Horn, R. G. Buser. "Uncooled Sensor Technology," *SPIE Proceedings*, Vol. 2020, San Diego, CA (1993).
- [32] E. L. Dereniak and G. D. Boreman, *Infrared Detectors and Systems*, John Willey and Sons, New York (1996).

- [33] M. B. Kaplinsky, J. Li, N. J. McCaffrey, E. S. Hou, and W. F. Kosonocky, "Progress on the Development of Multi-Wavelength Imaging Pyrometer", *SPIE Proceedings*, Vol. 2746-18, Orlando, FL (1996).
- [34] W. F. Kosonocky, et al. "Multi-Wavelength Imaging Pyrometer (M-WIP) for Semiconductor Process Monitoring and Control," *WL-TR-95-8010 Final Technical Report*, Air Force Material Command, Wright Patterson AFB (1995).
- [35] N.J. McCaffrey, "Design of a 320X122 MWIR-CCD PtSi Imaging Radiometer with Automatic Optical Integration Time Control", *Masters Thesis*, Department of Electrical and Computer Engineering, New Jersey Institute of Technology, Newark, NJ (1993).
- [36] J. Li, E. Hou, M. B. Kaplinsky, J. Li, N. J. McCaffrey, and W. F. Kosonocky, "M-WIP Workstation for RTP Monitoring and Control," *Proceedings of 1996 TMS Annual Meeting*, Anaheim, CA (1996).
- [37] M. B. Kaplinsky, W. F. Kosonocky, and N. J. McCaffrey, "Calibration of Multi-Wavelength Imaging Pyrometer," *Proceedings of 5th Infrared Radiometric Sensor Calibration Symposium*, Logan, Utah (May 1995).
- [38] M. B. Kaplinsky, W. F. Kosonocky, N. J. McCaffrey, J. Li, E. S. Hou, C. N. Manikopoulos, and N. M. Ravindra, "Multi-Wavelength Imaging Pyrometer for Non-Contact Temperature Sensing," *Proceedings of IEEE International Symposium on Industrial Electronics*, Athens, Greece (July 1995).
- [39] M. B. Kaplinsky, et al. "Recent Advances in the Development of Multi-Wavelength Imaging Pyrometer," *submitted for publication in Optical Engineering* (1997).